Push-Pull Tests to Support *In Situ* Chemical Oxidation System Design

by

Ashley Mathai

A thesis
presented to the University of Waterloo
in fulfillment of the
thesis requirement for the degree of
Master of Applied Science
in
Civil Engineering

Waterloo, Ontario, Canada, 2011

Author's Declaration

I hereby declare that I am the sole author of this thesis. This is a true copy of the thesis, including any required final revisions, as accepted by my examiners.

I understand that my thesis may be made electronically available to the public.

Abstract

The problems associated with the contamination of groundwater environments by non-aqueous phase liquids (NAPLs) such as chlorinated solvents, gasoline and manufacturing gas plant (MGP) residuals, including their distribution and persistence, are well accepted. The treatment of groundwater by *in situ* chemical oxidation (ISCO) relies on the oxidation potential of chemical reagents to destroy harmful organic compounds. The interaction of these oxidants with target and non-target compounds in the subsurface will help determine effectiveness and efficiency of an ISCO treatment system. Push-pull tests (PPTs) have the utility to estimate key properties *in situ* and allow for sampling a larger volume of aquifer to yield more representative estimates as compared to conventional bench-scale tests. The scale and cost-effectiveness of a PPT make it an ideal tool to collect valuable information on subsurface system behaviour so that uncertainties can be minimized. The use of PPTs to provide insight into treatment expectations or to support the design of an ISCO system requires a suitable interpretation tool.

A multi-species numerical model ('PPT-ISCO') in a radial coordinate system was developed to simulate a PPT with the injection of a conservative tracer and oxidant (persulfate or permanganate) into the saturated zone of a porous medium environment. The pore space may contain variable amounts of immobile, multicomponent, residual NAPL. The aquifer material contains a natural organic matter (NOM) fraction and/or other oxidizable aquifer material (OAM) species. The model is capable of simulating mass transport for an arbitrary number of conservative and reactive tracers and NAPL constituents subjected to chemical reactions.

The ability of PPTs to capture the *in situ* natural oxidant interaction (NOI) was tested with PPT-ISCO. Breakthrough curve (BTC) data collected from permanganate and persulfate PPTs conducted in the field were compared to simulated BTCs by assigning the same field operational parameters to the model and applying NOI kinetic information obtained from batch tests. These tests confirmed the usability of the model and PPTs to obtain the NOI kinetics from PPT BTCs.

The sensitivity of PPT BTCs to variations in the field operating and NOI parameters were investigated. The results of varying the field operating parameters indicated that the oxidant BTCs could be scaled to match varying injection and extraction flow rates. Variations in NOI parameters revealed that the permanganate BTC is primarily controlled by the permanganate fast reaction rate coefficient and the quantity of OAM present in the aquifer. The spatial profiles of

OAM across the test zone revealed that the majority of the OAM consumption is from the fast fraction and occurs in the vicinity of the well where the permanganate concentration is greatest. An estimate of the permanganate fast reaction rate coefficient can be obtained from a permanganate PPT BTC by employing the model to simulate the PPT with the operational parameters (used in the field) and literature estimates of the remaining NOI parameters. Calibration between the simulated and observed BTCs can be undertaken to adjust the permanganate fast reaction rate coefficient to fit the permanganate PPT BTC.

Persulfate NOI sensitivity investigations revealed that persulfate PPT BTCs can be characterized by a concentration plateau at early times as a result of the increased ionic strength in the area around the injection well. The ionic strength is primarily controlled by the injected persulfate concentration, and as persulfate degrades into sulphate and acid, the ionic strength is enhanced. Graphical analysis of the BTC revealed that an underestimated value of the persulfate degradation rate coefficient can be obtained from the PPT BTC. A more representative estimate of the persulfate degradation rate coefficient can be achieved after fitting the field BTC to the simulated results, applying the underestimated value as a starting point.

PPTs investigating ISCO treatability have the ability to provide insight into the effect of the NOI on the oxidation of target compounds, site-specific oxidant dosage requirements and NAPL treatment expectations. NAPL component BTCs from treatability PPTs are primarily controlled by the mass in the fast region, and the fast region mass transfer rate coefficient. Oxidation estimates extracted from NAPL component BTCs were shown to accurately approximate the mass of each NAPL component oxidized when compared to model calculations. The mass of NAPL oxidized for each of the components yields a site-specific oxidant dosage. This estimate exceeds what is prescribed by the stoichiometry between permanganate and the contaminant of concern due to the effect of the NOI.

The utility of PPTs to study and quantify the interaction between injected oxidants and the aquifer material has been demonstrated with PPT-ISCO. In addition, PPT-ISCO has revealed that treatability PPTs can be tailored to investigate the dosage requirements and treatment expectations of residual NAPLs. Results from this effort will be used to support ongoing field research exploring the use of PPTs to assist in understanding the competing subsurface processes affecting ISCO applications.

Acknowledgements

Many people have made this experience the rewarding and learning experience it has been. I would like to thank Dr. Neil Thomson for accepting me into his research program and for giving me this very interesting and challenging project to work on. Neil's mentorship and encouragement has provided the backdrop for my progress and development and for this I am forever appreciative.

I would also like to express my gratitude to Dr. Stefano Normani for his invaluable assistance in setting up the FORTRAN compiler on my laptop and for all his programming help throughout the course of the project.

Thank you to my parents who have supported me with their love, patience and food during my time at UW.

And to my friends, thank you for keeping me positive in the face of adversity and never-ending amounts of work and for making my time outside of school both rewarding and entertaining.

Financial support for this research was provided by a Natural Sciences and Engineering Research Council of Canada (NSERC) Canada Graduate Scholarship (PGS), a University of Waterloo President's Graduate Scholarship, and a NSERC Discovery Grant (N.R. Thomson).

Dedication

I would like to dedicate this thesis to my grandparents, Avira and Rosa Mathai, and Varkey and Mariam Anthony.

Table of Contents

List of Figures

List of Tables

1 Introduction

The problems associated with the contamination of groundwater environments by non-aqueous phase liquids (NAPLs) such as chlorinated solvents, gasoline and manufacturing gas plant (MGP) residuals, including their distribution and persistence, are well accepted (J. F. Pankow & Johnson, 1996). Conventional treatment technologies (e.g., pump-and-treat) are typically ineffective in removing residual NAPL because of the slow rate of dissolution and their low aqueous solubility. The *in situ* remediation of groundwater environments requires an understanding of the physical, chemical and biological properties governing the fate and transport of the contaminants of concern (COC) and potential treatment reagents. For example, to support a permanganate based *in situ* chemical oxidation (ISCO) application it is necessary to quantify hydraulic conductivity, porosity, reaction rates with the COC, natural oxidant demand (NOD) and perhaps the level of microbial activity (Sahl, Munakata-Marr, Crimi, & Siegrist, 2007; Seol, Zhang, & Schwartz, 2003; Xu & Thomson, 2009; Yan & Schwartz, 1999). Push-pull tests (PPTs) have the utility to estimate key properties *in situ* and allow for sampling a larger volume of aquifer to yield more representative estimates as compared to conventional bench-scale tests. The scale and cost-effectiveness of a PPT make it an ideal tool to collect valuable information on remedial system behaviour so that uncertainties can be minimized.

PPTs involve the injection ('push' phase) of a well-mixed solution consisting of a nonreactive, conservative tracer and one or more reactive tracers (biodegradable tracer, chemical oxidant, etc) into the saturated zone using a conventional monitoring well. The type, combination, and concentration of these tracers depend on the specific aquifer properties or processes to be investigated. After a sufficient time for kinetic processes to occur ('drift or reaction' phase), groundwater is extracted ('pull' phase) from the well. During the reaction phase no pumping occurs and the initial morphology of the injected solution mixture is controlled by the ambient groundwater flow field. Analysis of tracer breakthrough curves (BTCs) that are obtained by measuring tracer concentrations (and reaction by-products) in the extracted groundwater is performed to estimate the desired aquifer properties. The use of existing monitoring wells allows relatively inexpensive PPTs to be conducted at a variety of locations across the site. A practical limitation of the PPT is the lack of hydraulic control during the reaction phase and thus

in aquifers with large ambient groundwater velocities the duration of the reaction phase is limited.

The first PPT was conducted by Sternau et al. (1967) to study the degree of mixing of injected water with groundwater in an application related to artificial groundwater recharge (Istok, Humphrey, Schroth, Hyman, & O'Reilly, 1997). Since then PPTs have been used to determine a wide range of parameters from residual NAPL saturations, dispersivity, and effective porosity to aerobic respiration, denitrification, sulphate reduction, and methanogenesis reaction rates (Haggerty, Schroth, & Istok, 1998; Istok et al., 1997; M. H. Schroth, Istok, & Haggerty, 2000). Recently PPTs have been used to estimate the permanganate natural oxidant demand and observe persulfate temporal degradation (Mumford, Lamarche, & Thomson, 2004; Sra, Thomson, & Barker, 2010) . Istok (2008) extended the use of PPTs by considering them as feasibility assessment tools for surfactant enhanced NAPL recovery. In this case PPTs were used to quantify and identify the effects of sorption, precipitation and biodegradation on the ability of injected reagents to solubilise and mobilize residual phase trichloroethylene (TCE). Seok-Oh (2007) demonstrated the potential of PPTs to estimate TCE degradation rates.

Several analytical methods have been used to estimate *in situ* reaction rates from PPT BTCs. Snodgrass and Kitanidis (1998), and Haggerty et. al (1998) each developed simplified analytical methods to determine zero- and first-order reaction rate coefficients. In these simplified methods, rate coefficients are obtained by fitting a regression line to a plot of concentration versus time. The underlying assumptions in these methods include: (1) the injected tracers are simultaneously introduced as well-mixed slugs, (2) the dominating processes are advection and dispersion in a homogeneous, isotropic aquifer with spatially and temporally, uniformly distributed zero- or first-order irreversible reactions, (3) the tracer and reactants exhibit identical retardation (sorption is negligible), and (4) the background concentration of the conservative tracer and reactive tracers are negligible. Yang et al. (2007) elaborated on the method of Snodgrass and Kitanidis (1998) to include the case where the background concentrations are not negligible. Hageman (2003) presented an alternative analytical method (forced mass balance technique) that identifies first-order reaction rate coefficients for the case where sorption is not neglected. Recent work by Huang et al. (2010) has overcome previous limitations of dimensionality and linear equilibrium sorption by developing an analytical solution that accounts

for advection, longitudinal and transverse dispersion, first-order degradation, and rate-limited sorption. Despite these advancements, the rate coefficients estimated using simplified methods are limited to first- and zero- order mass action laws.

Numerical models (e.g., MODFLOW/MT3DMS, STOMP or STAMMT-R) offer advantages over simple analytical methods in that they are able to adapt to physical known heterogeneities and can simulate more complex reactions. Recently, Phanikumar (2010) developed a specific multi-species, radial coordinate numerical model to estimate kinetic rates of mixing interfaces (solution and native groundwater) based on PPT BTC data.

ISCO is a potentially effective technology that enhances the rate of NAPL mass removal by injecting a reagent into the subsurface that oxidizes aqueous phase contaminants into non-toxic end products (Thomson, Hood, & Farquhar, 2007). The use of PPTs to provide insight into treatment expectations or to support the design of an ISCO system requires a suitable interpretation tool. Unfortunately, analytical solutions and existing numerical models are unsuitable to handle the reaction expressions required.

Thomson (2011) summarized the behaviour of commonly used oxidants with uncontaminated aquifer solids and called this the natural oxidant interaction (NOI). Regardless of the choice of oxidant, the NOI will adversely impact ISCO applications by decreasing the mobility of the oxidant, reducing the reaction rate between the oxidant and target COC, and increasing the oxidant requirement to treat a contaminated aquifer system (Thomson, 2010). PPTs have been utilized to examine the interaction between oxidants and reductive species (reduced minerals and natural organic matter) (Mumford et al., 2004; Sra et al., 2010). PPTs used to investigate permanganate NOI have yielded favourable results when compared to bench-scale results (Mumford et al., 2004). PPTs conducted by Sra et. al (2010) were successful in producing persulfate BTCs that closely matched profiles provided by a persulfate kinetic model formulated from laboratory data. These results highlight the effectiveness of PPTs to capture *in situ* NOI behaviour.

To use PPTs to investigate ISCO treatability expectations of contaminated aquifers, the interpretation model must not only account for NOI but also for the reaction between the oxidant and the COC. If the NOI is parameterized with a separate set of PPTs, then the ability of the

oxidant to treat the COC can be explored. If NAPLs are present then dissolution kinetics and accessibility need to be considered. This is particularly important when multicomponent NAPLs like gasoline or MGP residuals are the contaminant source and the effective solubility changes as NAPL mass is depleted.

1.1 Thesis objectives

The objectives of this thesis are to:

1. Design and develop a multicomponent radially-symmetric numerical model to simulate a push-pull test to assess natural oxidant interaction and ISCO treatability;

2. Demonstrate the use of the developed model to investigate the interaction between an injected oxidant and natural organic matter/reduced minerals;

3. Examine the potential to optimize push-pull test operational parameters to obtain natural oxidant interaction kinetics from breakthrough curves; and

4. Explore opportunities to assess treatability of residual NAPL source zones using push-pull tests.

The results from this effort will be used to support ongoing field research exploring the use of push-pull tests to study the treatability of NAPL source zones using ISCO.

1.2 Thesis scope

To satisfy the thesis objectives stated above, a numerical model (PPT-ISCO) was developed to interpret PPT BTCs to yield information related to the NOI and NAPL treatability expectations. Chapter 2 outlines the model development and details the governing equations, numerical implementation and bench marking efforts. Chapter 3 examines the use of a PPT to investigate the NOI for permanganate and persulfate. Chapter 4 explores treatability PPTs and investigates the relationship between the BTCs and the controlling NAPL parameters. Finally, Chapter 5 presents the major findings and outlines recommendations for future research. The numerical code and sample input files are presented in Appendix A.

2 Development of PPT Model

A multi-species numerical model ('PPT-ISCO') in a radial coordinate system was developed to simulate a PPT with the injection of a conservative tracer and oxidant (persulfate or permanganate) into the saturated zone of a porous medium environment. The pore space may contain variable amounts of immobile, multicomponent, residual NAPL (Figure 2-1). The porous medium is assumed to be homogeneous with respect to grain size, mineral density and total porosity. The aquifer material contains a natural organic matter (NOM) fraction and/or other oxidizable aquifer material (OAM) species (Mumford et al., 2004). The model is capable of simulating mass transport of an arbitrary number of conservative and reactive tracers, and NAPL constituents subjected to chemical reactions.

2.1 Transport Processes

The transport of an aqueous species, *i*, can be represented by the radial advection dispersion equation (Bear, 1979), expressed as

$$\frac{\partial \theta C_i}{\partial t} = \frac{1}{r}\frac{\partial}{\partial r}\left[r(\alpha_r q + D^*_{d,i})\frac{\partial}{\partial r}(\theta C_i)\right] - \frac{1}{r}\frac{\partial}{\partial r}(rqC_i) + G_i^T \qquad (2\text{-}1)$$

where C_i (M/L^3) is the aqueous concentration of species *i*, either the tracer, oxidant, dissolved NAPL species, or a reaction by-product; r (L) is the radial distance from the well ($r_{\text{well}} \le r \le +\infty$); θ (L^3/L^3) is the total porosity of the medium; q (L/T) is the groundwater flux; α_r (L) is the longitudinal dispersivity; $D^*_{d,i}$ (L^2/T) is the effective molecular diffusion coefficient for species *i*; and G_i^T (M/L^3·T) is the total source/sink term for species *i,* which may represent mass transfer (G_i^{diss}), oxidation processes (G_i^{ox}), and the NOI (G_i^{NOI}).

The ambient groundwater velocity can be considered negligible relative to the gradient imposed by the injection system (Mumford, 2002). Assuming that the well screen fully penetrates the aquifer, and a steady-state well flow rate, the groundwater flux can be expressed as

$$q = \frac{\pm Q}{2\pi rb} \qquad (2\text{-}2)$$

where Q (L^3/T) is the well pumping rate (positive for injection and negative for extraction); and b (L) is the screened interval of the well (also the aquifer thickness). The groundwater flux is assumed to be the vertical average across the entire aquifer thickness.

2.2 Reactions

2.2.1 Oxidation

The oxidation of dissolved NAPL species by an oxidant (permanganate or persulfate) is assumed to be represented by an irreversible second-order reaction expression given by

$$G_i^{ox} = -\theta k_i C_i C_{ox} \tag{2-3}$$

where C_i (M/L^3) is dissolved concentration of the NAPL species i; C_{ox} (M/L^3) is the oxidant concentration; and k_i ($L^3/M \cdot T$) is the second-order rate coefficient with respect to the oxidant. Equation (2-3) represents the rate of mass decrease in each NAPL species due to oxidation.

Similarly the consumption of an oxidant by the reaction with the dissolved NAPL species is represented by

$$G_i^{ox} = -\sum_{i=1}^{nc} \theta k_i \beta_i C_i C_{ox} \tag{2-4}$$

where nc is the total number of NAPL constituents; and β_i (M/M) represents the stoichiometric mass ratio of oxidant per mass of dissolved species i. Equation (2-4) represents the total rate of oxidant mass consumed by the suite of dissolved NAPL species.

The form of Equations (2-3) and (2-4) are consistent with rate laws developed between permanganate and several dissolved chlorinated NAPL species (Yan and Schwartz, 1999; Hood et al., 2000; Huang et al., 2002), and between persulfate and chlorinated ethenes (Waldemer, Tratnyek, Johnson, & Nurmi, 2007).

2.2.2 NAPL Dissolution

NAPL dissolution is assumed to follow the theory of Borden and Kao (1992) where residual NAPL is distributed between two mass transfer limited regions: a fast region with a higher mass transfer rate, and a slow region with a slower mass transfer rate. This dual region NAPL dissolution model can be expressed as

$$G_i^{diss} = \theta\lambda_{fast}(C_{s,i}^{fast} - C_i) + \theta\lambda_{slow}(C_{s,i}^{slow} - C_i) \quad (2\text{-}5a)$$

with $$C_{s,i}^{fast/slow} = C_i^{sat} \cdot x_i^{fast/slow} \Big/ \left(f^S / f^L\right)_i \quad (2\text{-}5b)$$

where λ_{fast} and λ_{slow} (1/T) represents the mass transfer rate coefficients for the fast and slow NAPL regions respectively; $C_{s,i}$ (M/L^3) represents the effective solubility; x_i represents the mole fraction; C_i^{sat} (M/L^3) is the maximum aqueous concentration; and f^S/f^L (unitless) is the ratio of solid/liquid reference fugacities (J. F. Pankow & Johnson, 1996).

Depletion of mass from the fast or slow NAPL regions is expressed by

$$\frac{dM_i^{fast/slow}}{dt} = -\theta\lambda_{fast/slow}(C_{s,i}^{fast/slow} - C_i) \quad (2\text{-}6)$$

where M_i represents the mass of NAPL species *i*. The fast and slow NAPL regions consist of two nondiscrete NAPL fractions. Research has indicated the importance for consideration of two separate fractions (Malone, Kao, & Borden, 1993). The actual distribution of NAPL between the two fractions cannot be directly measured (Malone et al., 1993). Commonly the percentage of NAPL in each region is obtained by adjusting the parameters until a good fit is obtained between simulated and laboratory column tests.

2.2.3 NOI Reactions

2.2.3.1 Permanganate

Permanganate NOI can be expressed by a natural oxidant demand (NOD). The NOD represents the consumption of permanganate by uncontaminated aquifer material and is expressed as the grams of permanganate consumed per kilogram of aquifer solids. Naturally occurring organic OAM behaves as a significant permanganate sink, reducing both the amount of permanganate available for the destruction of contaminants and the overall rate of oxidation (Mumford et al., 2004). Batch experiments examining temporal permanganate degradation by OAM indicated that the OAM is consumed by an initial fast consumption rate followed by a persistent slower consumption rate (Xu & Thomson, 2008). The main factors controlling permanganate consumption include mass loading ratio, the initial permanganate concentration, and the nature and quantity of reduced aquifer material species. A high degree of correlation was observed

between the maximum NOD and the OAM content implying that organic carbon is the major reduced species contributing to permanganate consumption for aquifer materials (Xu & Thomson, 2009). The kinetic expressions are given by

$$G_{\mathrm{MnO}_4}^{NOI} = -k_{\mathrm{MnO}_4}^{fast}\theta C_{OAM}^{fast} C_{\mathrm{MnO}_4} - k_{\mathrm{MnO}_4}^{slow}\theta C_{OAM}^{slow} C_{\mathrm{MnO}_4} - k_{\mathrm{MnO}_2}\theta C_{\mathrm{MnO}_4} \quad (2\text{-}7a)$$

with $$G_{OAM_{fast}}^{NOI} = -k_{OAM}^{fast}\theta C_{OAM}^{fast} C_{\mathrm{MnO}_4} \quad (2\text{-}7b)$$

$$G_{OAM_{slow}}^{NOI} = -k_{OAM}^{slow}\theta C_{OAM}^{slow} C_{\mathrm{MnO}_4} \quad (2\text{-}7c)$$

where C_{OAM}^{fast} and C_{OAM}^{slow} (M/L^3) is the concentration of the fast and slow fraction of the OAM expressed as mass of OAM per volume of system; k_{ox}^{fast} and k_{ox}^{slow} (L^3/M·T) represent the fast and slow reaction rate coefficients with respect to permanganate; k_{OAM}^{fast} and k_{OAM}^{slow} (L^3/M·T) represent the fast and slow reaction rate coefficients with respect to OAM, k_{MnO_2} (1/T) is the reaction rate coefficient for the reaction catalyzed by the oxidant by-product (for permanganate, manganese dioxide – MnO_2).

The bulk OAM is comprised of two discrete regions, a fast reacting OAM fraction ($C_{OAM}^{fast}/C_{OAM}^{total}$), and the slow reacting OAM fraction (1- $C_{OAM}^{fast}/C_{OAM}^{total}$). OAM is represented as the chemical oxygen demand (COD) (g/kg) and the concentrations of C_{OAM}^{fast} and C_{OAM}^{slow} are estimated as a product of the COD, the percentage of OAM in the fast or slow fraction, and the bulk density.

The OAM reaction coefficients k_{OAM}^{fast} and k_{OAM}^{slow} are related to k_{ox}^{fast} and k_{ox}^{slow} through the stoichiometric ratio of permanganate mass required per unit mass of OAM (g of MnO_4/g of OAM), as given by (Xu & Thomson, 2009)

$$\beta^{fast} = \frac{k_{ox}^{fast}}{k_{OAM}^{fast}}, \text{ and } \beta^{slow} = \frac{k_{ox}^{slow}}{k_{OAM}^{slow}} \quad (2\text{-}8)$$

The reduction of permanganate yields manganese oxides that precipitate at the reaction sites on the sediment grains and leads to passivation of the aquifer material (Xu & Thomson, 2008). In the model, passivation is accounted for by decreasing the reaction rate coefficient for the slow

reacting OAM. This is equivalent to increasing the diffusional resistance through a solid layer. The empirical linear expression suggested by Xu et al., (2009) is given by

$$k_{ox}^{slow}(t) = k_{ox,init}^{slow} - k_p\left[\frac{m_{MnO_2}(t)}{m_{solids}}\right] \quad (2\text{-}9)$$

where $k_{ox,init}^{slow}$ ($L^3/M\cdot T$) is the initial reaction rate coefficient with respect to the slow reacting OAM; k_p ($L^3/M\cdot T$) is an empirical reduction factor associated with the passivation process; and m_{MnO_2} (M) is the mass of manganese oxides produced as a function of time. The permanganate mass consumed by the sediments can be used to estimate m_{MnO_2}.

2.2.3.2 Persulfate

Unactivated persulfate NOI manifests as an enhanced decomposition rate with only a slight decrease in the NOM content of aquifer solids (Thomson, 2010). While permanganate NOI behaviour can be described by a NOD, the repeated decomposition behaviour of persulfate yields an infinite interaction (infinite NOD). The kinetic expression adapted from by Sra et al. (2010) for unactivated persulfate NOI behaviour is expressed as

$$G_{S_2O_8}^{NOI} = -k_{obs}\gamma_{i,S_2O_8}\gamma_{i,react}^{1.5}C_{S_2O_8^{2-}} \quad (2\text{-}10a)$$

$$k_{obs} = k_{cat}C_{cat}^{\ n_{cat}} + k_{NOM}C_{NOM}^{\ n_{NOM}} \quad (2\text{-}10b)$$

where γ (unitless) represents the activity coefficient for persulfate and the reactant (NOM represented as total organic carbon) (Sra et al., 2010); k_{cat} is the mineral catalyzed reaction rate coefficient; k_{NOM} is the NOM reaction rate coefficient; n_{cat} and n_{NOM} are the reaction orders with respect to the catalysts and the NOM, respectively; C_{cat} (M/L^3) is the solids catalyst concentration which can be represented by amorphous iron (Fe_{Am}); and C_{NOM} (M/L^3) is the solids NOM concentration represented by the total organic carbon (TOC). Activity coefficients are estimated using the extended Debye-Hückel approximation (J. Richard Elliott & Lira, 1999) and the initial persulfate ionic strength. For simplicity the model assumes that the reaction order with respect to persulfate is unity for all reactions, and C_{cat} and C_{NOM} remain constant (Sra et al., 2010).

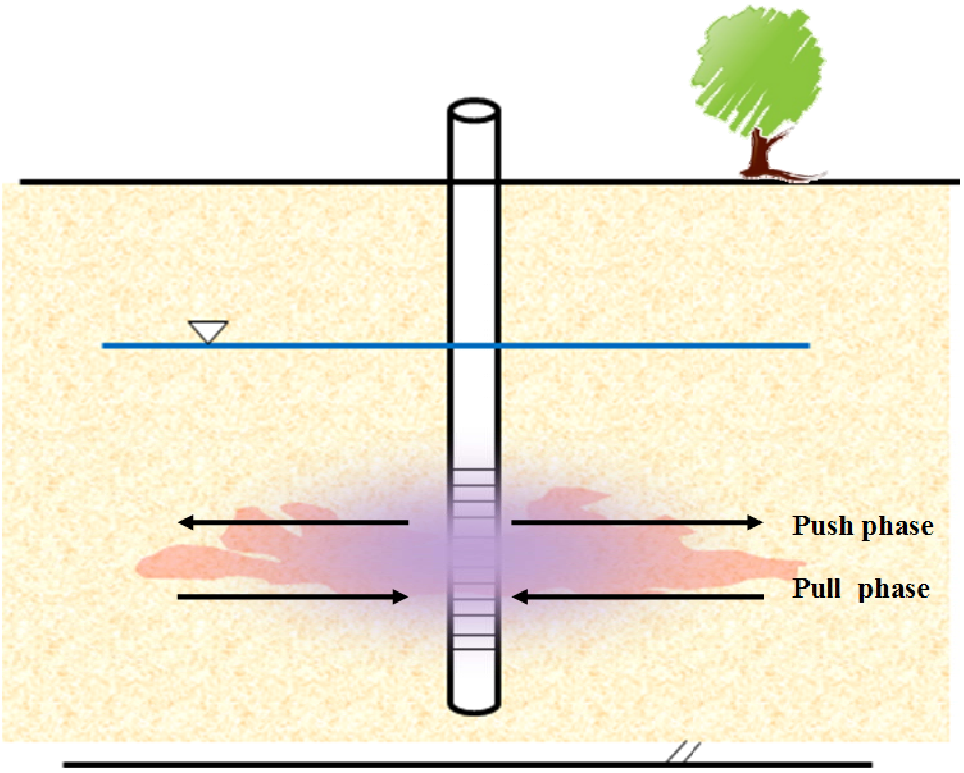

Figure 2-1. Conceptual illustration of PPT in a contaminated aquifer system. Injection solution is shaded purple. Residual NAPL contamination is shaded red.

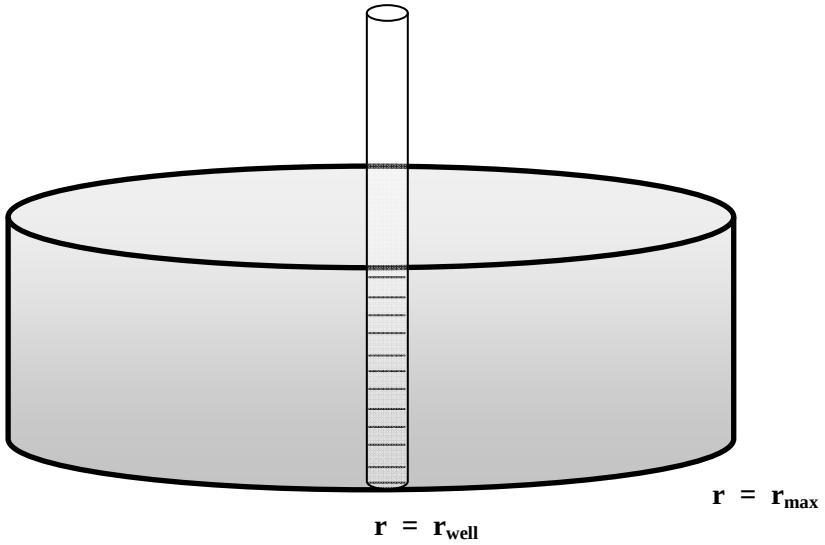

Figure 2-2. Idealization of PPT domain

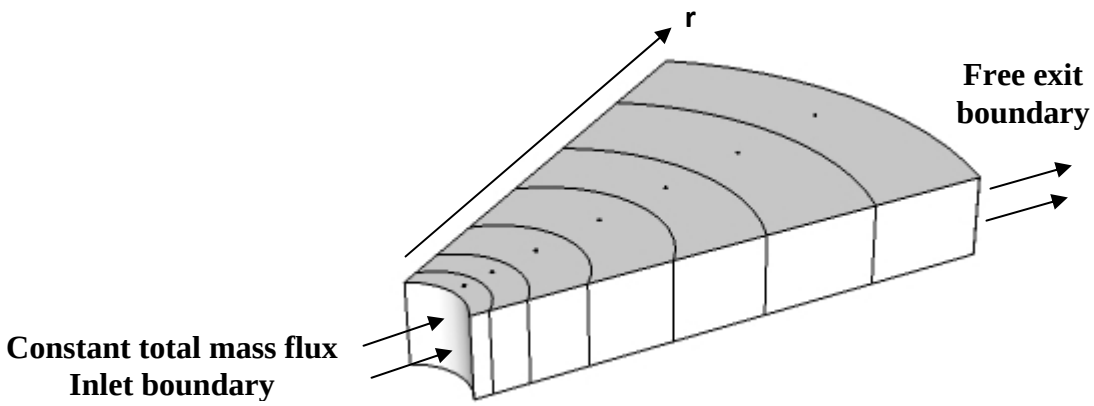

Figure 2-3. Numerical Details for PPT model during injection phase

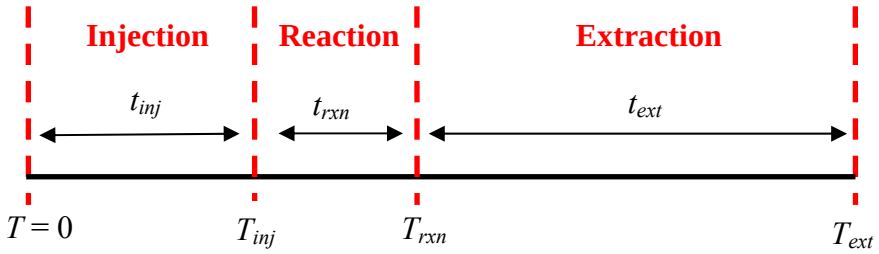

Figure 2-4. Schematic showing the notation of the different phases in a typical PPT

2.3 Numerical Model (PPT-ISCO)

The model was developed to simulate a complete PPT as it progresses through the three different phases: (1) the injection phase, (2) the reaction phase and (3) the extraction phase. During the first and third phases, groundwater velocity (v) is a function of the well flow rate. For the reaction phase the groundwater velocity is set to zero and diffusion remains the only active transport process.

The model domain (Figure 2-2) was divided into a finite number of control volumes (n_{CV}). The boundaries of control volumes are positioned mid-way between adjacent nodes. Thus each node is surrounded by a control volume (Versteeg & Malalasekera, 2007). Expanding control volumes following a geometric progression were used to provide for a higher resolution near the well bore (Figure 2-3). The external boundary of each CV follows the expansion expression given by

$$r_{i+1} = \alpha\, r_1 \tag{2-11}$$

where α represents the geometric expansion ratio; and r_1 is the well radius (r_{well}). The size of the computational domain (r_{max}) is a function of the well radius and α

$$r_{\max} = r_1 \alpha^{n_{CV}} \tag{2-12}$$

The time step intervals also follow a geometric progression as given by

$$\Delta t_{i+1} = \beta \Delta t_i \tag{2-13}$$

where β represents the geometric time step expansion ratio. This allows for short time steps at early times and longer time steps at later times. The time step increment is reset to the inital Δt at the start of each PPT phase.

The governing equations were integrated over each control volume to obtain a mass conservative expression discretized at each nodal point (Versteeg & Malalasekera, 2007). The model includes either an exponential weighting or second-order central weighting scheme to represent the advective flux term (Patankar, 1980). Control volumes adjacent to the domain boundaries are modified to incorporate the boundary conditions (Section 2.3.1). The resulting system of linear algebraic equations is solved using the tri-diagonal matrix algorithm to obtain the distribution of

C_i at the nodal points (Anderson, Tannehill, & Pletcher, 1984). Details of the numerical method and weighting schemes are provided in Appendix C.

2.3.1 Initial and Boundary Conditions

Prior to the start of a PPT simulation, it is assumed that the background concentration for the injection solution in the aquifer is zero. The initial conditions for solving Equation (2-1) are given by

$$C_i(r, t=0) = 0 : r_{well} \le r < r_{\max} \tag{2-14}$$

where C_i is the oxidant, tracer or by-product concentration. The boundary conditions used during the injection and extraction phases are different, since both Q and v are positive during the injection phase, and negative during the extraction phase (Figure 2-4). During the injection phase a constant total mass flux boundary condition is applied at the inlet and a free-exit condition (Frind, 1988) was applied at the outlet (r_{max}) as given by

$$\left(qC_o - \theta D \frac{\partial C}{\partial r} \right) = q\, C_o : 0 < T < T_{inj} \tag{2-15a}$$

$$\left(qC_e - \theta D \frac{\widetilde{\partial C}}{\partial r} \right) = J_{ext} : 0 < T < T_{ext} \tag{2-15b}$$

where T_{inj} is the injection time; T_{ext} is the extraction time; C_o is the concentration of the injected solution; C_e represents the concentration at the outlet boundary; D represents the hydrodynamic dispersion coefficient $(\alpha_r q + D_d^*)$; $\frac{\widetilde{\partial C}}{\partial r}$ represents the diffusive flux approaching the outlet, estimated from inside of the domain; and J_{ext} represents the total flux (advective and dispersive) exiting from the outlet. During the reaction phase a free exit condition is also applied at the outlet, and a similar inlet boundary condition was used since the only active transport process is diffusion.

$$\theta D \frac{\partial C}{\partial r} = 0 \ : T_{inj} < T < T_{rxn} \tag{2-16}$$

where T_{rxn} is the reaction time. During the pull phase the boundary condition at the well screen is obtained from a mass balance in the well (Zlotnik & Logan, 1996). With this condition the extracted concentration (C_w) is a function of the extraction flow rate, as well as the advective and dispersive fluxes, expressed by

$$0 = \left(\theta D \frac{\partial C}{\partial r} - qC_w \right) 2\pi r_{well} b - QC_w : T_{rxn} < T < T_{ext} \qquad (2\text{-}17)$$

2.3.2 Solution Method

For simplicity, the reactive transport equations (Equation 2-1) were solved using the Strang-splitting operator approach (Strang, 1968). In this approach, the advective-dispersive transport equation is solved over a half-time step (Δt /2). The reaction processes are then solved over the entire time step (Δt) using the Euler method for the dissolution (Equation (2-5a) and oxidation reactions (Equation 2-3), and using the forth-order Runge Kutta method for the consumption of oxidant by the NOI (Equation 2-7 or Equation 2-10a) and dissolved NAPL constituents (Equation 2-4) (Spiegel, 1958). The combination of these two methods was used to easily adapt to variations in the number of NAPL components and to simplify the coupled non-linear nature of the oxidant expression due to the NOI and NAPL oxidation. The advective-dispersive transport equations are then solved again over the remaining half-time step (Δt/2). The method is suitable for small time steps (Carrayrou, Mosé, & Behra, 2004; J.J. & J., 1995).

Mass balance calculations are completed for the oxidant and selected NAPL species at the conclusion of each PPT simulation. The oxidant (or tracer) mass balance error (M^{ox}_{error}) is expressed as

$$M^{ox}_{error} = \left(\frac{M^{ox}_{inj} - M^{ox}_{ext} - M^{ox}_{storage} - M^{ox}_{consumed}}{M^{ox}_{inj}} \right) \times 100 \qquad (2\text{-}18)$$

where M_{inj}^{ox} represents the mass of oxidant injected; M_{ext}^{ox} represents the mass of oxidant extracted; $M_{storage}^{ox}$ represents the mass of oxidant remaining in the system; and $M_{consumed}^{ox}$ represents the mass of oxidant consumed by the NAPL species and/or NOI.

The mass balance error for the selected NAPL species (M_{error}^{NAPL}) is expressed as

$$M_{error}^{NAPL} = \left(\frac{M_{initial}^{NAPL} - M_{final}^{NAPL} - M_{net\ dissloved}^{NAPL}}{M_{initial}^{NAPL}} \right) \times 100 \qquad (2\text{-}19)$$

where $M_{initial}^{NAPL}$ represents the mass of the NAPL species in the fast and slow NAPL regions prior to the start of the PPT; M_{final}^{NAPL} represents the mass remaining at the completion of the PPT; and $M_{net\ dissloved}^{NAPL}$ represents the net amount (into and out of the fast and slow regions) of mass dissolved during the PPT. An additional mass balance is completed for each time step to account for the total mass of NAPL species (present in the fast and slow regions and dissolved) in the system.

2.4 Model Benchmarking Efforts

Three examples that benchmark the conservative transport and NOI components of the developed model are presented in this section.

2.4.1 Example 1- Conservative Transport

The results from the developed PPT-ISCO model were compared with the following approximate analytical solution for the one-dimensional radial transport of a conservative tracer developed by (Gelhar & Collins, 1971):

$$\frac{C}{C_o} = \frac{1}{2} erfc \left[\left(\frac{V}{V_{inj}} - 1 \right) \Big/ \left\{ \frac{16}{3} \left(\frac{\alpha_r}{r_{\max}} \right) \left(2 - \left| 1 - \frac{V}{V_{inj}} \right|^{1/2} \left(1 - \frac{V}{V_{inj}} \right) \right) \right\}^{1/2} \right] \qquad (2\text{-}20a)$$

with $$r_{\max} = \sqrt{\frac{Qt_{inj}}{\pi b \theta}} \qquad (2\text{-}20b)$$

where Q_{inj} (L^3/T) represents the injection flow rate; Q_{ext} (L^3/T) represents the extraction flow rate; V (L^3) represents the cumulative extracted volume calculated as $|Q_{ext}|t$; V_{inj} (L^3) is the total injected volume calculated as $Q_{inj}t_{inj}$; and b (m) is the screened interval of the well.

The upper limit of applicability for Equation (2-19) is $\varepsilon << 0.01$, where $\varepsilon = \alpha_r/2r_{max}$. Input parameters (Table 2-1) were selected based on the unconfined aquifer at Canadian Forces Base (CFB) Borden located in Alliston, Ont., Canada. The analytical solution was compared against model solutions using the exponential or second-order central scheme (Figure 2-5).

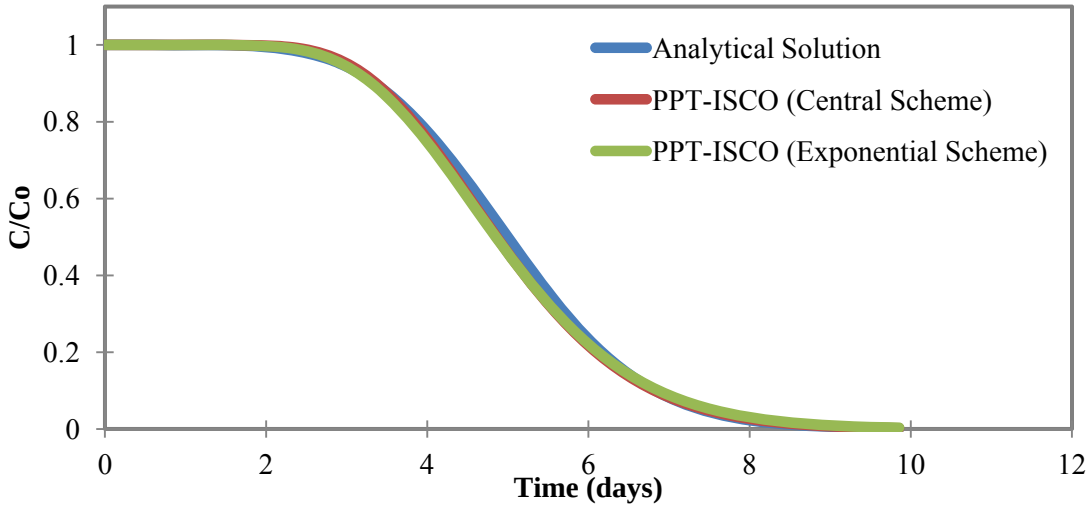

Figure 2-5. Comparison of results obtained from ISCO-PPT with approximate analytical solution proposed by Gelhar and Collins (1971) for radial flow in an aquifer with advection and dispersion (uniform mesh)

Both schemes exhibit solutions that are nearly identical to the analytical solution with $\varepsilon = 0.0068$. The tracer mass balance error for both schemes was < 0.1%. In this comparison the computational domain was discretized into a uniform radial grid with 0.01m spacing ($\alpha = 1.0$). The match between the analytical solution and numerical model highlights the accuracy of the developed model and the selected numerical schemes. Differences between the schemes become apparent when applying the comparison to a radially expanding grid ($\alpha = 1.05$) (Figure 2-6).

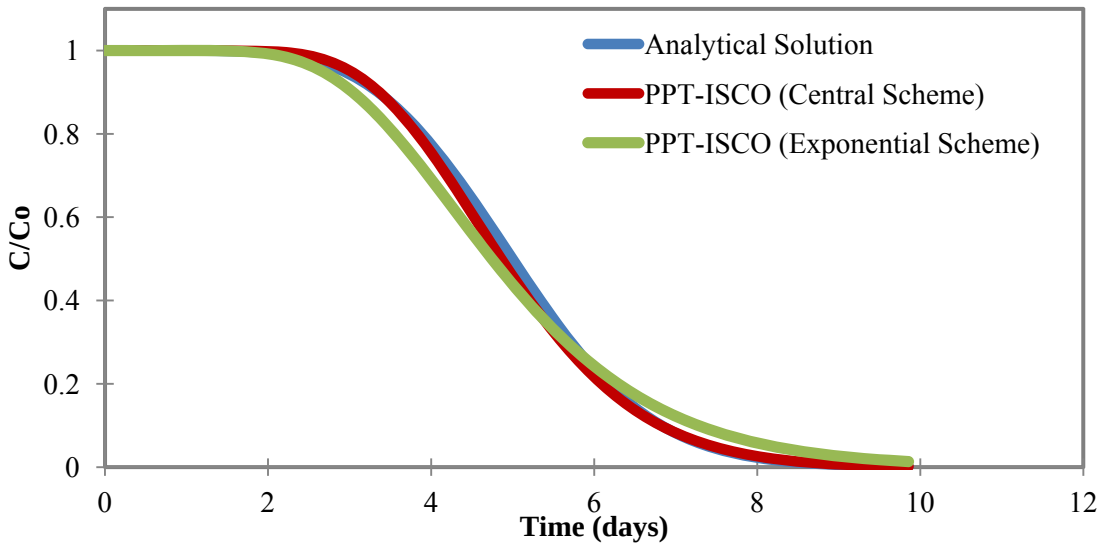

Figure 2-6. Comparison of results obtained from PPT-ISCO with approximate analytical solution proposed by Gelhar and Collins (1971) for radial flow in an aquifer with advection and dispersion (radially expanding grid)

The central scheme yields a solution very similar to the analytical solution, whereas the exponential scheme shows some numerical dispersion with $\varepsilon = 0.0068$. The tracer mass balance error for both schemes was < 0.1%. The exponential scheme reverts to the first-order upwind scheme where large gradients in grid spacing exist, which is known to produce numerical dispersion. It is important to note the classic second-order central method is viable only for low grid Péclet numbers which may not always be feasible for PPT scenarios because of the high advective flux that occurs during the injection and extraction phases. In this comparison the Péclet number does not exceed 2 to allow for a physically realistic solution with the second-order central scheme. Due to this limitation the second-order central method is prone to unphysical solutions exhibiting numerical oscillations. The exponential scheme is a more robust solution that is noted for its algorithmic simplicity, fast convergence, and physical solutions for any Péclet number (Leonard & Drummond, 1995). The scheme is only accurate for steady, quasi-one dimensional flow (when the grid is aligned with the main flow direction) (Leonard & Drummond, 1995) which is the case for this formulation.

The conservative transport simulations were simulated with an initial Δt of 1 second. Increasing the initial time step to 1 minute for both the second-order central and exponential schemes yields no significant change in accuracy and the mass balance error remains < 0.1%. For an initial time step of 1 hour, the solutions for both schemes begin to exhibit numerical oscillations ($C/C_o > 1.0$)

as a result of the Crank- Nicolson method. Computation time with $\Delta t = 1$ second and $\Delta t = 1$ minute does not vary significantly, and is set at 1 second.

Variations in the time step expansion ratio ($\beta = 1.00005$ to 1.005) yielded a small change in the mass balance error (from 0.1% to 0.2%). The solution at the high values of β is qualitatively very similar to $\beta = 1.00005$. Variations in grid spacing ($\alpha = 1.05$ to 1.5) yielded a small degree of change (from < 0.1% to 0.2%) to mass balance errors for conservative transport (Appendix C). However qualitatively the BTCs obtained differ significantly from the analytical solution due to an increased amount of averaging occurring over the larger control volume sizes.

Table 2-1. Parameters used for Example 1: Verification of conservative transport

Parameter	Description	Value	Unit
Q	flow rate	0.1	m^3/d
t_{inj}	injection phase duration	5	d
t_{ext}	extraction phase duration	10	d
b	screened interval	1	m
θ	porosity	0.3	-
α_r	dispersivity	0.01	m
n_{CV}	total CVs in domain	80	-
α	mesh expansion ratio	1.05	-
β	time step expansion ratio	1.00005	-
r_{well}	well radius	0.025	m
r_1	initial grid step	0.025	m

2.4.2 Example 2- Permanganate NOI

Permanganate consumption by OAM was compared against PPT data collected in the field (Mumford et al., 2004). In this field exercise the PPTs were employed to estimate the permanganate NOD in an uncontaminated region of the saturated zone in the CFB Borden aquifer. Each PPT was estimated to have contacted a minimum of 270 kg of aquifer material. The input parameters for the comparison are listed in Table 2-2. For this simulation the duration

of the reaction phase is considered to be short enough that the effect of any ambient groundwater flow will not alter the migration of permanganate mass during the reaction phase.

The comparison between the model solution and field PPT data was completed in two steps. First, PPT-ISCO was fit to the conservative tracer BTC to determine the site-specific physical parameters (Figure 2-6a). The values for porosity (0.3 to 0.4) and dispersivity (0.01 to 0.04 m) were adjusted. In the second step PPT-ISCO is employed to produce the permanganate BTC using the OAM concentrations and kinetic rate coefficients estimated for the CFB Borden aquifer from batch tests (Xu & Thomson, 2009). A good agreement was obtained between the model results and the field BTC (Figure 2-7b) after a minor adjustment in k_{ox}^{fast} (from 0.14 to 0.16 L/g-day) was made. This increase is assumed to be reasonable based on the small variability associated with rate estimates obtained from batch tests. The match obtained is shown in Figure 2-7. The permanganate mass balance error was < 0.1%.

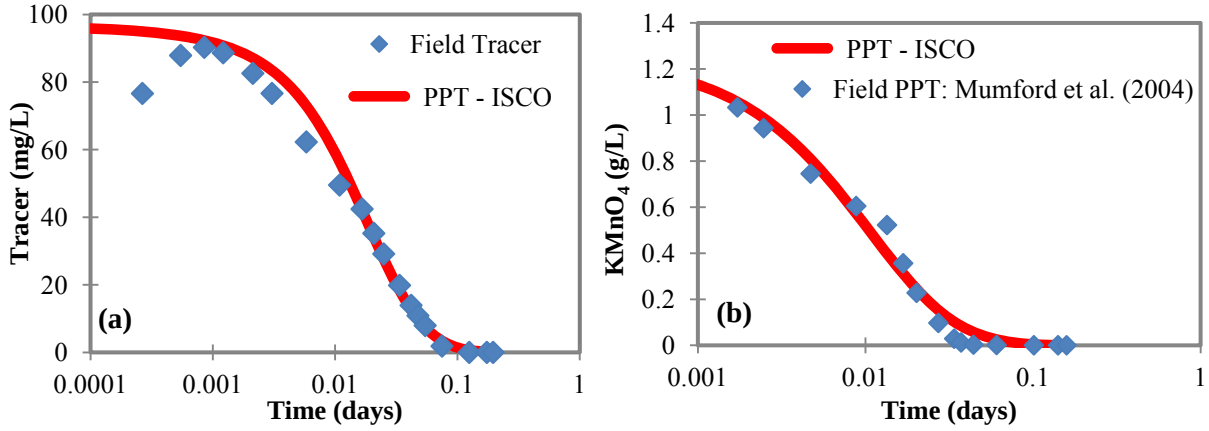

Figure 2-7. Comparison of results obtained from PPT-ISCO with (a) tracer field data and (b) permanganate field data (Mumford et al., 2004)

Table 2-2. Parameters used for Example 2: Permanganate consumption by OAM

Parameter	Description	Value	Unit	Source
Q_{inj}	injection flow rate	1.2	m^3/day	(Mumford et al., 2004)
Q_{ext}	extraction flow rate	3.0	m^3/day	(Mumford et al., 2004)
t_{inj}	injection phase duration	0.04	d	(Mumford et al., 2004)
t_{rxn}	reaction phase duration	1.9	d	(Mumford et al., 2004)
t_{ext}	extraction phase duration	0.15	d	(Mumford et al., 2004)
b	screened interval	1.0	m	-
θ	porosity	0.4[1]	-	(Brewster et al., 1995)
α_r	dispersivity	0.04[1]	m	(Sudicky et al., 1983)
ρ_b	sediment density	1.81	g/cm^3	(Mackay, Freyberg, Roberts, & Cherry, 1986)
C_{MnO4}	injected concentration	5.0	g/L	(Mumford et al., 2004)
C_{tracer}	injected tracer concentration	100.0	g/L	(Mumford et al., 2004)
OAM	bulk mass of OAM	6.96	g-$KMnO_4$/kg	(Xu & Thomson, 2009)
$C_{OAM}^{fast}/C_{OAM}^{total}$	OAM fast reacting fraction	56	%	(Xu & Thomson, 2009)
β^{fast}	stoichiometric mass ratio for fast fraction of OAM	6/21.4	-	(Xu & Thomson, 2009)
β^{slow}	stoichiometric mass ratio for slow fraction of OAM	14/21.4	-	(Xu & Thomson, 2009)
k_{ox}^{fast}	permanganate fast reaction rate coefficient	0.16[1]	L/g/day	(Xu & Thomson, 2009)
k_{ox}^{slow}	permanganate slow reaction rate coefficient	0.0058	L/g/day	(Xu & Thomson, 2009)
k_{MnO_2}	permanganate decomposition reaction constant	0.00001	1/day	(Xu & Thomson, 2009)
k_p	passivation factor	3.9	L/g-day	(Xu & Thomson, 2009)
n_{CV}	total CVs in domain	80	-	-
r_{well}	well radius	0.025	m	-
r_{max}	length of test domain	1.26	m	
α	mesh expansion ratio	1.05	-	-
β	time step expansion ratio	1.00005	-	-

1. Fitted parameters

2.4.3 Example 3- Persulfate NOI

Persulfate degradation was benchmarked against PPT data collected by Sra et al., (2010). In this case PPTs were also conducted in the saturated zone of the CFB Borden aquifer, but this time in a presumably no-drift, hydraulically isolated section of a sheet-pile walled gate. Sodium persulfate and a conservative tracer (lithium chloride) were injected and withdrawn periodically over 25 days. In the field, the well and tubing was purged a minimum of 3 times during each sampling interval. To simulate this PPT using PPT-ISCO, the reaction phase duration was set to zero, the extraction phase duration was set to 25 days and the extraction flow rate was adjusted until a good fit between the field tracer data and model results was achieved (see Table 2-3 for complete list input parameters). The total extracted volume obtained from PPT-ISCO is within an order of magnitude of the minimum extracted volume estimated from the well volume (purged 3 times at each sampling interval). The exact volume extracted during the experiment by Sra et. al., (2010) is not established because purging in excess of 3 volumes is reported and may also have taken place on non-sampling days. Reaction rate coefficients and concentrations for the mineral catalyst and NOM were estimated from batch experiments (Sra et al., 2010). Following model agreement with the conservative tracer (Figure 2-8(a)), a good match was achieved between the field and model persulfate BTCs as shown in Figure 2-8(b). The persulfate mass balance error was < 0.1%.

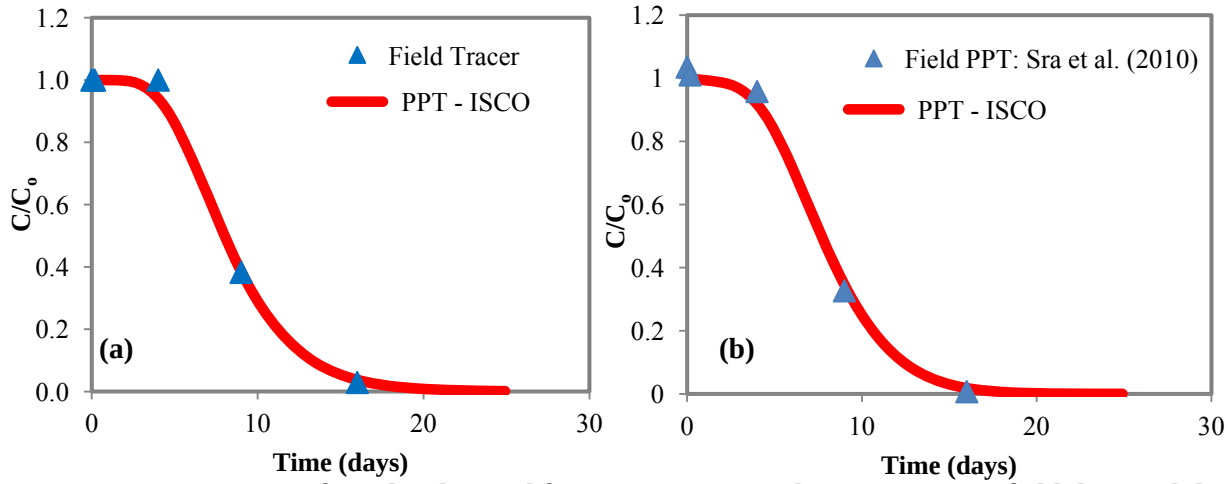

Figure 2-8. Comparison of results obtained from PPT-ISCO with (a) PPT tracer field data and (b) persulfate PPT field data from Sra et al., (2010)

Table 2-3. **Parameters used for Example 3: Persulfate consumption by NOM**

Parameter	Description	Value	Unit	Source
Q_{inj}	injection flow rate	0.50	L/min	(Sra et al., 2010)
Q_{ext}	extraction flow rate	0.01	L/min	-
t_{inj}	injection phase duration	0.167	d	(Sra et al., 2010)
t_{rxn}	reaction phase duration	0	d	(Sra et al., 2010)
t_{ext}	extraction phase duration	25	d	(Sra et al., 2010)
b	screened interval	1.0	m	-
θ	porosity	0.33	-	(Brewster et al., 1995)
α_r	dispersivity	0.01	m	(Sudicky et al., 1983)
ρ_b	sediment density	1.81	g/cm^3	(Mackay et al., 1986)
$C_{S_2O_8}$	injected oxidant concentration	20.0	g/L	(Sra et al., 2010)
C_{tracer}	injected tracer concentration	220.0	mg/L	(Sra et al., 2010)
C_{NOM}	solids NOM concentration	0.24	mg/g	(Sra et al., 2010)
C_{cat}	solids catalyst concentration	0.30	mg/g	(Sra et al., 2010)
k_{cat}	mineral catalyzed reaction rate coefficient	79.6×10^{-3}	-	(Sra et al., 2010)
k_{NOM}	NOM reaction rate coefficient	32.4×10^{-3}	-	(Sra et al., 2010)
n_{cat}	catalyst reaction order	1.5	-	(Sra et al., 2010)
n_{NOM}	NOM reaction order	1.5	-	(Sra et al., 2010)
n_{CV}	total CVs in domain	80	-	-
r_{well}	well radius	0.025	m	-
r_{max}	length of test domain	1.26	m	
α	mesh expansion ratio	1.05	-	-
β	time step expansion ratio	1.00005	-	-

2.5 NAPL Oxidation and Dissolution Processes

To illustrate the NAPL dissolution and oxidation processes, a PPT (see Table 2-4 for input parameters) was simulated with a permanganate injection of 20 g-$KMnO_4$/L into a contaminated aquifer at a rate of 1 m^3/day for 6 hours and (after a 0.5 day reaction phase) withdrawn continuously (at 4.5 m^3/day) over a period of 10 days. The duration of the extraction phase was selected to allow for observation of the rebound in NAPL component concentrations in the BTCs. The operating parameters were selected to correspond with values used in various PPTs (Haggerty et al., 1998; Mumford et al., 2004; M. H. Schroth & Istok, 2006; Sra et al., 2010).

The aquifer contains a residual NAPL (ρ_{NAPL} = 1.1 kg/L) which is uniform (S_{NAPL} = 1%) across the domain. The components of the NAPL include benzene, toluene, naphthalene and a bulk fraction. The properties of the NAPL components are provided in Appendix A. The aqueous concentration of the NAPL components is initially assigned to their respective maximum effective solubility limits. The domain is homogenous with respect to porosity and sediment density. The injection well (r_{well}) has a screened interval of 1.5 m. Consumption of the oxidant due to the NOI is neglected.

The simulations were completed using the exponential spatial weighting scheme, centered-in-time temporal scheme. Control volume and time step sizes were increased by a factor of 5% (α) and 0.005% (β) respectively. The initial Δt was set at 1 second. The results of these investigations are presented as PPT NAPL component BTCs (Figure 2-9), and fast (Figure 2-10) and slow (Figure 2-11) region NAPL mass profiles that feature representative NAPL components at a location within close vicinity to the injection well (0.04 m).

The results show that the NAPL component BTCs return to unity at a later time when oxidant is added (Figure 2-9). The delay in the dissolved concentrations returning to unity is a result of oxidation occurring in the system which serves to destroy the compound, lowering its dissolved concentration. The fast region NAPL mass profile highlights this oxidation reaction (Figure 2-10). A noticeable change in slope is apparent in the NAPL mass profiles at the time of transition from the injection phase to the reaction phase (0.25 days). For the case where oxidant is not added, the mass remaining in the fast and slow regions does not significantly change throughout the reaction phase. When oxidant is injected into the system, dissolution of NAPL mass from the

fast region is enhanced and continues during the reaction phase as oxidation processes remain active. At the conclusion of the test, 44% of the oxidant injected has been consumed by the NAPL compounds, and the remaining 56% was extracted during the pull phase of the test.

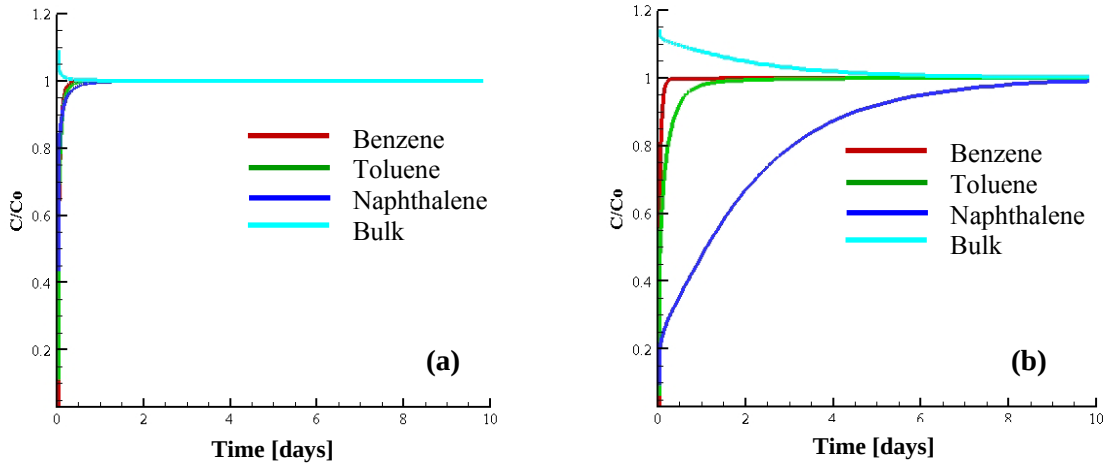

Figure 2-9. NAPL BTCs from simulated PPT without (a) and with (b) oxidant injection

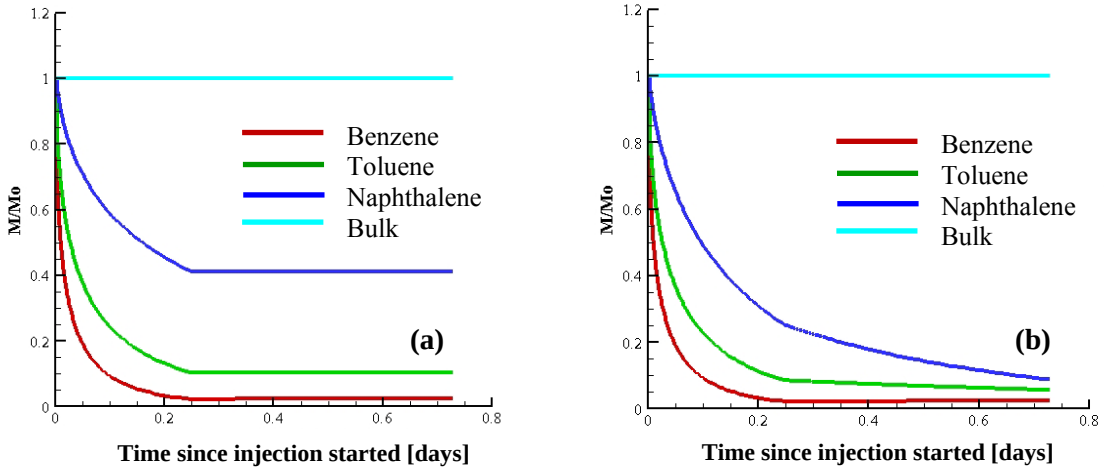

Figure 2-10. Fast region mass dissolution plots from simulated PPT without (a) and with (b) oxidant injection

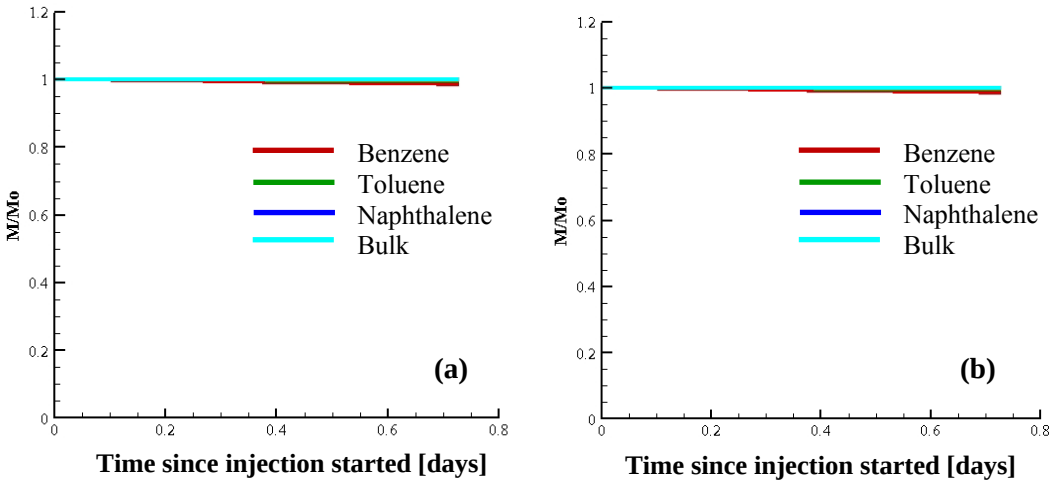

Figure 2-11. Slow region mass dissolution plots from simulated PPT without (a) and with (b) oxidant injection

Variations in control volume and time step sizes were examined to investigate how they impact the solution behaviour. Naphthalene was chosen as a representative compound due to its relatively high reaction rate with permanganate and its significant weight percentage within the residual NAPL. The solution presented for naphthalene (Figure 2-9(b)) is identified as the base case. Changing the control volume discretization to the uniform radial grid (α = 1.05 to 0.01m uniform spacing) that allowed for the least amount of numerical dispersion (Section 2.4.1) is identified as Case #1. Variations in grid spacing (α = 1.05 to α = 1.25) and the time step expansion ratio (β = 1.00005 to 1.05) is identified as Case #2 and Case #3, respectively.

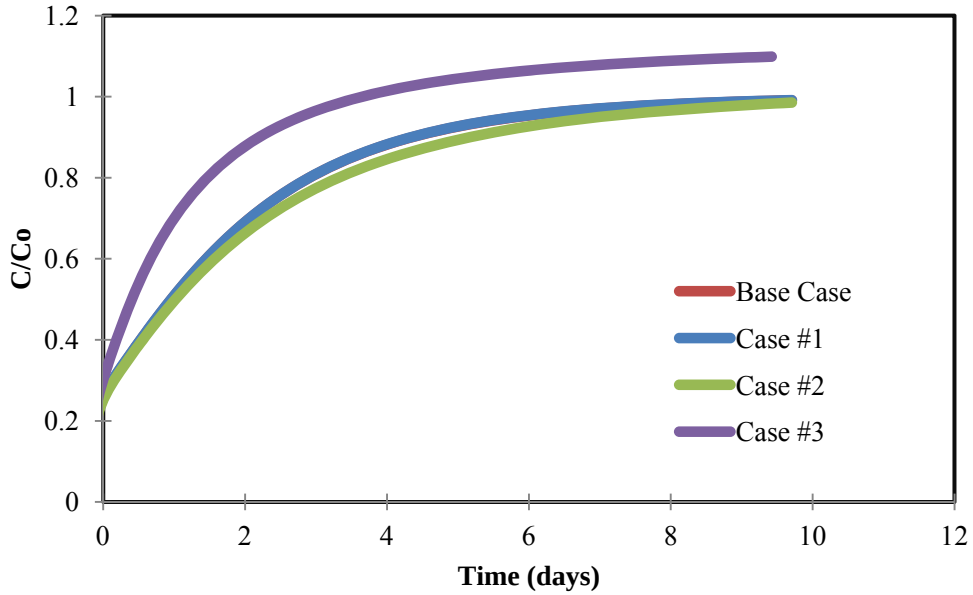

Figure 2-12. Naphthalene BTCs with grid and time step variations

The effect of changing the discretization schemes (from radially expanding to a very fine uniform radial spacing) does not manifest in the BTCs and suggests that the constant NAPL source suppresses the impact of numerical dispersion. The numerical model mass balance error for permanganate and naphthalene for both grid sizes were < 0.1%. After increasing the grid spacing the solution begins to vary from Case #1 due to a lower resolution near the well bore. The permanganate and naphthalene mass balance error remain < 0.1%. The most significant change in the solution occurs when the time step expansion ratio is increased. With this change the BTC exceeds a relative concentration of 1.0 and the mass balance error for permanganate increases to 12%. This error is attributed to the operator splitting method which requires small time steps due to the complexity of the reaction terms (Carrayrou et al., 2004; J.J. & J., 1995).

Table 2-4. Parameters used for residual NAPL simulations

Parameter	Description	Value	Unit
b	screened interval	1.5	m
r_{well}	well radius	0.025	m
θ	porosity	0.4	-
α_r	dispersivity	0.04	m
ρ_b	sediment density	1.81	kg/L
S_{NAPL}	NAPL saturation	1	%
ρ_{NAPL}	NAPL density	1.1	kg/L
$C_{ox}^{initial}$	$KMnO_4$ injection concentration	20	g/L
t_{inj}	injection duration	0.25	days
t_{ext}	extraction duration	10	days
Q_{inj}	injection flow rate	1	m^3/day
Q_{ext}	extraction flow rate	4.5	m^3/day
t_{rxn}	reaction phase duration	0.5	days
λ^{fast}	fast region mass transfer rate	10^5	day^{-1}
λ^{slow}	slow region mass transfer rate	0.01	day^{-1}
$\%fast$	% of total NAPL in fast region	75	%
n_{CV}	total CVs in domain	80	-
r_{max}	size of computational domain	1.26	m
α	mesh expansion ratio	1.05	-
β	time step expansion ratio	1.00005	-
$k_{benzene}$	second order rate coefficient for oxidation of benzene by permanganate	0.0	-
$k_{naphthalene}$	second order rate coefficient for oxidation of naphthalene by permanganate	$4.2x10^{-3}$	L/g-min
$k_{toluene}$	second order rate coefficient for oxidation of toluene by permanganate	$2.7x10^{-4}$	L/g-min
k_{bulk}	second order rate coefficient for oxidation of MGP bulk component by permanganate	0.0	-

3 PPTS To Examine NOI

As described (Section 1.0), PPTs have exhibited potential to capture *in situ* NOI behaviour (Mumford et al., 2004; Sra et al., 2010). As part of the investigation into the NOI of permanganate and persulfate, a sensitivity analysis was completed to understand how field PPT operating parameters and NOI kinetics influence the oxidant BTCs. Spatial profiles were examined to understand the distribution of oxidant after the injection and reaction phases, and to observe the changes in the NOM consumption. An analytical approach was also considered to examine if kinetics rates could be determined from the PPT BTCs, and to illustrate the effects of the reaction rate coefficients on PPT BTCs. Methods to estimate the NOD of permanganate were also investigated.

The PPT investigations explored here occur in a simulated aquifer system ('test zone') characterized by the CFB Borden aquifer. The site is homogeneous with respect to porosity and sediment density. The screened interval (b = 1 m) of the injection well (r_{well} = 0.025 m) is situated in the saturated zone. All simulations were completed using the exponential spatial weighting scheme, and centered-in-time temporal scheme. Control volume and time step sizes were increased by a factor of 5% (α) and 0.005% (β) respectively. The initial Δt was set as 1 second.

Calculations are performed for a "base case" and for additional cases (in the sensitivity analysis) where a single parameter is varied from the base case. Results for each case are presented as the relative concentration against extraction time, and the relative concentration against volume of solution extracted. Spatial distribution profiles are also provided for the base scenario. Base case values for t_{inj}, t_{rxn}, t_{ext}, Q_{inj}, and Q_{ext} were selected to be representative of values used in PPT experiments (Haggerty et al., 1998; Mumford et al., 2004; M. H. Schroth & Istok, 2006; Sra et al., 2010), and values for the initial oxidant concentration ($C_{ox}^{initial}$) are varied from 1 to 20 g/L to represent the range of values that may be used in the field to avoid significant density effects. All other relevant parameters (b, r_{well}, θ = 0.33, α_r = 0.01 m and ρ_b = 1.81 kg/L) are held constant for both the permanganate and persulfate investigations.

3.1 Permanganate

Permanganate PPT investigations were used to examine the link between the field operational and NOI parameters on resulting BTCs. The range of parameters investigated, and the base-case values (italicized) are presented in Table 3-1. The fraction of the fast OAM ($C_{OAM}^{fast}/C_{OAM}^{total}$) was assigned a value of 56% and was held constant in this analysis. This estimate is consistent with laboratory studies that measured the OAM fractions of eight representative aquifer solids and concluded that the fast OAM fraction was typically between 45-60% (Xu & Thomson, 2009). The variability in OAM selected is representative of the COD range observed by Xu et. al., (2009).

Table 3-1. Permanganate PPT parameters investigated

Parameter	Notation	Unit	Range
$KMnO_4$ injection concentration[1]	$C_{ox}^{initial}$	g/L	1,*5*,20
injection phase duration[1]	t_{inj}	-	10 minutes, *1 hour*, 12 hours
reaction phase duration[1]	t_{rxn}	-	5 hours, *2 days*, 10 days
injection flow rate[1]	Q_{inj}	m^3/day	0.5, *1*, 2
extraction flow rate[1]	Q_{ext}	m^3/day	0.3, *3*, 6
permanganate fast reaction rate coefficient[2]	k_{ox}^{fast}	L/g/day	0.005, *0.05*, 0.5
permanganate slow reaction rate coefficient[2]	k_{ox}^{slow}	L/g/day	0, 0.06, *0.006*
passivation factor[2]	k_p	L/g-day	0, *4*, 10
stoichiometric mass ratio (fast fraction)[2]	β_{fast}	g/g	0.15, *0.30*, 0.95
stoichiometric mass ratio (slow fraction)[2]	β_{slow}	g/g	0.15, *0.70*, 0.95
bulk oxidizable aquifer material[2]	OAM	g/kg	1, *7*, 50

1. Field operating parameter
2. NOI parameter

3.1.1 Spatial profiles

Spatial profiles illustrating the distribution and consumption of permanganate are presented for the base case, and for cases of increasing and decreasing reaction times (Figure 3-1). The tracer profile is also shown for comparison purposes. The fast and slow OAM fractions are presented as concentrations (Section 2.2.3.1). The spatial profiles illustrate the decrease in the fast and slow OAM fractions across the test zone as a result of permanganate consumption, and also highlight the extent and change in permanganate concentration with a variation in t_{rxn}.

The spatial profiles identify increased OAM consumption occurring within the vicinity of the well, where the permanganate concentration is highest. Since the OAM and permanganate consumption follow a second-order rate law, regions of lower permanganate concentration undergo a slower rate of OAM consumption. The profiles show that a majority (90%) of the OAM consumed is from the fast fraction, as a result of the larger fast fraction OAM kinetic rate coefficient, (k_{OAM}^{fast} related to k_{ox}^{fast} through Equation 2-8) compared to the slow fraction kinetic rate coefficient (k_{OAM}^{slow}). With increased reaction time, the OAM and permanganate concentrations decrease across the entire test zone. At the end of the longest reaction phase (Figure 3-1 (d)), 36% of the fast and 96% of the slow OAM fractions remain unconsumed. The small percent of the slow fraction of OAM consumed is a direct result of the magnitude of k_{OAM}^{slow} and also the passivation mechanism. Passivation decreased the C_{OAM}^{slow} consumed by 9% when compared to the base case simulation, and by 16% for a t_{rxn} of 10 days.

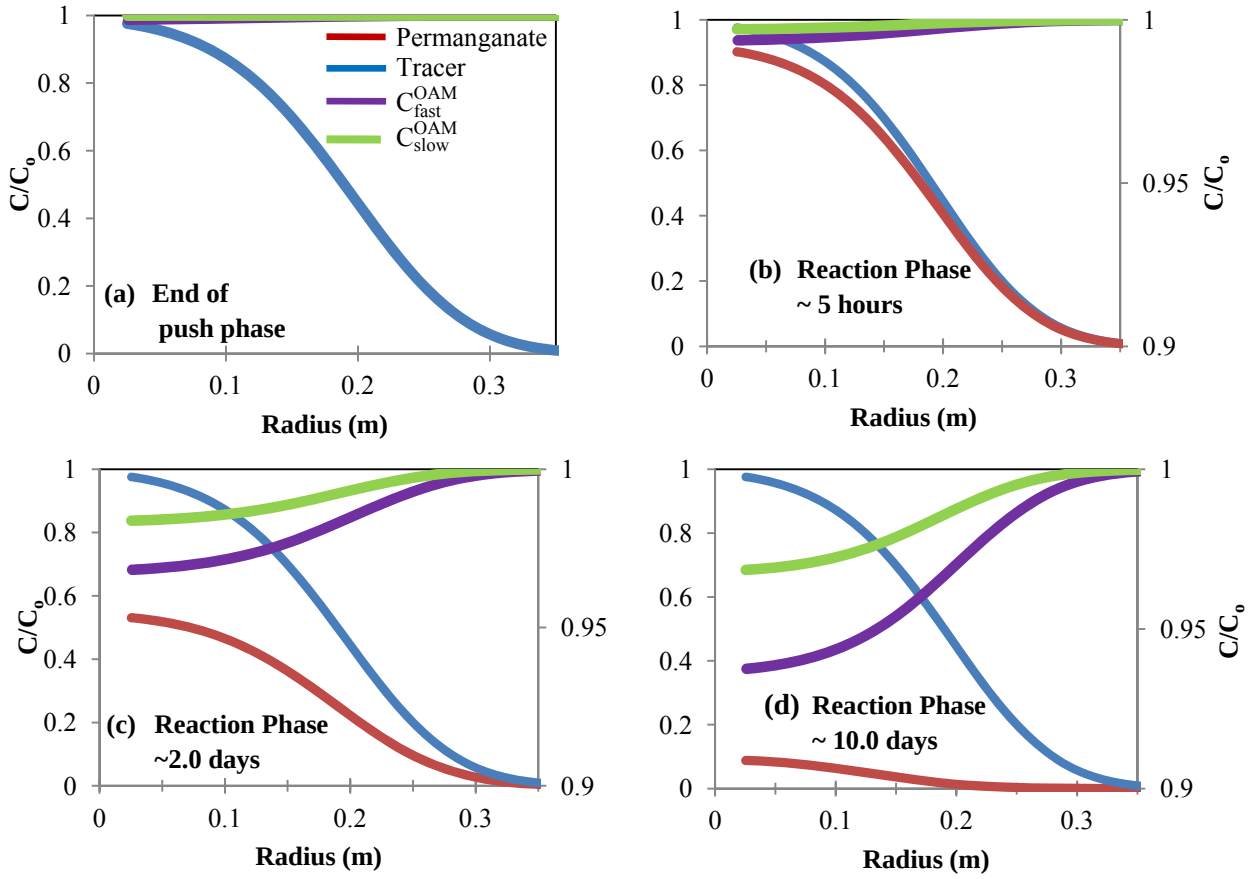

Figure 3-1. Spatial profiles of normalized permanganate, tracer , C^{OAM}_{fast} and C^{OAM}_{slow} concentrations at (a) the end of the push phase, and (b), (c), (d) after a reaction phase of 5 hours, 2.0 days and 10.0 days respectively. The C^{OAM}_{slow} concentration is presented on the right-hand axis.

3.1.2 Sensitivity Analysis

BTCs are presented for variations in the field operational (Figure 3-2) and NOI parameters (Figure 3-3). The scalability of the PPT BTCs to variations in the field operating parameters was examined. Additionally the BTCs were investigated for any distinguishable characteristics that may be related to permanganate reaction rate coefficients.

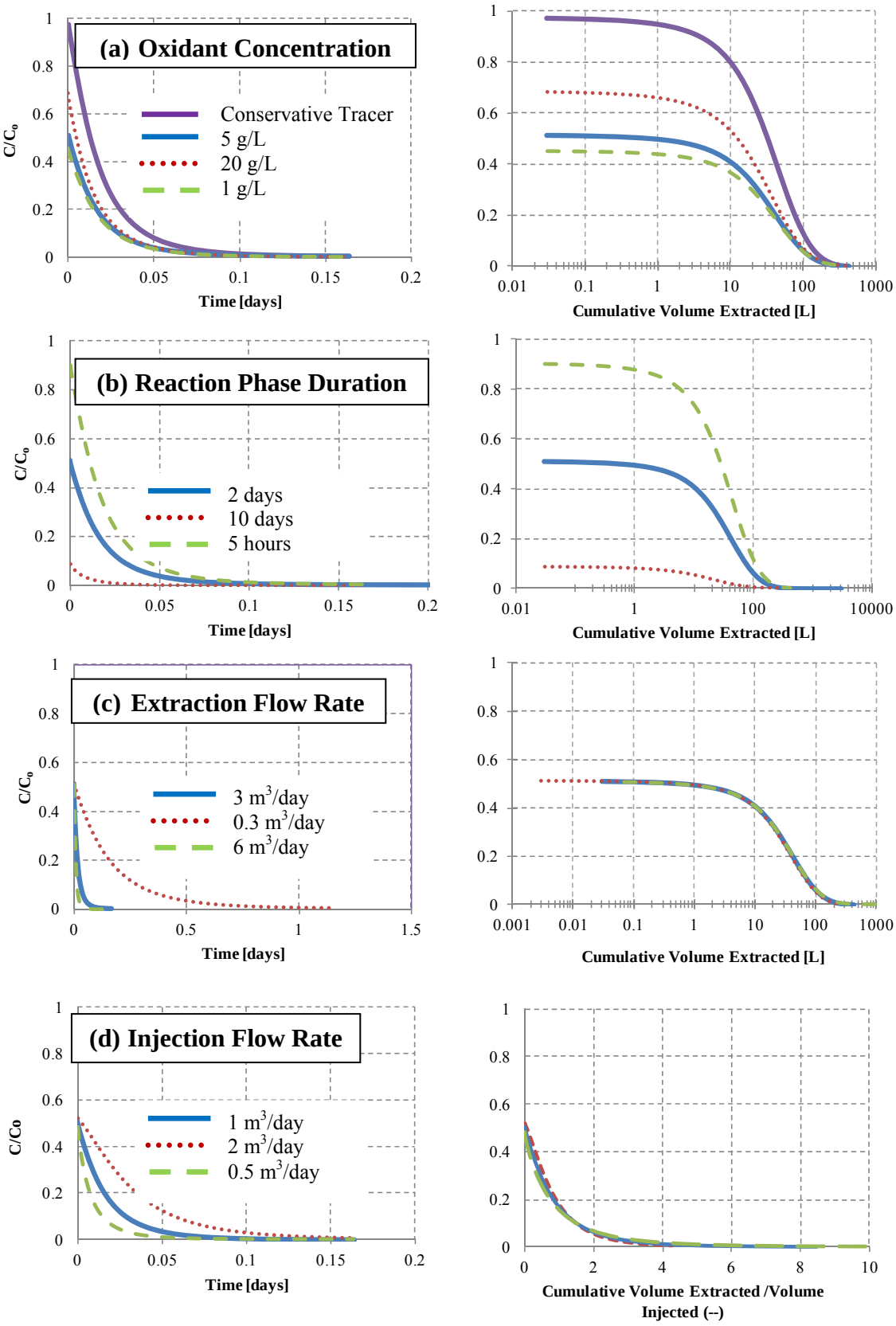

Figure 3-2. BTCs during the extraction phase of a PPT for various operating parameters. The base case is shown in blue.

PPT BTCs can be described as highly asymmetric and exhibiting long tails. Typically asymmetry is ascribed to rate-limited mass transfer in other physical situations, but in a PPT the BTC asymmetry is due primarily to the geometry of the flow field (Haggerty et al., 1998). Thus the results in Figure 3-2 show the effect of variations in the field operating parameters superimposed with the characteristics of the alternating PPT diverging/converging flow field.

Variations in the injected permanganate concentration ($C_{ox}^{initial}$) resulted in differences in the mass of permanganate being consumed by OAM (Figure 3-2(a)) in the test zone. Increasing the injected concentration to 20 g/L, increases permanganate consumption by 67%, while decreasing the injected concentration to 1 g/L, decreases permanganate consumption by 79% relative to the base case of 5 g/L. Since permanganate consumption follows a second-order mass rate law, increasing the permanganate concentration leads to higher consumption. Qualitatively, an increased permanganate dosage ($Q_{inj}C_{ox}^{initial}$) results in higher permanganate concentrations during extraction, causing the BTC to more closely resemble the conservative tracer BTC. An informative PPT will require a dosage that allows for enough of the injected permanganate mass to be consumed by the NOI so that the mass of tracer and permanganate extracted differentiates the permanganate BTC from the tracer BTC. To facilitate this, the dosage must be sufficient for some of the injected permanganate mass to remain in the test zone for extraction. If the oxidant is fully depleted before the extraction phase, any BTC analysis, of course, cannot be completed. Variations in the reaction phase duration (Figure 3-2(b)) also produce changes in the mass of permanganate consumed by the OAM. A t_{rxn} between 5 hours and 10 days resulted in the mass of injected permanganate consumed to increase from 9 to 95%.

Of the field operating parameters investigated, PPT BTCs can be scaled to variations in Q_{inj} and Q_{ext}. BTCs of varying extraction flow rates (Figure 3-2(c)) can be scaled to the cumulative volume extracted. The change in Q_{ext} primarily affects the extraction time required for the complete removal of excess permanganate from the aquifer system ($C/C_o < 0.01$). For example, reducing Q_{ext} from 5.0 to 0.3 m^3/day causes the extracted volume required to reach a relative concentration of approximately 0.1 to be reduced by only 5% (from 168 to 159 L). Thus an increase in the Q_{ext} has the same effect on the BTC as increasing the t_{ext} ($V_{ext} = Q_{ext}t_{ext}$). The mass extracted from the system is proportional to Q_{ext}.

Variations in Q_{inj} (Figure 3-2(d)) can be scaled to the cumulative volume extracted normalized by the volume of solution injected ($V_{inj} = Q_{inj}t_{inj}$). This is because the mass of aquifer material contacted by permanganate is proportional to the volume of oxidant injected. Small deviations exist between the BTCs due to a combination of increased dispersion ($q\alpha_r$) and a greater mass of permanganate injected for higher values of Q_{inj} (Equation 2-2).

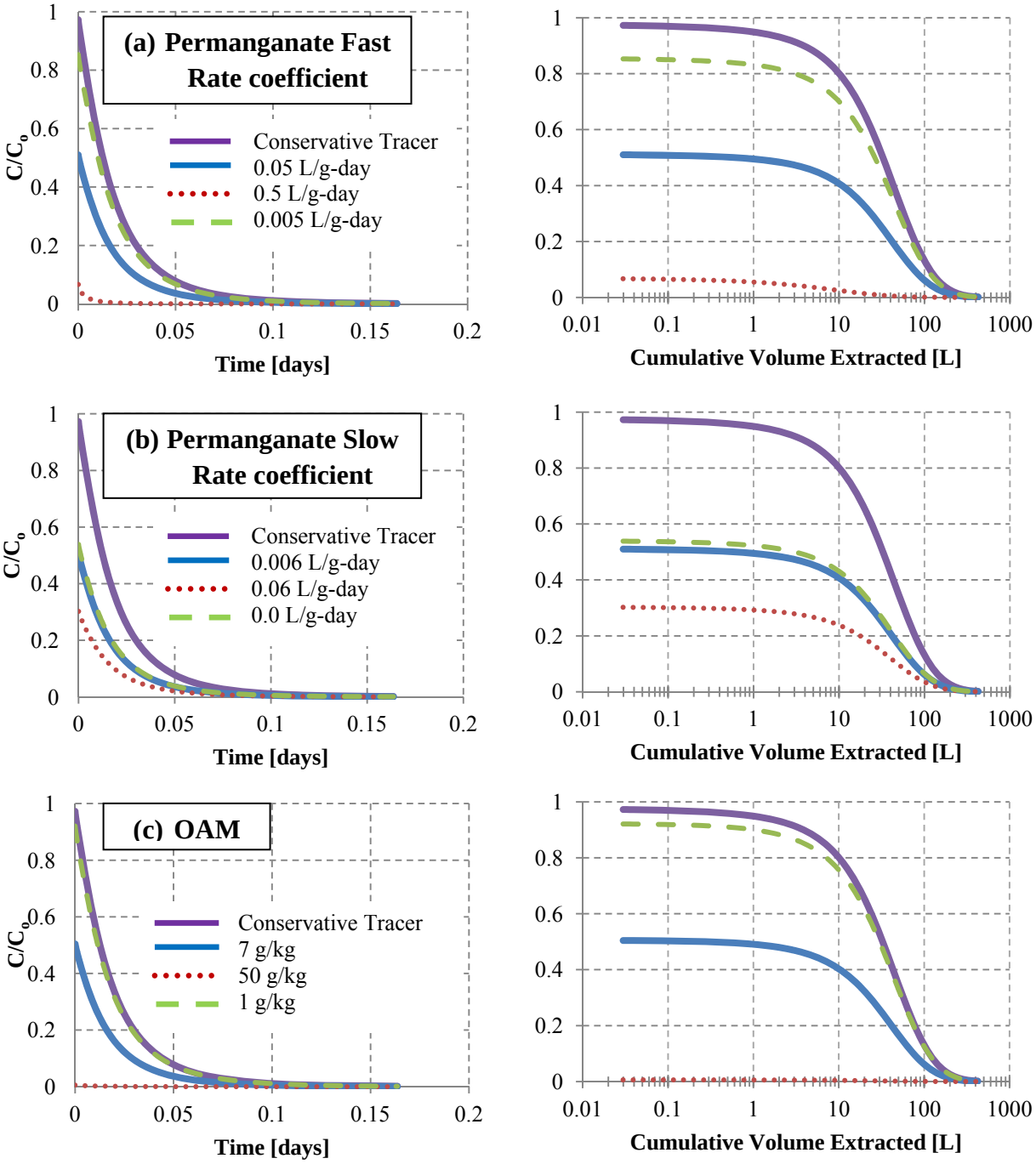

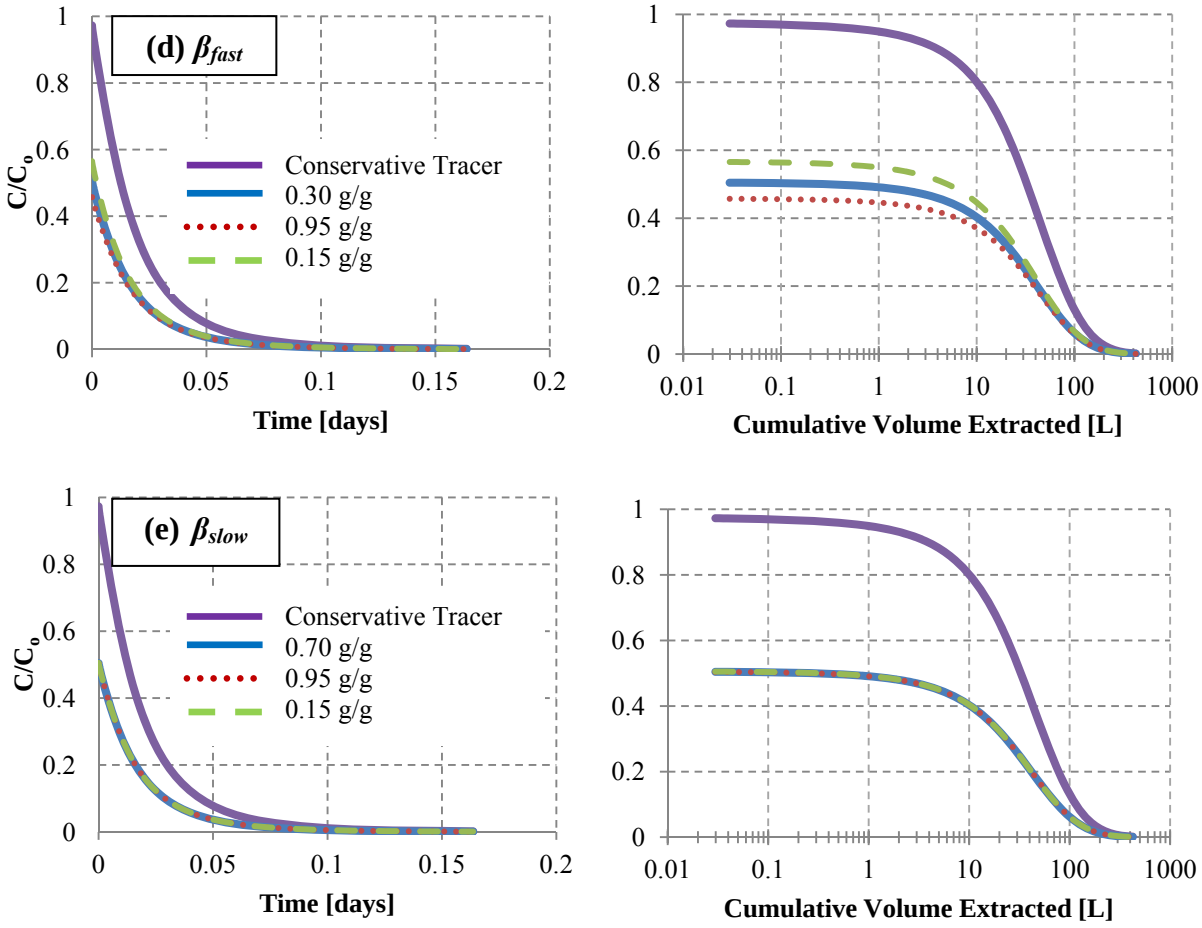

Figure 3-3. BTCs during the extraction phase of a PPT for various NOI parameters. The base case is shown in blue.

Variations in the permanganate reaction rate coefficients (Figure 3-3(a) and (b)) show that k_{ox}^{fast} is the controlling reaction rate coefficient that affects the shape of the permanganate BTCs. Increasing k_{ox}^{fast} by an order of magnitude increases the mass of permanganate consumed by approximately 50% (from 94 to 184 g of MnO_4^-). An order of magnitude decrease in k_{ox}^{fast} reduces the mass of permanganate consumed by 75% (from 94 to 23 g-MnO_4^-). The effect of reducing k_{ox}^{slow} (Figure 3-2(b)) to zero is minimal (< 10% change in permanganate consumption) and does not visually manifest in the BTCs. An order of magnitude increase in k_{ox}^{slow} enhances permanganate consumption by 30% from the base case, however this degree of increase is not reasonable given current literature estimates of k_{ox}^{slow} (Xu & Thomson, 2009). Variations in passivation (Section 2.2.3) produce no visual change in the permanganate PPT BTCs (Appendix

D). As discussed, in the base-case simulation passivation reduced the consumption of the slow fraction of OAM by < 10%. Since no visual change is apparent by reducing k_{ox}^{slow} to zero, no change can be expected due to variations in the passivation factor.

Variations in the quantity of OAM reveal that permanganate consumption increases by 50% for a 7 fold increase in OAM (50 g/kg) and decreases permanganate consumption by 81% for a 7 fold decrease in OAM (1 g/kg). The differences in permanganate mass consumed indicate that the quantity of OAM in the test zone plays a strong role in the resulting PPT BTCs. Changing the fast and slow OAM stoichiometric mass ratios (Figure 3-2(d) and (e)) did not yield a significant change in the mass of permanganate consumed (<10% due to variations in β_{fast} and < 1% due to variations in β_{slow}). The stoichiometric requirement for the consumption of OAM does not play a role in the PPT BTC in comparison to k_{ox}^{fast} or the quantity of OAM.

3.1.3 PPTs to Estimate Permanganate NOI Reaction Rate Coefficients

One interest in the use of PPTs to investigate NOI is to search for opportunities in the design of the test that results in the magnification of the controlling kinetic parameters (k_{ox}^{fast}, k_{ox}^{slow}, k_{OAM}^{fast}, k_{OAM}^{slow}). Field operational parameters include the injected permanganate concentration, the injection and extraction flow rates, and the duration of injection and reaction phases. As observed in Section 3.1.2, the influence of k_{ox}^{slow} (related to k_{OAM}^{slow}) on the BTC is minimal and as a result characteristics in the BTC attributed to k_{ox}^{slow} are unlikely. The quantity of OAM was observed to play a strong role in the shape of the permanganate BTC and can be estimated from a COD test. Permanganate PPT BTCs were therefore examined for characteristics that may be related to k_{ox}^{fast}.

Different combinations of field operating and NOI parameters can produce similar BTCs. For example, a BTC that indicates a significant portion of the permanganate mass injected has been consumed could be attributed to the duration of the reaction phase, the quantity of OAM or due to the magnitude of k_{ox}^{fast}. This potentially limits the ability to estimate reaction rate coefficients from field BTCs, especially if BTC tails are incomplete from sample collection, or the bounds of the parameters are unknown (Haggerty et al., 1998). The potential in analyzing BTCs for kinetic rate coefficients has been well established (Haggerty et al., 1998) and several regression methods

exist for estimating first-order reaction kinetics (Section 1.0) (Haggerty et al., 1998; Hall, Luttrell, & Cronin, 1991; Istok et al., 1997). A regression analysis is conducted with the base case permanganate PPT BTC to examine whether it can be applied in a limited fashion to this situation.

The simple analytical regression method presented by Schroth (2006) estimates first-order reaction rate coefficients based on a plug flow mixed reactor model. The method essentially involves manipulating the BTC data to produce a characteristic linear first-order relationship. Applying this graphical method to the base-case PPT BTC reveals, as expected, that permanganate PPT BTCs do not follow the characteristic profile for a first-order reaction (Figure 3-4(a)). However for simulations when k_{ox}^{fast} is decreased, the characteristic relationship becomes more linear, and if k_{ox}^{fast} is reduced to zero a pseudo first-order rate coefficient for the slow reacting permanganate rate coefficient (k_{ox}^{slow}) can be approximated from the regression technique (Table 3-2). An example of this is presented in Figure 3-4(b), where the regression analysis is conducted on a PPT BTC simulated using the base-case parameters, but with k_{ox}^{fast} set to zero. Scroth et. al. (2006) describes the slight variation (r^2~1) in Figure 3-4(b) as a result of the plug flow mixing assumption not fully representing the mixing of the injected test solution with the aquifer. The graphical analysis is able to estimate the second-order rate coefficient because k_{ox}^{slow} is so low that C_{OAM}^{slow} is essentially constant. While it is unlikely that this scenario would exist in the field, the regression technique provides insight into the link between the rate coefficients and the PPT BTCs.

The coupled second-order nature of the rate coefficients makes estimating k_{ox}^{fast} from graphical procedures problematic. Applying the characteristic kinetic second-order plot (Connors, 1990) to a PPT BTC requires estimating the fast and slow OAM concentrations. This approach is complicated because the exact amount of OAM oxidized by the fast and slow fractions are unknown based on the permanganate BTC. An estimate of k_{ox}^{fast} can be obtained from a permanganate PPT BTC dataset by employing the model to simulate the PPT with the literature estimates of the remaining NOI parameters (Table 3-4), a COD test to estimate the quantity of OAM, and the operational parameters. The literature estimates can be used since the majority of the NOI parameters do not manifest in the BTC. Calibration between the simulated and

observed BTCs ("curve fitting") can be undertaken to adjust k_{ox}^{fast} to fit the permanganate BTC. PPT-ISCO acts as a quick interpretation tool, and curve fitting is not significantly time consuming as each simulation typically requires much less than a minute.

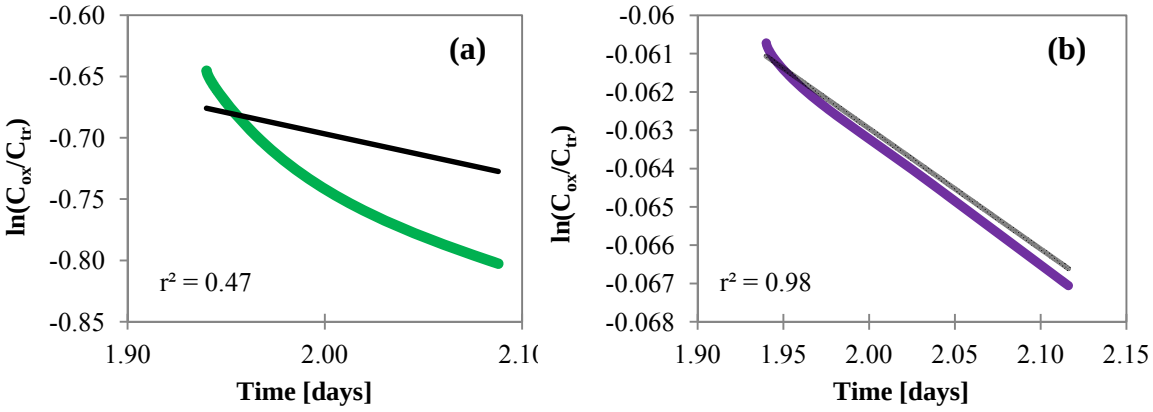

Figure 3-4. First-order characteristic kinetic plot for permanganate PPT BTCs with (a) k_{ox}^{fast} = 0.05 L/g/day and (b) k_{ox}^{fast} set to zero

Table 3-2. Estimates of rate coefficients (k_{ox}^{slow}) from BTCs when k_{ox}^{fast} is set to zero

Simulated k_{ox}^{slow} (L/g/day)	k_{ox}^{slow} (estimated) (L/g/day)	Error (%)
0.0058 (base case)	0.0057	1.7
0.0020	0.0019	5.0
0.0090	0.0087	3.3

Table 3-3. Information required to estimate k_{ox}^{fast} from permanganate PPT BTCs using PPT-ISCO

Parameter	Method to Obtain Parameter
Q_{inj}	field operating parameter
Q_{ext}	field operating parameter
t_{inj}	field operating parameter
t_{rxn}	field operating parameter
t_{ext}	field operating parameter
C_{MnO_4}	field operating parameter
C_{tracer}	field operating parameter
b	well screen interval
r_{well}	injection well radius
θ	conservative tracer fit
α_r	conservative tracer fit
OAM	COD test
k_{ox}^{fast}	permanganate BTC fit, approximated between 10^{-1} to 10^{-2} L/g-day from (Xu & Thomson, 2009)
k_{ox}^{slow}	Estimated as $\leq 10^{-3}$ L/g/day from (Xu & Thomson, 2009)
k_{MnO_2}	Estimated as $\leq 10^{-5}$ day^{-1} from (Xu & Thomson, 2009)
k_p	Estimated between 0 - 10 L/g/day from (Xu & Thomson, 2009)
$C_{OAM}^{fast} / C_{OAM}^{total}$	Estimated between 45-60% from (Xu & Thomson, 2009)
β^{fast}	Estimated as 6/21 from (Xu & Thomson, 2009)
β^{slow}	Estimated as 14/21 from (Xu & Thomson, 2009)

3.1.4 NOD Estimate

PPTs have been employed in the past as a tool to estimate the permanganate NOD (Mumford et al., 2004). The NOD estimate (assuming no drift) from a PPT is expressed as (Mumford et al., 2004):

$$\mathrm{NOD}_{\mathrm{PPT}} = \frac{\left(\frac{m_{inj}^{ox} - m_{ex}^{ox}}{f_{rec}^{Tr}} \right)}{m_{aq}^{i}} \quad \text{with} \quad \begin{array}{l} f_{rec}^{Tr} = m_{ex}^{Tr} / m_{inj}^{Tr} \\ m_{aq}^{i} = \rho_b V_{inj} / \theta \end{array} \tag{3-1}$$

where m_{inj}^{ox} (M) is the mass of $KMnO_4$ injected; m_{ex}^{ox} (M) is the mass of $KMnO_4$ extracted; f_{rec}^{Tr} (-) is the fractional tracer recovery (ratio of tracer mass extracted to tracer mass injected); m_{aq}^{i} (M) is the initial mass of aquifer solids contacted; ρ_b (M/L^3) is the dry bulk density of the aquifer material; V_{inj} (L^3) is the injected solution volume; and θ (-) is the effective porosity of the aquifer. All of these parameters (except porosity and density) are estimated from the mass of permanganate and tracer extracted during the pull phase of the PPT. The $\mathrm{NOD}_{\mathrm{PPT}}$ predicted by Equation (3-1) for the base-case permanganate PPT (Table 3-1) is 0.56 g/kg.

To examine the accuracy of the method presented by Equation (3-1), the base case permanganate BTC and spatial profiles were examined. Figure 3-5 shows the NOD profile across the test zone as determined at each computational node (control volume). Note that near the injection well the NOD > 0.85 g/kg. TO determine a system wide NOD, each control volume NOD is multiplied by a weighting factor (V_i /V_T) (where V_i (m^3) represents the volume of aquifer material in the current control and V_T (m^3) is the total volume of impacted aquifer material) and summed over the entire spatial domain. This summation of the OAM consumption ($\mathrm{NOD}_{\mathrm{cumultv.}}$) across the test zone is shown in Figure 3-6, where at the end of the test zone the $\mathrm{NOD}_{\mathrm{PPT}}$ is equal to 0.56 g/kg; identical to the value obtained from the BTC analysis.

The consumption of OAM, as described in Section 3.1.1, decreases with distance from the injection well (Figure 3-1). When the mass of OAM consumed in each control volume is expressed as an NOD (Figure 3-5), the majority (75%) of the control volumes impacted (by permanganate) express NOD values greater than 0.56 g/kg. Figure 3-6 also shows the mass of aquifer solids impacted by the injected permanganate, in relation to the $\mathrm{NOD}_{\mathrm{cumultv.}}$ across the test zone. Approximately 90% of the $\mathrm{NOD}_{\mathrm{PPT}}$ ($0.9\mathrm{NOD}_{\mathrm{PPT}}$ = 0.51 g/kg) manifests within the

first 60% of the initial mass of aquifer solids contacted ($0.60\,m_{aq}^{i}$). The remaining NOD beyond this point contributes to <10% of the NOD_{PPT} (0.05 g/kg) and implies that the NOD_{PPT} as estimated from the BTC represents an underestimate. As expected, the permanganate consumption is greatest in the vicinity of the well and decreased towards the edge of the test zone. As a result it may not be appropriate to include the entire mass as given by m_{aq}^{i} in the estimate of NOD_{PPT}. If V_T is adjusted so that the total volume of aquifer impacted is decreased to reflect the location where 90% of the NOD_{PPT} is expressed, the predicted NOD_{PPT} value (represented as NOD_{90} in Figure 3-6) increases by approximately 30% (0.80 from 0.56 g/kg). With the radial system, the large quantity of aquifer mass ($0.40\,m_{aq}^{i}$) that contributes < 10% of NOD_{PPT} drives the system-wide NOD down (to 0.56 g/kg) when compared to the control volume NOD values near the injection well (> 0.85 g/kg).

Hence it is reasonable to omit from Equation (3-1) the mass of aquifer solids that contributes to < 10% of NOD_{PPT}. Equation (3-1) can be used twice to obtain intervals of the NOD_{PPT} using the original estimate of m_{aq}^{i} (described in Equation (3-1)), and the estimate of m_{aq}^{i} that accounts for 90% of the NOD_{PPT}. The intervals obtained will encompass a more representative NOD of the site. The intervals obtained for the base case permanganate PPT are 0.87 g/kg < NOD < 0.56 g/kg. The following guidelines can be used to obtain intervals of the NOD for a permanganate PPT BTC:

1. Calculate NOD_{PPT} using Equation 3-1 (0.56 g/kg)
2. Reduce estimate of NOD_{PPT} by 10% (0.51g/kg)
3. Apply PPT-ISCO to illustrate the NOD_{PPT} profile and mass of aquifer solids impacted (Figure 3-6)
4. Obtain the second estimate of m_{aq}^{i} (the mass that corresponds to the NOD_{PPT} at 0.51g/kg, 145 kg)
5. Use Equation (3-1) again using the reduced estimate of m_{aq}^{i} and obtain the second interval of NOD_{PPT} (0.87 g/kg)

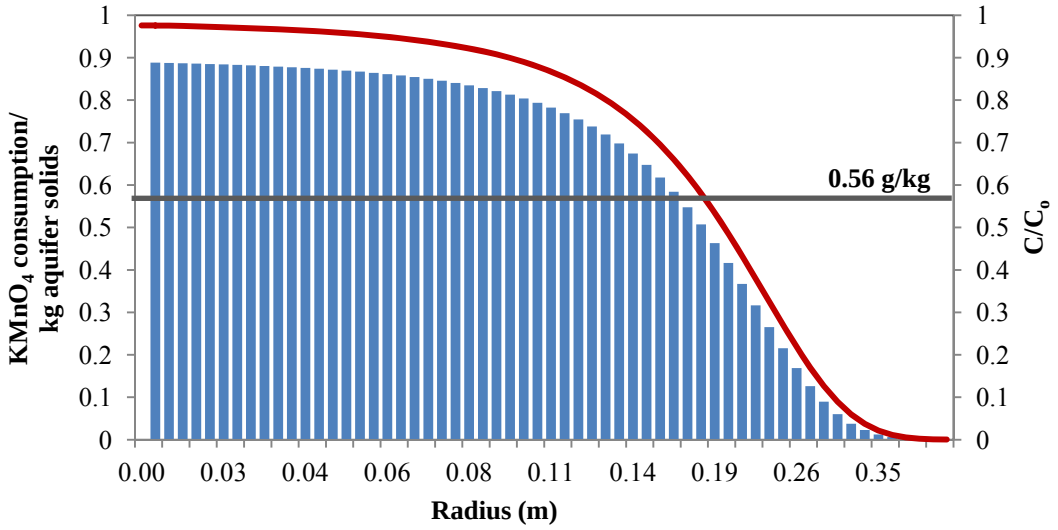

Figure 3-5. OAM consumption expressed as NOD for each control volume. Each bar represents a control volume. Note the x-axis represents the location of the control volume across the spatial domain. The tracer curve is presented on the right-hand axis (extent of injection).

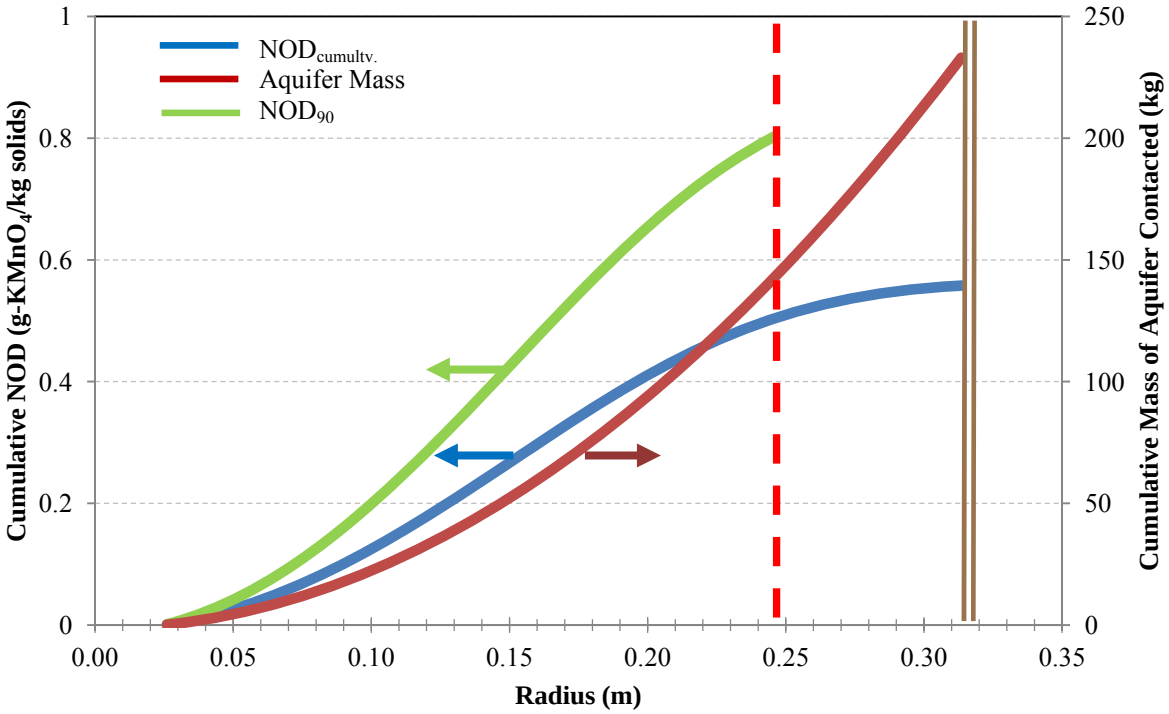

Figure 3-6. Cumulative NOD Profile (base case scenario). Dashed line indicates location where 90% of the NOD_{PPT} is reached. Solid double line indicates extent of permanganate injection (m_{aq}^{i}) based on Equation (3-1).

3.2 Persulfate

Persulfate PPT investigations were conducted to illustrate the effects of the controlling PPT parameters (Table 3-4) on the persulfate PPT BTCs. The concentration of amorphous iron and TOC are 0.24 and 0.30 mg/g, respectively, as estimated by Sra et. al., for the CFB Borden aquifer. The empirical constant k_{cat} and k_{NOM} (Equation 2-10(b)) are estimated as 79.6×10^{-3} day^{-1} and 32.4×10^{-3} day^{-1}, respectively (Sra et al., 2010).

Table 3-4. Investigated Persulfate PPT Parameters

Parameter	Notation	Unit	Range
injected $Na_2S_2O_8$ concentration	$C_{ox}^{initial}$	g/L	1,5,*20*[1]
injection phase duration	t_{inj}	-	20 minutes, *4 hours*[1], 1.5 days
reaction phase duration	t_{rxn}	-	*1 day*[1], 10 days, 20 days
injection flow rate	Q_{inj}	m^3/day	0.5, *1.0*[1], 5
extraction flow rate	Q_{ext}	m^3/day	0.5, *1.0*[1], 5
NOI reaction rate coefficient	k_{obs}	day^{-1}	0.10, *0.21*[1], 0.70

1. base case values

3.2.1 Spatial Profiles

Spatial profiles illustrating the distribution of persulfate are presented for the base case, and for cases of increasing reaction times (Figure 3-7). The tracer profile is included to observe the radial extent of the persulfate injection. The decomposition of persulfate is represented as sulphate. Figure 3-8 presents the ionic strength across the test zone for increasing reaction phases.

The spatial profiles collectively illustrate the spread and change in persulfate concentration, the sulphate production in response to persulfate degradation, and the relationship of both to the ionic strength. The ionic strength is primarily controlled by the injected persulfate concentration, and as persulfate degrades into sulphate (SO_4^{2-}) and acid (H^+), the ionic strength will be enhanced (Sra et al., 2010). The highest ionic strength is located in the vicinity of the well, where the persulfate concentration is greatest, and decreases across the reaction site proportionally with the persulfate concentration (Figure 3-7 and Figure 3-8). The degradation of persulfate due to

the NOI is partially controlled by the activity coefficients of persulfate and the reactant. As the ionic strength is enhanced over time, the activity coefficients decrease and the rate of persulfate degradation (k_{bulk}) due to the NOI is decreased. The overall rate of persulfate degradation can be summarized as (from Equation 2-10)

$$k_{bulk}(t) = k_{obs}\gamma_{S_2O_8}\gamma_{react}^{1.5} \qquad (3\text{-}2)$$

At the end of the push phase very little degradation of persulfate has occurred, and the sulphate concentration is increased at further distances from the well (Figure 3-7(a)). This is a result of a higher degradation rate at distal zones (due to the lower ionic strength) at early times compared to zones close to the injection point. For example, between 0.04 m and 0.40 m away from the well, k_{bulk} is increased approximately 7 times (from 0.006 to 0.04 day^{-1}).

Over time the ionic strength will increase as persulfate degrades (Figure 3-8), and this will result in the continual suppression of k_{bulk} everywhere. The reduction in k_{bulk} (at 0.40 m from the injection well) is approximately 50% from the end of the push phase to the end of the 10 day reaction phase (0.04 to 0.02 day^{-1}). As the ionic strength is enhanced with time, this percentage can be expected to increase.

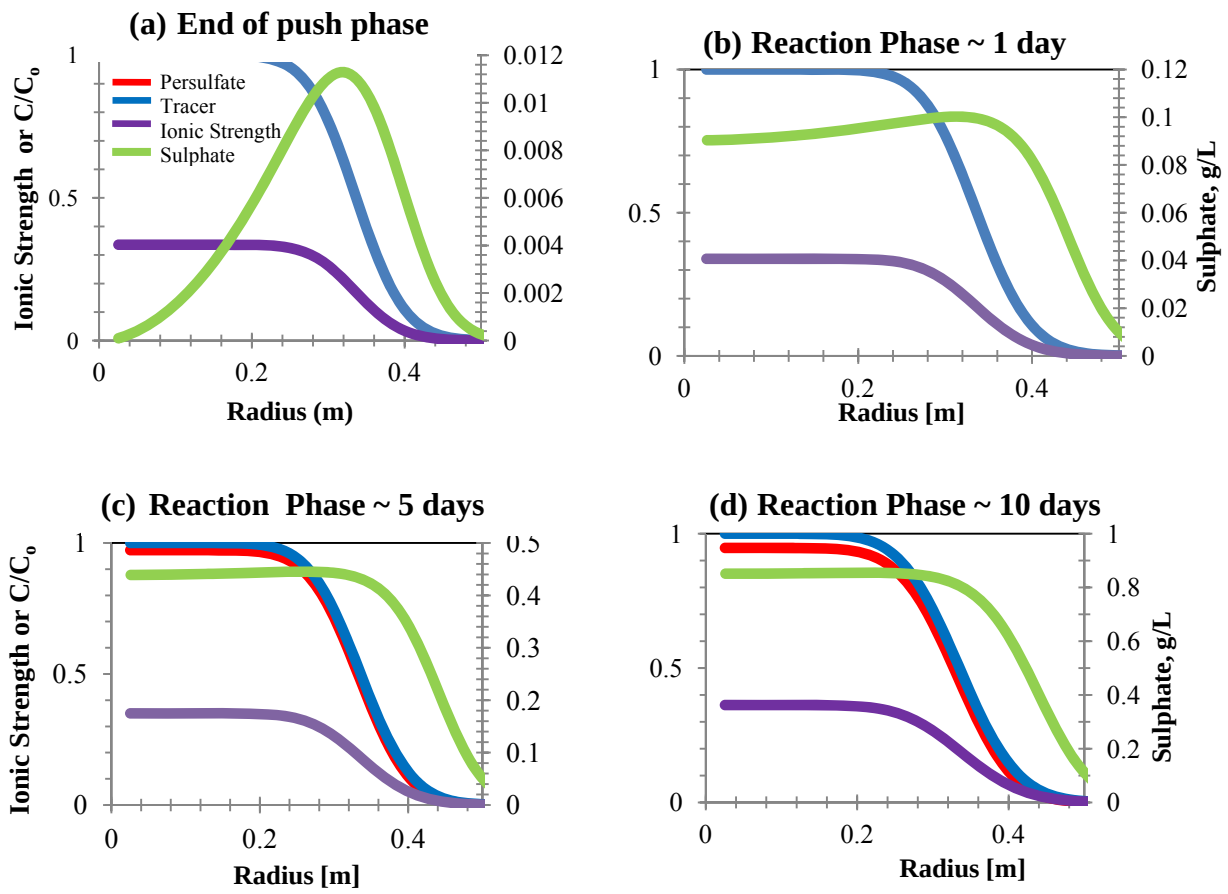

Figure 3-7. Spatial profiles of persulfate (normalized), tracer (normalized), sulphate (g/L) and ionic strength (unitless) at (a) the end of the push phase, and (b), (c), (d) after a reaction phase of 1.0 day, 5.0 days and 10.0 days respectively. The sulphate concentration is presented on the right-hand axis.

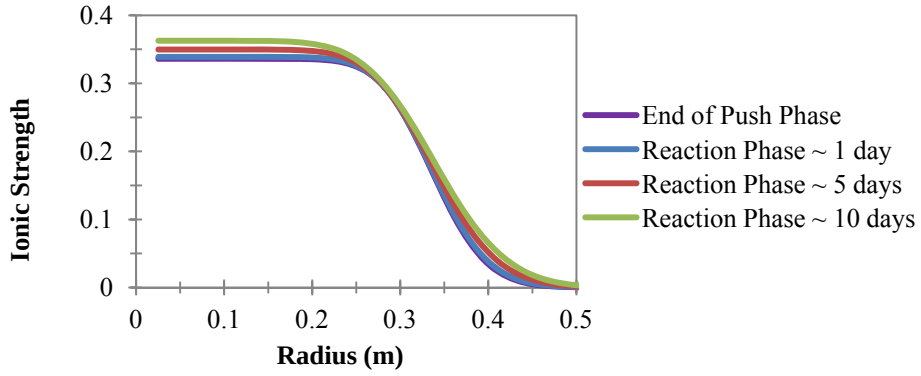

Figure 3-8. Spatial profile of ionic strength with varying reaction times

3.2.2 Sensitivity Analysis

The sensitivity of persulfate PPT BTCs to variations in the field operational parameters and k_{obs} is examined with Figure 3-9.

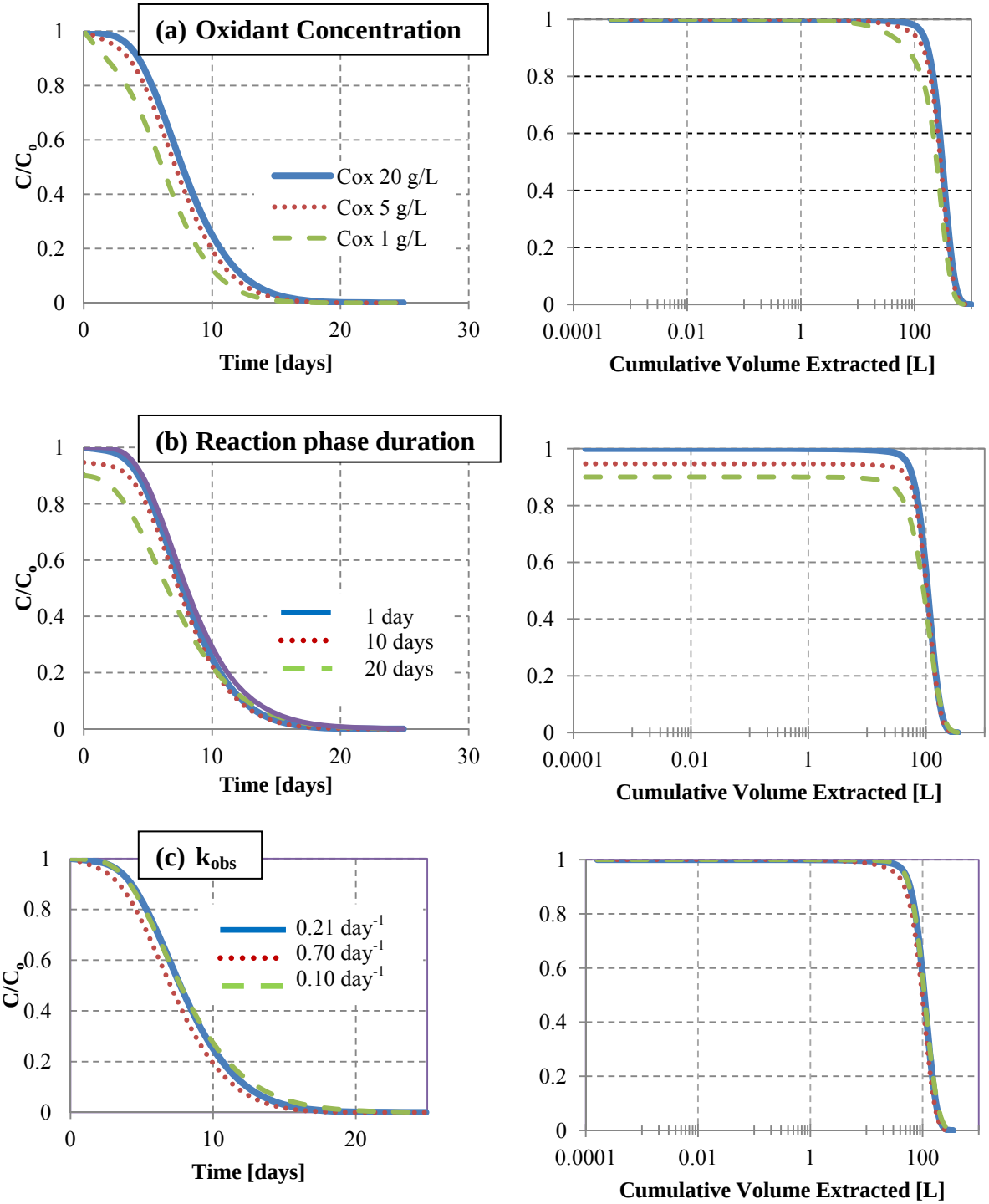

Figure 3-9. BTCs during the extraction phase of a PPT for various operating parameters and k_{obs}. The base case is shown in blue.

Persulfate BTCs can be characterized by a concentration plateau observed at early times (Figure 3-9(a) – base case). This observed plateau is a result of the minimal persulfate degradation that takes place near the well, as a result of the elevated ionic strength. As described above, in zones of high ionic strength, the activity coefficients of persulfate and the reactants are suppressed, and the overall degradation rate of persulfate is decreased. The concentration plateau is diminished when the injected persulfate concentration is decreased (Figure 3-9(a)). As the injected concentration is reduced, the ionic strength in the vicinity of the well is decreased, enhancing the rate of persulfate degradation (k_{bulk}). For example with the injection concentration reduced to 1 g/L, the initial k_{bulk} around the well is increased approximately 10 times (compared to the base case). The plateau has essentially disappeared for an injection concentration of 1 g/L, highlighting this faster degradation rate at early times.

As expected, increases in the reaction phase duration and the reaction rate k_{obs} (Figure 3-9(b) and (c)) increase the mass of persulfate degraded. The concentration plateau continues to be observed because the ionic strength (as prescribed by the injected persulfate concentration) is not varied. The scalability of the field operating parameters remains consistent with the findings presented for the permanganate field operating parameters (presented in Appendix D -).

3.2.3 PPTs to Estimate Persulfate NOI Rate Coefficients

Persulfate PPT BTCs were also investigated for opportunities to highlight the controlling kinetic parameters. Persulfate degradation follows an enhanced first-order degradation rate (k_{bulk}) that varies in time. As a result it is more practical to investigate methods that estimate k_{obs} from the PPT BTCs. The kinetic parameters required for k_{obs} (k_{cat} and k_{NOM}) are available from Sra et. al. (2010), empirically derived from seven well-characterized aquifer materials. The concentrations of amorphous iron (C_{cat}) and TOC (C_{NOM}) can be estimated using laboratory techniques on aquifer samples obtained in the field. However, for PPTs conducted in aquifer material not captured by Sra et. al., (2010) the empirical constants will not be valid.

Equation (3-2) represents an enhanced first-order rate expression because k_{bulk} is multiplied by the activity coefficients of persulfate and the reactant. The graphical regression analysis (Section 3.1.3) is applied in conjunction with the initial persulfate and reactant activity values (as estimated from the injected persulfate concentration) to approximate k_{obs}. Fitting the persulfate PPT BTC (base case scenario) to the characteristic kinetic plot for a first-order reaction reveals

as expected, a linear trend (Figure 3-10). The slope of the characteristic plot estimates a first-order kinetic rate, which for persulfate PPT BTCs is represented by k_{bulk}. An estimate of k_{obs} is obtained by dividing the reaction rate estimated from the slope by the initial activity coefficients of persulfate and the reactant as described in Equation (3-2). With this, the graphical method underestimates the simulated base case k_{obs} by approximately 14% (0.19 from 0.22). This is because as persulfate degrades and the ionic strength is increased, the activity coefficients decrease in time. The decreasing activity coefficients cause the graphical method to consistently produce an underestimated value of k_{obs} (Table 3-5).

An accurate estimate of k_{obs} can be achieved through the use of PPT-ISCO and the graphical procedure together. The graphical method provides a starting value that can be used during curve fitting to estimate k_{obs}. Using this starting value, and the field operational parameters, a simple curve fitting exercise can be undertaken to estimate of k_{obs} (Table 3-6).

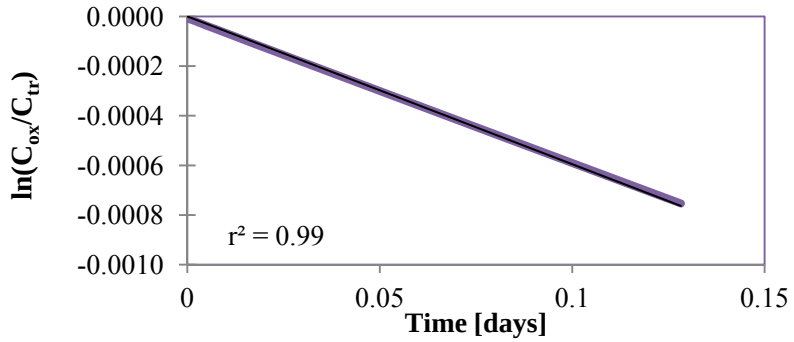

Figure 3-10. Base Case PPT BTC plotted to characteristic kinetic plot for first-order reaction

Table 3-5. Estimates of rate coefficients (k_{obs}) from persulfate BTC

Simulated k_{obs}	k_{obs} (estimated)	Error (%)
0.22 (base case)	0.19	13.6
0.40	0.35	12.5
0.10	0.09	10.0

Table 3-6. Information required to estimate k_{obs} from persulfate PPT BTCs using PPT-ISCO

Parameter	Method to Obtain Parameter
Q_{inj}	field operating parameter
Q_{ext}	field operating parameter
t_{inj}	field operating parameter
t_{rxn}	field operating parameter
t_{ext}	field operating parameter
$C_{S_2O_8}$	field operating parameter
C_{tracer}	field operating parameter
θ	conservative tracer fit
α_r	conservative tracer fit
k_{obs}	1) Starting value estimated from graphical method 2) Accurate estimate from adjustment of starting value to persulfate BTC fit
$\gamma_{S_2O_8}, \gamma_{react}$	Extended Debye-Hückel approximation and $C_{S_2O_8}$ (Section 3.2.1)

4 ISCO Treatability using PPTs

PPTs investigating ISCO treatability (treatability PPTs) have the ability to provide insight into the effect of the NOI on the oxidation of target COCs, site-specific oxidant dosage requirements and NAPL treatment expectations. The effect of the NOI on ISCO treatability has been reported in pilot scale studies where removal of significant amounts of NAPL mass in a porous medium environment required the injection of permanganate in excess of the amount predicted by the stoichiometric relationship between permanganate and the target COC (Schnarr et al., 1998; Thomson et al., 2007). The site-specific oxidant dosage can be defined as the total mass of oxidant consumed (by the NAPL and the NOI) per mass of the NAPL oxidized. If dosage estimates are able to be approximated from PPT BTCs, then potential exists to apply PPTs as a preliminary *in situ* screening tool for ISCO.

In this chapter the various features of a treatability PPT are studied by first examining NAPL dissolution and oxidation kinetic behaviour (Section 2.2.1 and 2.2.2) experienced during a PPT. This is completed by investigating the sensitivity of the governing dissolution and oxidation parameters to PPT NAPL component BTCs. Variations in the oxidation and dissolution parameters are manifested in the PPT BTCs as the time required for each of the NAPL components to return to a relative concentration of unity. The ability to extract estimates of oxidant dosage and treatability expectations from the BTCs is explored. The behaviour of each oxidant during a PPT into a gasoline-component contaminated aquifer is examined for the effects of the NOI and treatability characteristics specific to each.

4.1 Methodology

The numerical investigations explored here occur in a hypothetical aquifer system ('test zone') that is characterized (Table 4-1) as homogeneous with respect to porosity ($\theta = 0.3$) and sediment density ($\rho = 1.81$kg/L). The screened interval ($b = 1.5$m) of the injection well ($r_{well} = 0.025$m) is situated within the saturated zone of the aquifer.

The NAPL residuals are comprised of either residual MGP or gasoline contamination. Reaction rate coefficients, stoichiometric mass requirements, weight percentages and reference fugacities for the MGP and gasoline residual components are presented in Appendix A. MGP residual tars are mixtures of thousands of chemicals consisting primarily of hydrocarbons with lesser quantities of other organic and inorganic compounds. It is impossible to determine the precise

chemical composition of MGP residuals because they are dependent on the specific MGP processes that were employed during use (Lehr, Hyman, & Gass, 2001). The investigated MGP residual composition consists of 20 dissolved species and a bulk component. MGP residual contamination treatability is investigated with permanganate only, reaction rate coefficients between persulfate and the dissolved MGP residual species is not well established. Of the 21 MGP residual components investigated, 13 are oxidizable by permanganate. The MGP residual analyses presented here focus on 5 representative components: benzene, naphthalene, 2-methltnaphthalene (2-methltnap), 1-methltnaphthalene (1-methltnap) and acenaphthylene. Of the non-oxidizable compounds, benzene and acenaphthylene were selected due to their high and low maximum solubility concentrations, respectively. Naphthalene, 2-methltnap, 1-methltnap were selected to represent the oxidizable components due to their relatively high reaction rate coefficients with permanganate, and significant weight percentage in MGP residuals.

Gasoline is composed of a mixture of volatile hydrocarbons suitable for use in internal combustion engines. The primary components of gasoline are branched-chain paraffins, cycloparaffins, and aromatics. The residual gasoline contamination investigated is comprised of 9 components: benzene, toluene, ethylbenzene, o-xylene, m,p-xylene, 1,2,3-trimethylbenzene, 1,2,4-trimethylbenzene, 1,3,5- trimethylbenzene and naphthalene. The remainder of the gasoline is assumed to be non-reacting and grouped into the bulk component. The entire suite of gasoline components, except the bulk fraction, is oxidizable by persulfate. All except the bulk fraction and benzene are oxidizable by permanganate. The representative components were selected as benzene, naphthalene, m,p-xylene, and 1,2,3-trimethylbenzene. The non-oxidizable component is represented by benzene (for MGP residual investigations) and the remaining to be illustrative of the oxidizable components. Two gasoline compositions with different component weight percentages are examined (Figure 4-1). The first, gasoline Composition A, is for the case where the weight percentages of the 9 components analyzed are taken from a baseline gasoline analysis completed by the Chevron Corporation (Appendix B). The remaining percentage is assigned to the bulk component. For the second, gasoline Composition B, the bulk component weight was taken as the percentage remaining after summing the total percentage of components present in gasoline (branched alkanes, alkyl benzenes, strait chain, branched alkene, straight alkene, cycloalkane, cycloalkene and PAHs). The weight percentages for the 9 gasoline components (as taken from composition A) and the bulk were then scaled to unity.

Simulations are performed for a "base case" and for additional cases (in the sensitivity analysis) where a single parameter is varied from the base case. The residual NAPL (ρ_{NAPL} = 1.1 kg/L) contamination (S_{NAPL} = 1%) is modelled assuming two discrete mass transfer limited regions. The aqueous concentration of the NAPL components in the groundwater is uniform across the domain and initially set at their respective effective solubility limits.

Base case values for $t_{inj,}$ t_{rxn}, t_{ext}, Q_{inj}, and Q_{ext} (Table 4-1) were selected to be representative of values used in PPT experiments (Haggerty et al., 1998; Mumford et al., 2004; M. H. Schroth & Istok, 2006; Sra et al., 2010). The oxidant is injected at a rate of 1 m^3/day for 6 hours and after the duration of the reaction phase withdrawn continuously (4.5 m^3/day) over a period of 10 days. $C_{ox}^{initial}$ is set to 20 g/L to represent the maximum concentration that may be used in the field while avoiding significant density effects. Permanganate (Table 2-2) and persulfate (Table 2-3) NOI kinetic data were characterized based on the CFB Borden aquifer.

The simulations were completed using the exponential spatial weighting scheme, centered-in-time temporal scheme. Control volume and time step sizes were increased by a factor of 5% (α) and 0.005% (β) respectively. The initial Δt was set at 1 second. The results of these investigations are presented as PPT BTCs and NAPL mass profiles that feature the representative components of MGP or gasoline residual at a location within close vicinity to the injection well (0.04 m) or at a distal location in the spatial domain (0.4 m).

Table 4-1. Parameters Used in Treatability Simulations

Parameters	Value
b (m)	1.5
r_{well} (m)	0.025
θ (-)	0.3
α_r (m)	0.01
ρ_b (kg/L)	1.81
S_{NAPL} (%)	1
ρ_{NAPL} (kg/L)	1.1
$C_{ox}^{initial}$	20
t_{inj} (days)	0.25
t_{ext} (days)	10
Q_{inj} (m^3/day)	1
Q_{ext} (m^3/day)	4.5
n_{CV}	80

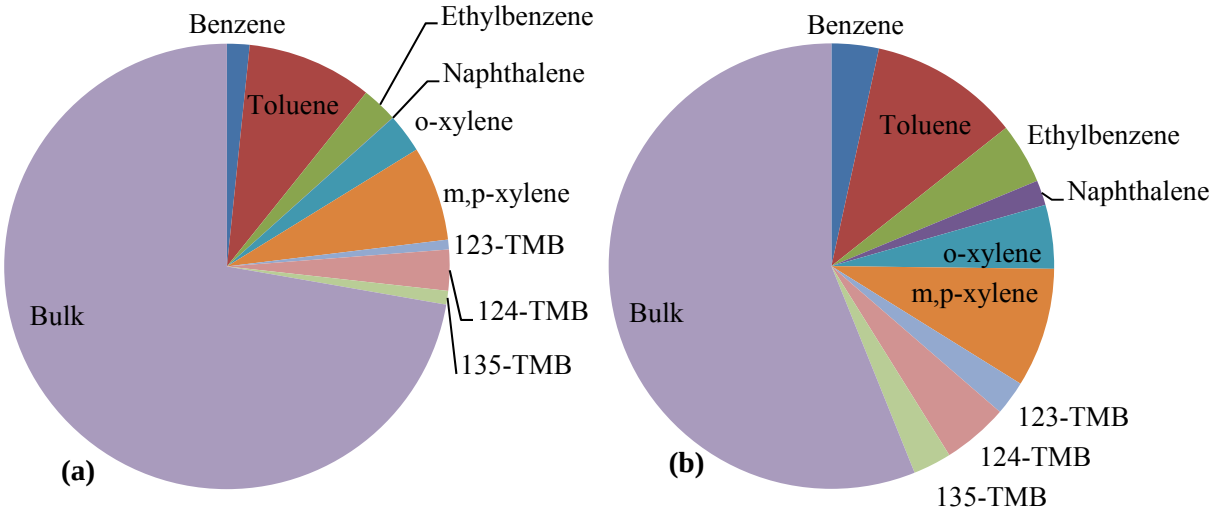

Figure 4-1. Component weight percentages for (a) gasoline Composition A and (b) gasoline Composition B

4.2 Sensitivity Analysis

The sensitivity analysis examines changes to NAPL component BTCs due to variations in the parameters that control the oxidation and dissolution kinetics (t_{rxn}, λ^{fast}, λ^{slow}, $m_{fast}^{NAPL}/m_{total}^{NAPL}$) and due to the effect of the NOI. The range of parameters investigated, and the base case values are presented in Table 4-2. To examine the sensitivity, a permanganate PPT ($C_{ox}^{init} = 20$ g-$KMnO_4$/L) was simulated into an aquifer contaminated with MGP residual tar (Table 4-1). The fast mass transfer rate coefficient is estimated as 10^3 day^{-1}, and is varied from 10^5 (representing ideal mass transfer conditions) and 10^2 day^{-1}. The lower two rate coefficients were selected to illustrate the variations in BTCs when the fast mass transfer rate coefficients are less than ideal. The slow mass transfer rate coefficient is set as 0.01 day^{-1} as estimated from Borden and Kao (1992) for toluene, xylenes and various aliphatic hydrocarbons, and is varied from 10^2 to 0.0001 day^{-1}. This range was selected to illustrate changes in the BTCs as a result of a much slower and much faster slow region mass transfer rate coefficient compared to the literature estimate. The percentage of NAPL mass in the fast region ($m_{fast}^{NAPL}/m_{total}^{NAPL}$) is estimated as 75% and is varied from 95% to 25%, to be representative of significant mass in either region. Variations in the permanganate NOI are represented through variations in k_{ox}^{fast}. The permanganate NOI is neglected for the sensitivity investigations, except for the cases examining the effect of the NOI. The remaining permanganate NOI parameters remain consistent with the literature values for the CFB Borden aquifer (Table 2-2).

Table 4-2. Range of Investigated Parameters

Parameter	Notation	Unit	Range
fast region mass transfer rate coefficient	λ^{fast}	day^{-1}	10^3[1],10^5,10^2
slow region mass transfer rate coefficient	λ^{slow}	day^{-1}	0.01[1], 100,0.0001
% of total NAPL in fast region	$m_{fast}^{NAPL}/m_{total}^{NAPL}$	%	75[1], 95, 55, 25
reaction phase duration	t_{rxn}	days	0.5[1], 3.5,10
permanganate fast reaction rate	k_{ox}^{fast}	L/g-day	0[1],0.15,0.015

1. base case value

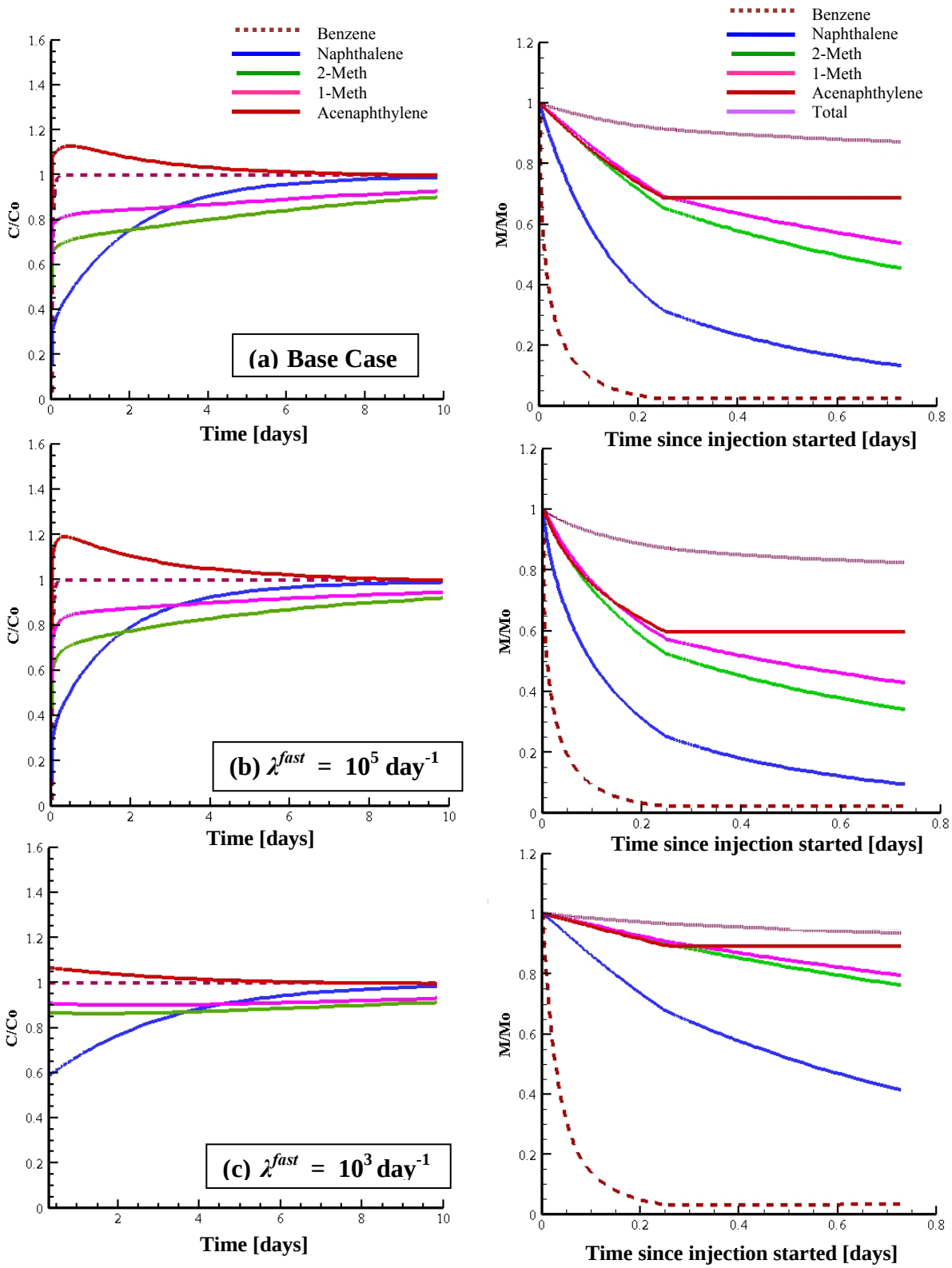

Figure 4-2. NAPL PPT results for (a) base case, and (b) and (c) variations in λ^{fast}. Left-hand panels represent PPT BTCs and right-hand panels represent the fast region NAPL mass profile located 0.04 m from the well

Variations in λ manifest in the amount of permanganate consumed, as well as the time for the components to return to a relative concentration of unity. Increasing λ^{fast} by two orders-of-magnitude causes the total mass of MGP residual dissolved from the fast and slow regions to increase by 70% from the base case, allowing permanganate mass consumption to increase an additional 12%. Similarly, an order-of-magnitude decrease in λ^{fast} causes the total mass of MGP residual dissolved from the fast and slow regions to decrease by 55% compared to the base case, which causes permanganate mass consumption to fall 27%. The increase in λ^{fast} causes dissolution in the fast mass transfer region to occur at a higher rate, resulting in a higher aqueous concentration of the MGP residual components in the groundwater. This increased groundwater concentration results in more oxidation, and thus an increase in permanganate consumption. The larger λ^{fast} manifests in the BTCs as the oxidizable components returning to a relative concentration earlier. Variations in λ^{slow} manifest in the same way as λ^{fast}, but to a smaller degree (Appendix E). The increase in λ^{slow} results in a 4% increase in permanganate consumption, and the decrease causes a negligible change in the mass of permanganate consumption.

In the NAPL mass profiles a distinguishable change in slope is clear at the time of transition from the injection phase to the reaction phase. The effect of increased MGP residual dissolution is noticed for the oxidizable components in the NAPL mass profiles between mass transfer rates. For example, 85% of the naphthalene mass in the fast region is dissolved at the end of the reaction phase in the base case, this percentage changes to 87% and 59% for the increase and decrease in λ^{fast} respectively. No major change is seen in the mass of benzene dissolved between the mass transfer rate coefficients, as the highly soluble nature of the compound causes a significant portion of mass to be dissolved (even at the lowest mass transfer rate).

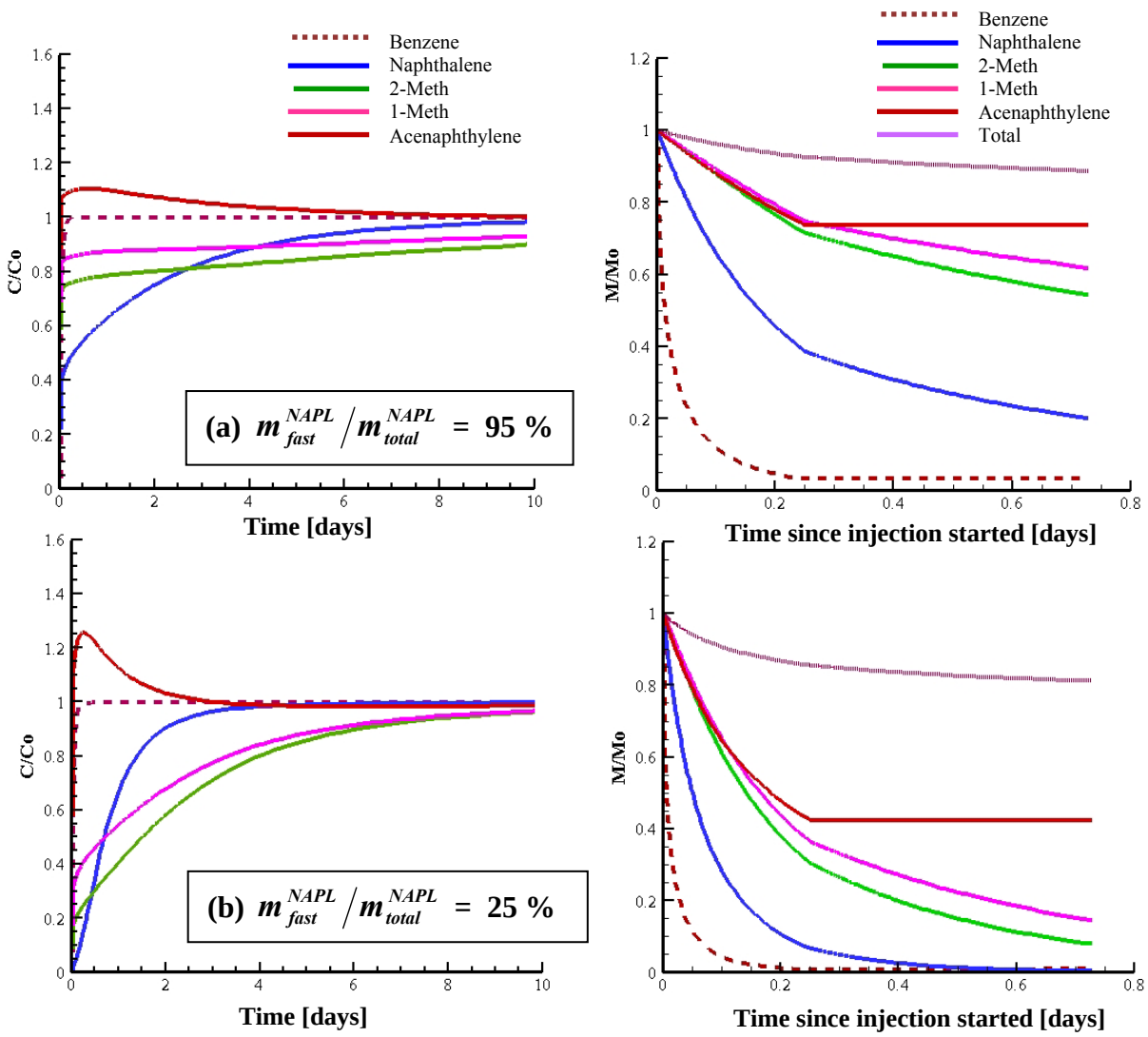

Figure 4-3. NAPL PPT results for variations in $m_{fast}^{NAPL} / m_{total}^{NAPL}$: left-hand panels represent PPT BTCs and right-hand panels represent the fast region NAPL mass profile located 0.04 m from the well

Similar to λ^{fast}, variations in $m_{fast}^{NAPL} / m_{total}^{NAPL}$ alter the mass of permanganate consumed by the MGP residuals. Increasing the percentage of mass in the fast region to 95% produces a 3% increase in permanganate consumption (compared to the base case), and decreasing $m_{fast}^{NAPL} / m_{total}^{NAPL}$ to 25% causes permanganate consumption to decrease 25%. With a lesser quantity of mass in the fast region, less mass is available to be dissolved by λ^{fast}. The decrease in dissolution reduces oxidation and as a result the permanganate consumption is decreased. The variations in λ and

$m_{fast}^{NAPL} / m_{total}^{NAPL}$ indicate that the BTCs are primarily governed by the dissolution and oxidation occurring in the fast region, as expected.

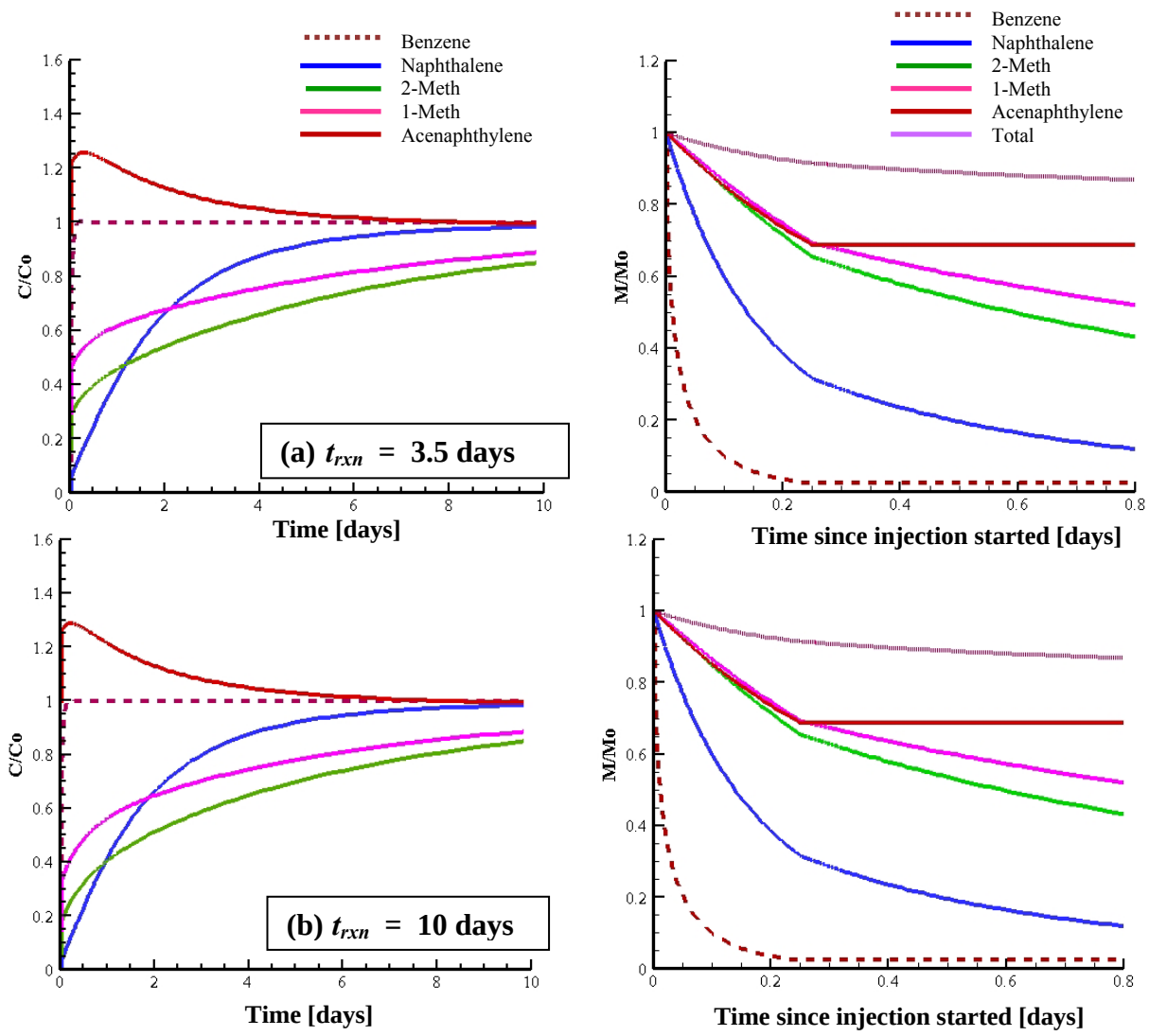

Figure 4-4. NAPL PPT results for variations in t_{rxn}: left-hand panels represent PPT BTCs and right-hand panels represent the fast region NAPL mass profile located 0.04 m from the well

Comparable to the permanganate and persulfate NOI investigations, the duration of the reaction phase has the greatest effect on the amount of permanganate consumed (Figure 4-4). Increasing the reaction phase duration from 0.5 days to 3.5 and 10 days causes permanganate consumption to be increased from 62% to 96% and 100% respectively. With the duration of the reaction phase increased, oxidant consumption is enhanced and dissolution increases proportionally to re-establish equilibrium. The increase in permanganate consumed between 3.5 days and 10 days is

not proportional since the oxidation rate will decrease as the oxidant concentration decreases. Furthermore, because the oxidant is fully depleted prior to the end of t_{rxn} = 10 days, an oxidant limited situation is created which restricts the information obtained from the NAPL component BTC analysis.

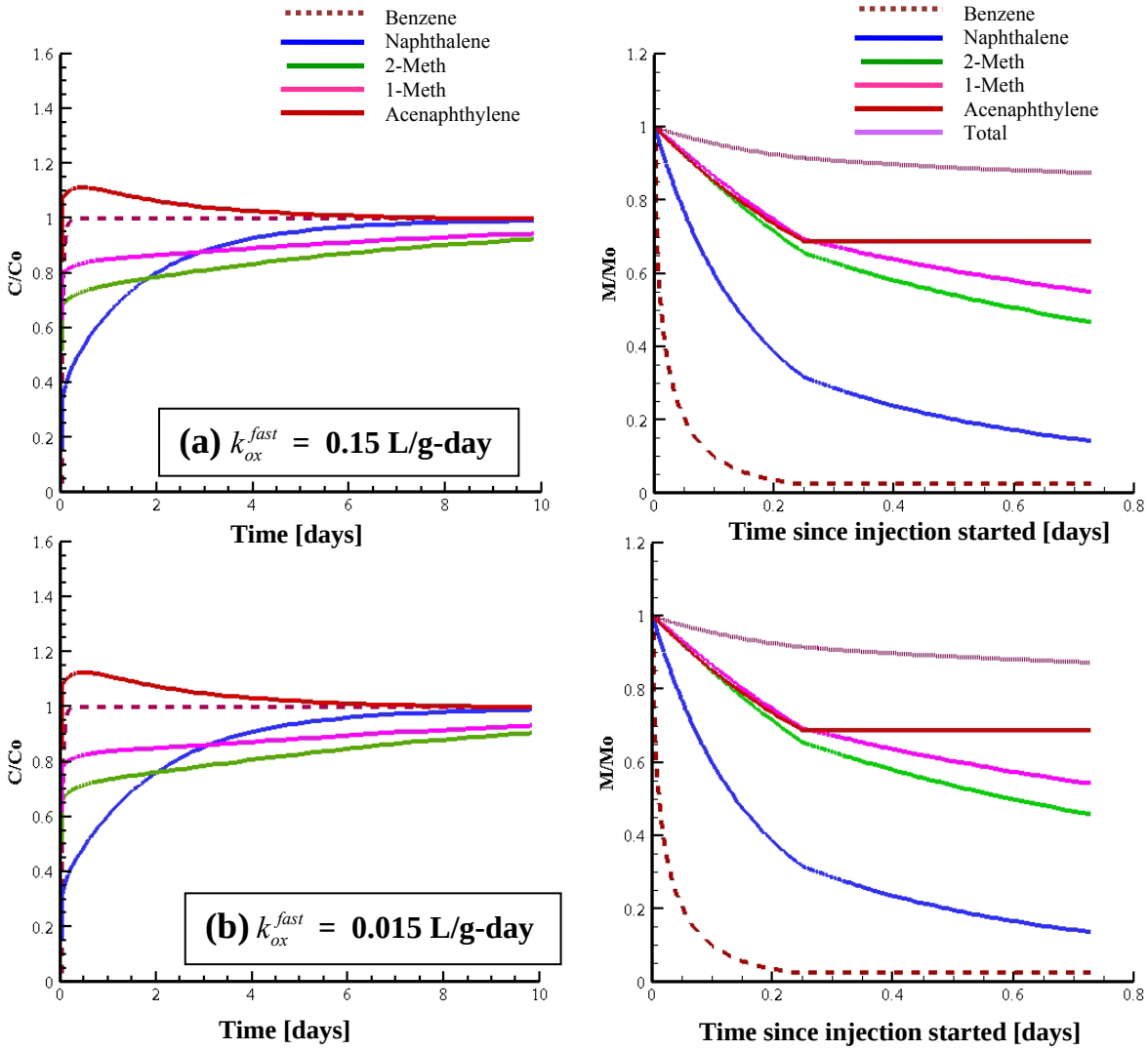

Figure 4-5. NAPL PPT results for variations in k_{ox}^{fast} : left-hand panels represent PPT BTCs and right-hand panels represent the fast region NAPL mass profile located 0.04 m from the well

The effect of the NOI reveals, as expected, the amount of permanganate available for oxidation of MGP residuals is decreased. Variations in k_{ox}^{fast} (0.015 and 0.15 L/g-day) cause the consumption of permanganate by MGP residuals to be decreased by 3 and 17% (from the base case where the NOI is neglected) respectively. Oxidation of MGP residuals by permanganate in

the presence of the NOI causes the permanganate concentration available for MGP residual oxidation to be decreased, lowering the rate of oxidation and thus lowering the mass of the MGP residuals required to be dissolved to re-establish equilibrium.

4.3 Oxidation Dosage and Treatability Estimates

PPTs have exhibited promise as a remediation screening tool by capturing *in situ* NOI behaviour. If the NOI has been parameterized, then the potential to obtain site-specific oxidant dosage and treatability estimates from NAPL component BTCs can be examined. Dosage estimates obtained from these BTCs should exceed what is prescribed by stoichiometry because a portion of the permanganate consumed will be a result of the NOI. Treatability expectations can be quantified as the mass of NAPL oxidized per total mass of oxidant consumed. These estimates can be obtained for any number of NAPL components monitored. A potential field technique to estimate oxidant dosage and treatability expectations is investigated.

It is theorized that oxidant dosage and treatability expectations can be estimated from the results of two PPT NAPL component BTCs (Figure 4-6). The first PPT (PPT-1) is conducted in the absence of an oxidant (only conservative tracer) (Figure 4-6(a)). The extraction phase of this PPT is continued until the relative concentrations of each of the NAPL compounds monitored have reached quasi-steady state (the extracted concentration does not vary with time), represented as t'. This first BTC provides baseline information regarding the behaviour and dissolution kinetics of the NAPL components in response to an inert injection into the system. This information is manifested as the time required for the relative concentration of the NAPL components to reach steady state.

The second PPT (PPT-2) (Figure 4-6(b)) is conducted under identical operating parameters as the first PPT, this time with the addition of an oxidant. The extraction phase is again continued until the relative concentrations of the monitored NAPL compounds have reached steady state (represented as t_1). The oxidant causes an increase in the NAPL dissolution required for the components to reach steady state. This time interval is governed by the fast region mass transfer rate coefficient and the mass of NAPL in the fast region. The combination of these two PPT NAPL BTCs provides the basis of the treatability assessment.

The difference in mass extracted between the NAPL component BTCs (m_i^{PPT}) represents the mass of the component destroyed by the oxidant (Figure 4-6(c)), and is given by

$$m_i^{PPT} = \int_{t_0}^{t_1} \left(Q_{ext} C_i^{PPT\text{-}1} dt \right) - \int_{t_0}^{t_1} \left(Q_{ext} C_i^{PPT\text{-}2} dt \right) \qquad (4\text{-}1)$$

where m_i^{PPT} (M) represents the mass of the monitored NAPL species *i* oxidized, C_i^{PPT-1} (M/L^3) represents the concentration of species *i* during the first PPT; C_i^{PPT-2} (M/L^3) represents the concentration of species *i* during the second PPT; t_0 represents the time at the start of the extraction, and t_1 represents the time at which the relative concentration of species *i* has reached steady state during the second PPT. The assumption that m_i^{PPT} represents the mass of species *i* oxidized requires the NAPL architecture to remain unchanged between PPTs. Since the first PPT requires a negligible quantity of mass to be removed for baseline information, the assumption is considered valid.

The treatability of each of the components can be expressed as

$$\frac{m_i^{PPT}}{\Delta \mathrm{MnO_4}} \qquad (4\text{-}2)$$

where ΔMnO_4 (M) represents the permanganate consumed (by the NAPL and the NOI) during the second PPT. Accounting for each of the oxidizable NAPL species monitored, the site-specific oxidant dosage can be estimated as

$$dosage = \frac{\Delta \mathrm{MnO_4}}{\sum_{i=1}^{nc} m_i^{PPT}} \qquad (4\text{-}3)$$

where *nc* represents the total number of oxidizable NAPL components monitored during the PPTs. This dosage estimate will be greater than the average stoichiometric mass requirement for oxidation by permanganate for the suite of NAPL compounds.

To investigate the use of the potential field technique, PPT-ISCO was employed to: (1) estimate m_i^{PPT} through piecewise integration of simulated BTCs, (2) to confirm through the model that the mass oxidized represents the difference in mass between the BTCs, and (3) to quantify the increase in oxidant dosage due to the NOI. This treatability assessment was completed for the permanganate PPT into the MGP residual contaminated aquifer described by the field and

operating parameters outlined in the base case (Table 4-1 and Table 4-2). The permanganate NOI is characterized by the CFB Borden aquifer (Table 2-2).

The m_i^{PPT} estimated through piecewise integration of the simulated BTCs is compared to the oxidation estimates calculated by PPT-ISCO (Table 4-3). The percent difference between oxidation estimates (BTCs vs. PPT-ISCO) indicate that Equation (4-1) does accurately represent the mass of the MGP residual component oxidized by permanganate in the aquifer system. For NAPL components that are not oxidizable by permanganate, the estimate of m_i^{PPT} is negligible. The naphthalene PPT BTCs are presented in Figure 4-7.

The treatability assessment identifies the response of the components to oxidation (Figure 4-8). The total mass of MGP residual oxidized is 52 g-MGP residual/g-MnO4 consumed. The complete assessment is presented in Appendix E. The mass of each component oxidized is a function of the reaction rate (k_i), the weight percentage present in the MGP residual, and the stoichiometric mass balance requirement (β_i) (Equation (2-4)). Naphthalene has a relatively high reaction rate with permanganate and the highest weight percentage of all the components in the MGP residual composition, as a result it is the component with the greatest mass oxidized.

The bulk stoichiometric estimate of the permanganate mass ratio required to oxidize the MGP residual is 12 g-MnO_4/g-MGP. This value is calculated as the weighted mean of the stoichiometric mass ratio (β_i) and weight percentages of each of the oxidizable components. The site-specific oxidant dosage estimated from Equation (4-3) is 19 g-MnO_4/g-MGP residual oxidized. The difference from the bulk stoichiometric estimate highlights the effect of the NOI on the permanganate dosage required to oxidize the residual MGP. As the effect of NOI is decreased, the oxidant dosage will more closely approximate the bulk stoichiometric estimate (Appendix E).

Table 4-3. Comparison of oxidation estimates between BTC and PPT-ISCO and treatability expectations for representative MGP residual components

	Oxidation Estimates			Treatability Expectations
	BTCs (g)	**PPT-ISCO (g)**	**% diff**	**mg oxidized/ g MnO_4 consumed**
Naphthalene	62437	62562	0.2%	22
2-methylnaphthalene	14831	14846	0.1%	5
1-methnaphthalene	6922	6924	0.0%	2
	Total (all oxidizable MGP components)			52

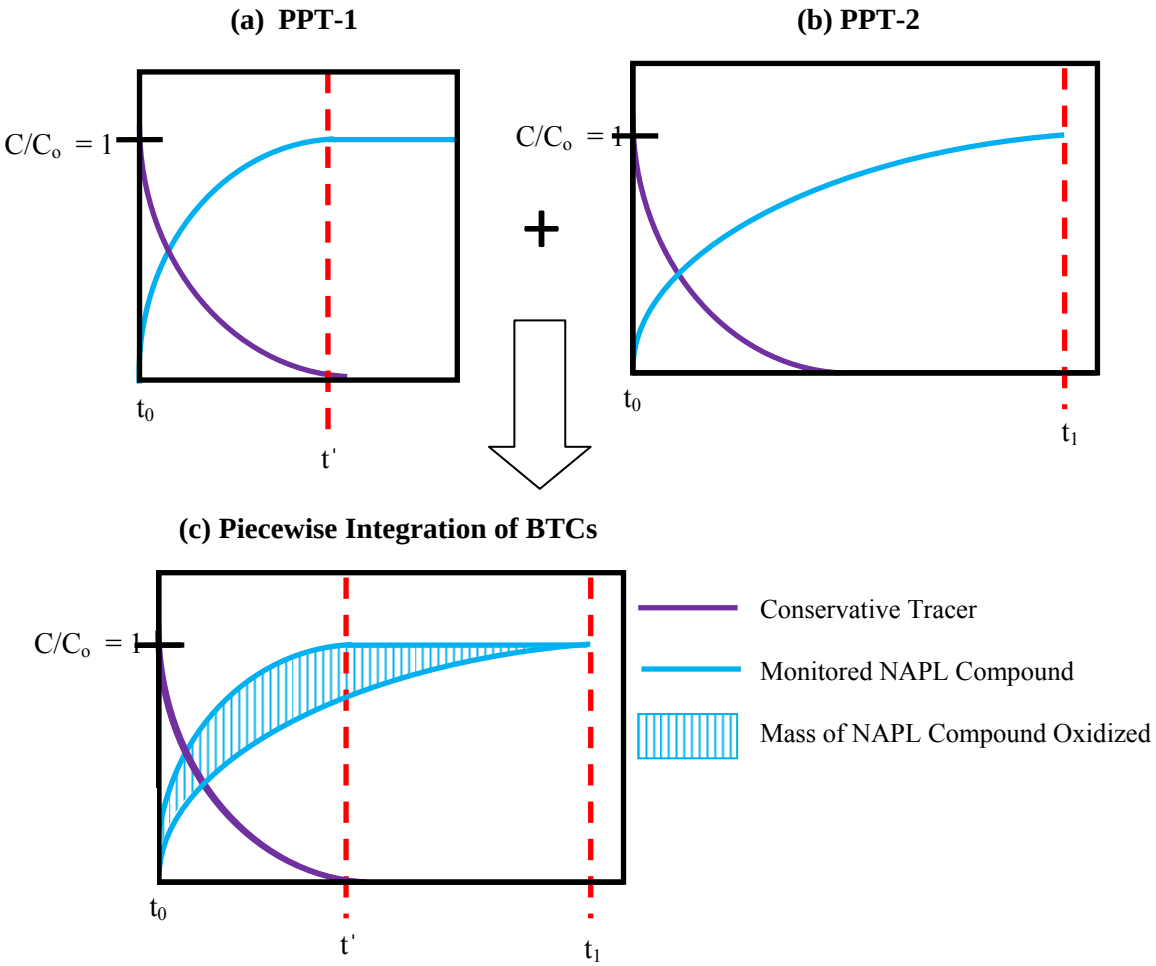

Figure 4-6. Treatability expectation schematic: (a) BTC with no oxidant injection, (b) BTC with oxidant injection, (c) Overlay of figures (a) and (b)

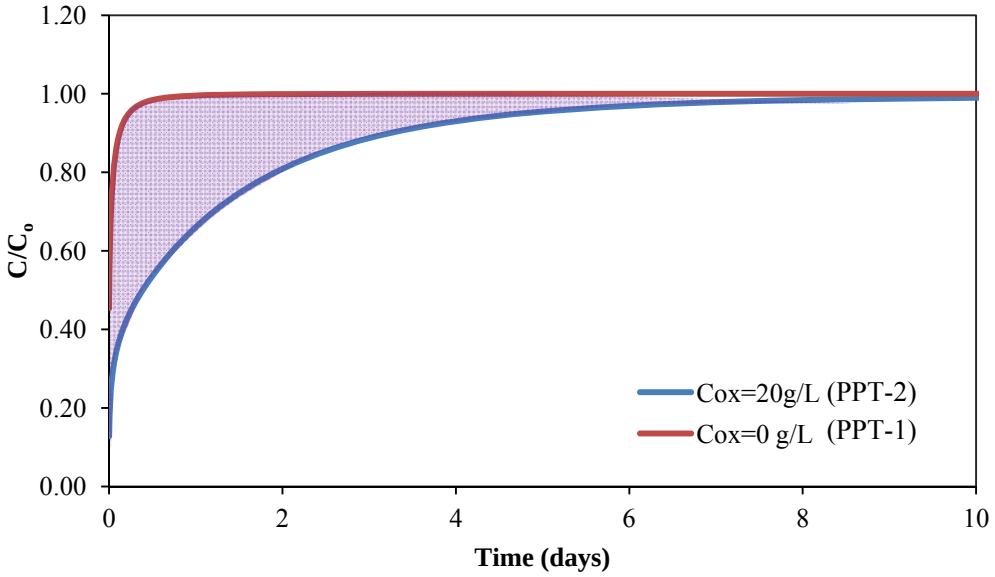

Figure 4-7. BTCs for naphthalene with and without oxidant injection. Oxidized mass is shaded purple.

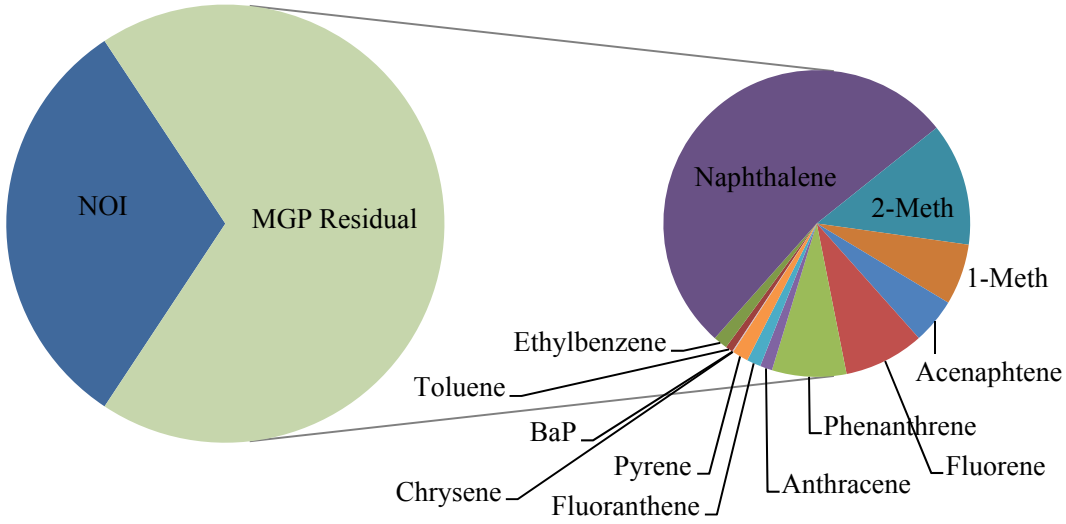

Figure 4-8. Distribution of permanganate consumption due to the NOI and MGP residual oxidation

4.4 Oxidant Behaviour

The oxidant behaviour during a PPT into a gasoline contaminated aquifer is examined. In this section PPT-ISCO is employed to investigate the effects of the NOI, and to observe oxidation and dissolution kinetic behaviour and gasoline treatability characteristics specific to each oxidant. The PPT and gasoline contaminated aquifer are described by the parameters outlined in the base case (Table 4-1 and Table 4-2). For a permanganate injection concentration of 20 g-$KMnO_4$/L, the persulfate concentration for an equal oxidizing potential is 45 g-$Na_2S_2O_8$/L based on the ratio of persulfate to permanganate equivalent weights.

The results for the permanganate PPT ($C_{ox}^{initial}$ = 20g-$KMnO_4$/L) into a gasoline contaminated aquifer is presented in Figure 4-9 (for gasoline composition A) and Figure 4-10 (for gasoline composition B). Details of the gasoline compositions, including weight percentages and reaction rates are provided in Appendix B. The results for both gasoline compositions are very comparable. The time for the components to approach unity remains approximately the same between the compositions (Figure 4-9(b) and Figure 4-10(b)). Characteristic oxidation and dissolution kinetic behaviour is seen in the fast region NAPL mass profiles (Figure 4-9(c) and (e) and Figure 4-10(c) and (e)). At 0.04 m from the injection well, the greatest percentage of mass dissolved (~ 95%) is from benzene, as a result of the high advective flux in this region and the high effective solubility of benzene. In the region 0.4 m from the well, a greater percentage of naphthalene has dissolved (~ 20%) in comparison to benzene (< 1%). At this location, the advective flux is substantially lower (Equation 2-2) and as a result of oxidation (naphthalene has a high reaction rate and the smallest weight percentage) the percentage of naphthalene dissolved is greater than the percentage of benzene (or any other component) dissolved. The percentage of mass dissolved (for each of the components) in Composition B is slightly less due to the increased weight percentage of each of the components. At 0.04 and 0.4 m, a minimal amount of mass has dissolved (< 1%) in the slow region (Figure 4-9(d) and (f) and Figure 4-10(d) and (f)) due to the lower mass transfer rate in the slow region.

The total percentage of permanganate consumed due to the NOI for compositions A and B is 40% and 32% respectively. With Composition B, the competition for oxidant between the gasoline and OAM is increased, and the amount of oxidant available to be consumed by the OAM is decreased. Oxidation of gasoline is increased 27% with Composition B, and is reflected

in the permanganate BTCs (Figure 4-9(a) and Figure 4-10(a)). This relationship also causes the difference (although trivial) between the site-specific oxidant dosage estimates (28.7 and 27.9 g-MnO_4/g-gasoline oxidized, for composition A and B respectively) (Table 4-4). The full treatability assessment is presented in Appendix E. The bulk estimate for the stoichiometric mass requirement for oxidation of the gasoline constituents by permanganate is 15.5 g-MnO_4/g-gasoline residual. The increase from the stoichiometric average is indicative of the effect of the NOI on the site-specific oxidant dosage.

Table 4-4. Summary of Treatability and Oxidant Dosage Estimates

	Composition A	Composition B
Total % of MnO_4 consumed by gasoline	60.3%	67.8 %
Total % of MnO_4 consumed by OAM	39.6 %	32.1 %
Oxidant dosage (g-oxidant consumed/g-gasoline oxidized)	28.7	27.9
NAPL treatability estimate (mg-gasoline oxidized/g oxidant consumed)	34.8	35.9

Second-order reaction rate coefficients for unactivated persulfate oxidation of gasoline components are between 2 and 3 orders-of-magnitudes slower than permanganate (Sra et al., 2010). As a result any base case comparison between persulfate and permanganate is not straightforward even after increasing the persulfate concentration to match equivalent oxidizing strengths. The low reaction rate coefficients are relevant when considering the duration of the reaction phase. For the purposes of observing the BTCs and dissolution kinetics that result from persulfate oxidation, the reaction phase duration for persulfate simulations was extended to 30 days. However because permanganate and persulfate cannot be compared, the results for the persulfate PPT ($C_{ox}^{initial}$ = 45g-$Na_2S_2O_8$/L) into a gasoline contaminated aquifer (gasoline composition A) are presented in Appendix E. Results for gasoline composition B is not repeated for persulfate as both compositions are likely to be qualitatively and quantitatively similar as was the case with the permanganate PPT.

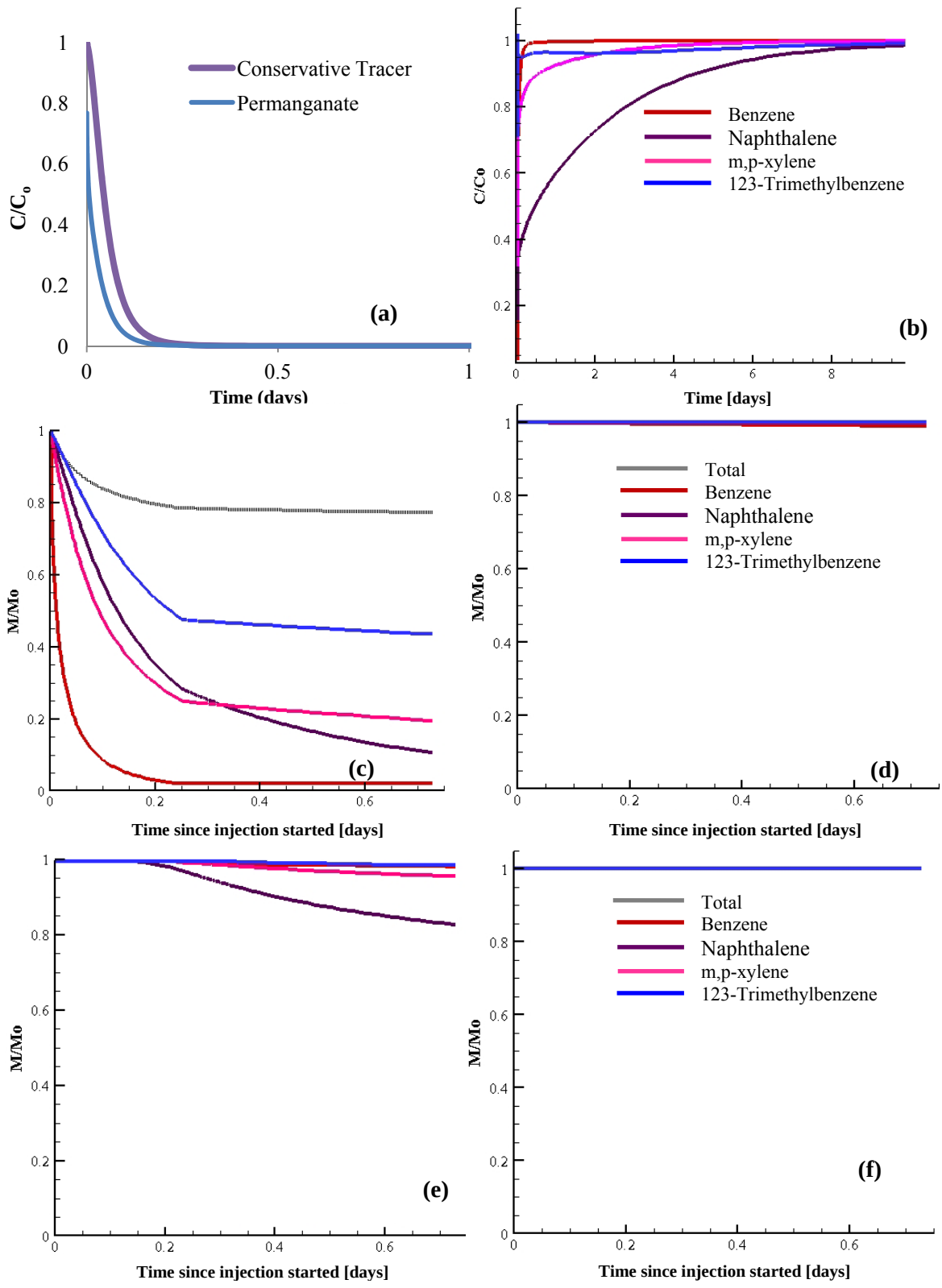

Figure 4-9. Results for permanganate PPT into gasoline contaminated aquifer (gasoline composition A): (a) normalized permanganate and tracer BTCs, (b) normalized gasoline component BTCs, fast region NAPL mass profiles at (c) 0.04m and (e) 0.4 m from the well, and slow region NAPL mass profiles at (d) 0.04 m and (f) 0.4 m from the well

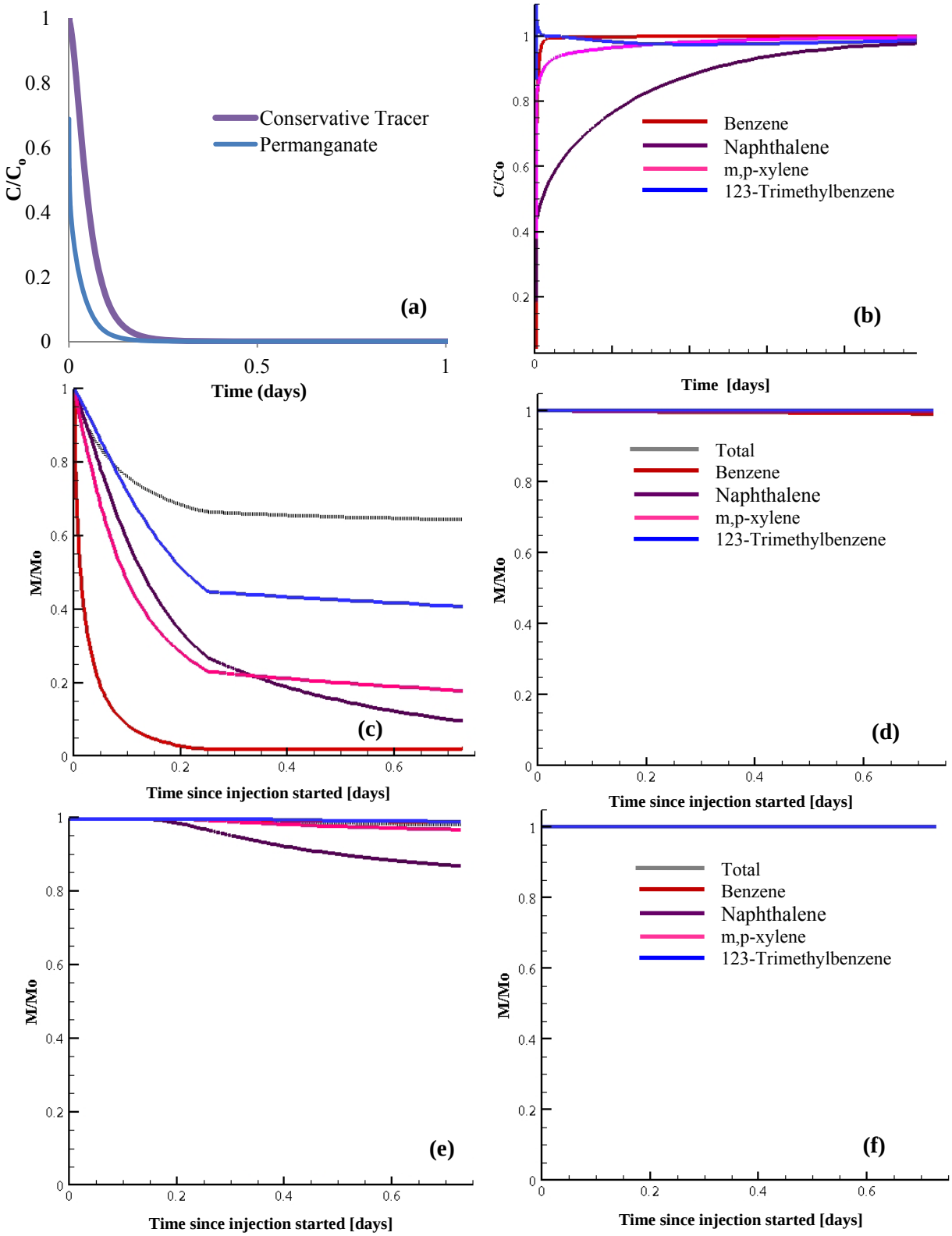

Figure 4-10. Results for permanganate PPT into gasoline contaminated aquifer (gasoline composition B): (a) normalized permanganate and tracer BTCs, (b) normalized gasoline component BTCs, fast region NAPL mass profiles at (c) 0.04m and (e) 0.4 m from the well, and slow region NAPL mass profiles at (d) 0.04 m and (f) 0.4 m from the well

5 Conclusions and Recommendations

A multi-species numerical model ('PPT-ISCO') in a radial coordinate system was developed to simulate a PPT with the injection of a conservative tracer and oxidant (persulfate or permanganate) into the saturated zone of a porous medium environment. The pore space may contain variable amounts of immobile, multicomponent, residual NAPL. The porous medium is assumed to be homogeneous with respect to grain size, mineral density and total porosity. The aquifer material contains a natural organic matter (NOM) fraction and/or other oxidizable aquifer material (OAM) species. The model is capable of simulating mass transport for an arbitrary number of conservative and reactive tracer/NAPL constituents subjected to chemical reactions in addition to advection and dispersion.

PPT-ISCO demonstrated potential to capture *in situ* NOI behaviour by producing simulated BTCs that compared favourably to PPT BTCs obtained in the field Borden experiments. The simulated BTCs were produced using NOI parameter estimates obtained from batch tests. These results confirmed the functionality of PPTs and PPT-ISCO to obtain the *in situ* NOI kinetics.

PPT-ISCO was employed to examine the link between the NOI parameters and the PPT BTCs. The results of varying the field operating parameters indicated that the oxidant BTCs could be scaled to match varying injection and extraction flow rates. Variations in the NOI kinetics highlighted that permanganate BTCs are primarily controlled by the permanganate fast reaction rate coefficient and the quantity of OAM in the aquifer. The spatial profiles of OAM consumption across the test zone revealed that the majority of the OAM consumed is from the fast fraction and occurs in the vicinity of the well where the permanganate concentration is greatest. The majority of the NOI parameters do not manifest in the BTCs, hence an accurate estimate of the permanganate fast reaction rate coefficient can be obtained from PPT-ISCO using literature estimates of the remaining parameters, and a COD test to estimate the quantity of OAM.

Using PPT-ISCO to estimate the site-specific permanganate NOD revealed that the previous method available to estimate NOD from a PPT may underestimate the NOD value. This can be overcome by using the model to adjust the NOD value to be more representative of the regions that consume the most permanganate mass. The method can be used to obtain two NOD estimates to provide intervals that are more representative of the site-specific NOD.

The sensitivity of the persulfate BTCs to the NOI parameters revealed that persulfate PPT BTCs can be characterized by a concentration plateau at early times as a result of increased ionic strength in the area around the well. In areas of high ionic strength, the activity coefficients of persulfate and the reactants are suppressed, and the overall degradation rate of persulfate is decreased. This relationship causes the concentration plateau observed at early times for high concentrations of persulfate. The ionic strength is primarily controlled by the initial persulfate concentration, and as persulfate degrades into sulphate and acid, the ionic strength will be enhanced. Over time the ionic strength will increase as persulfate degrades, and this will result in the continual suppression of the degradation rate everywhere. Graphical methods to estimate the persulfate degradation reaction rate revealed that an underestimated value of the degradation rate coefficient can be estimated from PPT BTCs. An accurate estimate of the degradation rate coefficient can be achieved from PPT-ISCO using the graphical estimate as a starting point during curve fitting.

Treatability PPTs were utilized to study the sensitivity of NAPL component BTCs to the controlling parameters. The results revealed that the BTCs are primarily controlled by the mass in the fast region, and the fast region mass transfer rate coefficient. Oxidation estimates from NAPL component BTCs were shown to approximate the mass of each NAPL component oxidized when compared to model calculations. A site-specific oxidant dosage was estimated from the BTCs that highlighted the effect of the NOI on the amount of permanganate required to treat the residual NAPL.

5.1 Recommendations

This research focused on developing a numerical model suitable for interpreting permanganate and persulfate PPT BTCs for NOI kinetic information and NAPL treatability estimates. The following recommendations are made to extend the results of this study:

- Illustrate the utility of PPT-ISCO through additional field experiments, using PPT-ISCO to help design field tests, and applying PPT-ISCO to quantify NOI kinetics and MGP treatability;
- Include a sorption component for the NAPL species. There is evidence to support that linear isotherms do not accurately represent sorbed concentrations of some NAPLs in

sandy aquifer material at high aqueous concentrations (J. F. Pankow & Cherry, 1996). It is also recognized that the assumption of an organic content controlled sorption may not be valid for fractions of organic carbon <0.001(Schwarzenbach & Westall, 1981). Other possible sorption models to include are the two isotherm-based models (Freundlich and Langmuir), and additional one-site kinetic and two-site kinetic sorption models (Phanikumar & McGuire, 2010) ;

- Include Monod kinetics as an option in the reaction term. During PPTs where the chemical equilibria are disturbed, subsurface biodegradation kinetics may behave dynamically and more closely approximate Monod kinetics (Burbery, Cassiani, Andreotti, Ricchiuto, & Semple, 2004). However Monod kinetics are seldom used in practice due to the difficulty in obtaining required utilization parameters (Burbery et al., 2004);

- Adapt the model to account for an ambient hydraulic gradient during the reaction phase. For sites where a longer reaction phase is required, accounting for the drift phase will help to understand how much of the oxidant mass has shifted in the direction of the gradient during the drift phase, and if some of the oxidant mass has drifted beyond the influence of extraction; and

- Include more oxidant choices, including peroxide and activated persulfate (with various activation agents).

References

Anderson, D. A., Tannehill, J. C., & Pletcher, R. H. (1984). *Computational fluid mechanics and heat transfer* Taylor & Francis.

Bachmat, Y., Mandel, S., & Bugayevski, M. (1988). A single-well tracer technique for evaluating aquifer parameters, I. theoretical work. *Journal of Hydrology, 99*(1-2), 143-163.

Barcelona, M.J., Holm,T.R. (1991). Oxidation-reduction capacities of aquifer solids. *Environmental Science and Technology, 25*(9), 1565-1572.

Bear, J. (1979). *Hydraulics of groundwater*. Mineola: Dover Publications.

Birak, P. S., & Miller, C. T. (2009). Dense non-aqueous phase liquids at former manufactured gas plants: Challenges to modeling and remediation. *Journal of Contaminant Hydrology, 105*(3-4), 81-98.

Borden, R. C., & Kao, C. (1992). Evaluation of groundwater extraction for remediation of petroleum-contaminated aquifers. *Water Environment Research, 64*(1), 28-36.

Brewster, M. L., Annan, A. P., Greenhouse, J. P., Kueper, B. H., Olhoeft, G. R., Redman, J. D., et al. (1995). Observed migration of a controlled DNAPL release by geophysical methods. *Ground Water,33*(6), 977-987.

Burbery, L., Cassiani, G., Andreotti, G., Ricchiuto, T., & Semple, K. T. (2004). Single-well reactive tracer test and stable isotope analysis for determination of microbial activity in a fast hydrocarbon-contaminated aquifer. *Environmental Pollution, 129*(2), 321-330.

Carrayrou, J., Mosé, R., & Behra, P. (2004). Operator-splitting procedures for reactive transport and comparison of mass balance errors. *Journal of Contaminant Hydrology, 68*(3-4), 239.

Chen, C., & Woodside, G. D. (1988). Analytical solution for aquifer decontamination by pumping. *Water Resources Research, 24*(8), 1329-1338.

Connors, K. A. (1990). *Chemical kinetics: The study of reaction rates in solution* VCH.

Davis, B. M., Istok, J. D., & Semprini, L. (2002). Push–pull partitioning tracer tests using radon-222 to quantify non-aqueous phase liquid contamination. *Journal of Contaminant Hydrology, 58*(1-2), 129-146.

Davis, B. M., Istok, J. D., & Semprini, L. (2005). Numerical simulations of radon as an in situ partitioning tracer for quantifying NAPL contamination using push–pull tests. *Journal of Contaminant Hydrology, 78*(1-2), 87-103.

Drever, J. I., & McKee, C. R. (1980). *The push-pull test: A method of evaluating formation adsorption parameters for redicting the environmental effects on in situ coal gasification and uranium recovery* In Situ Consulting.

Eberhardt, C., & Grathwohl, P. (2002). Time scales of organic contaminant dissolution from complex source zones: Coal tar pools vs. blobs. *Journal of Contaminant Hydrology, 59*(1-2), 45-66.

Ferziger, J. H., & Peri M. (2002). *Computational methods for fluid dynamics* Springer.

Forsey, S. P. (2004). In situ chemical oxidation of creosote/coal tar residuals: Experimental and numerical investigation. (Dissertation for the Doctoral Degree, University of Waterloo).

Frind, E. O. (1988). Solution of the advection-dispersion equation with free exit boundary. *Numerical Methods for Partial Differential Equations, 4*(4), 301-313.

Gates, Dianne D., Siegrist, Robert L., Cline,Steven R. (1995). Chemical oxidation of contaminants in clay or sandy soil. pp. 582-588.

Gates-Anderson, D. D., Siegrist, R. L., & Cline, S. R. (2001). Comparison of potassium permanganate and hydrogen peroxide as chemical oxidants for organically contaminated soils.*127*(4), 337-347.

Gelhar, L. W., & Collins, M. A. (1971). General analysis of longitudinal dispersion in nonuniform flow. *Water Resources Research, 7*(6), 1511-1521.

Geller, J. T., & Hunt, J. R. (1993). Mass transfer from nonaqueous phase organic liquids in water-saturated porous media. *Water Resources Research, 29*(4), 833-845.

Goltz, M. N., & Oxley, M. E. *Analytical modeling of aquifer decontamination by pumping when transport is affected by rate-limited sorption* AGU.

Hageman, K. J., Field, J. A., Istok, J. D., & Schroth, M. H. (2003). "Forced mass balance" technique for estimating in situ transformation rates of sorbing solutes in groundwater. *Environmental Science & Technology, 37*(17), 3920-3925.

Haggerty, R., Fleming, S. W., & McKenna, S. A. (2000). *STAMMT-R solute transport and multirate mass transfer in radial coordinates version 1.01* No. SAND99-0164). Albuquerque, New Mexico: Sandia National Laboratories.

Haggerty, R., Schroth, M. H., & Istok, J. D. (1998). Simplified method of "push-pull" test data analysis for determining in situ reaction rate coefficients. *Ground Water, 36*(2), 314-324.

Hall, S. H., Luttrell, S. P., & Cronin, W. E. (1991). A method for estimating effective porosity and ground-water velocity. *Ground Water, 29*(2), 171-174.

Haselow, J. S., Siegrist, R. L., Crimi, M., & Jarosch, T. (2003). Estimating the total oxidant demand for in situ chemical oxidation design. *Remediation Journal, 13*(4), 5-16.

Hellerich, L. A., Oates, P. M., Johnson, C. R., Nikolaidis, N. P., Harvey, C. F., & Gschwend, P. M. (2003). Bromide transport before, during, and after colloid mobilization in push-pull tests and the implications for changes in aquifer properties. *Water Resources Research, 39*(10), 1301.

Hoopes, J. A., & Harleman, D. R. F. (1967). Dispersion in radial flow from a recharge well. *J.Geophys.Res., 72*(14), 3595-3607.

Hsieh, P. A. (1986). A new formula for the analytical solution of the radial dispersion problem. *Water Resources Research, 22*(11), 1597-1605.

Huang, J., Christ, J. A., & Goltz, M. N. (2010). Analytical solutions for efficient interpretation of single-well push-pull tracer tests. *Water Resources Research, 46*(8), W08538.

Huang, K., Hoag, G. E., Chheda, P., Woody, B. A., & Dobbs, G. M. (2002). Chemical oxidation of trichloroethylene with potassium permanganate in a porous medium. *Advances in Environmental Research, 7*(1), 217-229.

Imhoff, P. T., Jaffé, P. R., & Pinder, G. F. (1994). An experimental study of complete dissolution of a nonaqueous phase liquid in saturated porous media. *Water Resources Research, 30*(2), 307-320.

Istok, J. D., & Field, J. A. (1999). *In-situ, field scale evaluation of surfactant-enhanced DNAPL recovery using a single-well, "Push-pull" test* (Environmental Management Sciences Program Final Report No. project 55196-OR)U.S. Department of Energy. Retrieved from http://www.osti.gov/em52/final_reports/55196.pdf

Istok, J. D. (1989). *Groundwater modeling by the finite element method* American Geophysical Union.

Istok, J. D., Humphrey, M. D., Schroth, M. H., Hyman, M. R., & O'Reilly, K. T. (1997). Single-well, "push-pull" test for in situ determination of microbial activities. *Ground Water, 35*(4), 619-631.

Istok, J. D., Field, J. A., Schroth, M. H., Davis, B. M., & Dwarakanath, V. (2002). Single-well "Push−Pull" partitioning tracer test for NAPL detection in the subsurface. *Environmental Science & Technology, 36*(12), 2708-2716.

J. Richard Elliott, & Lira, C. T. (1999). *Introductory chemical engineering thermodynamics* Prentice Hall PTR.

J.J., K., & J., M. (1995). Critical assessment of the operator-splitting technique in solving the advection--dispersion--reaction equation: 1. first-order reaction. *Advances in Water Resources, 18*(2), 89-100.

Jin, M., Delshad, M., Dwarakanath, V., McKinney, D. C., Pope, G. A., Sepehrnoori, K., et al. (1995). Partitioning tracer test for detection, estimation, and remediation performance assessment of subsurface nonaqueous phase liquids. *Water Resources Research, 31*(5), 1201-1211.

Jonathan H., S. (1973). Total organic carbon in seawater â€" comparison of measurements using persulfate oxidation and high temperature combustion. *Marine Chemistry, 1*(3), 211-229.

Karickhoff, S. W., Brown, D. S., & Scott, T. A. (1979). Sorption of hydrophobic pollutants on natural sediments. *Water Research, 13*(3), 241-248.

Ko, S., & Ji, S. (2007). In situ push-pull tests for the determination of TCE degradation and permanganate consumption rates. *Environmental Geology, 53*(2), 359-364.

Leap, D. I., & Kaplan, P. G. *A single-well tracing method for estimating regional advective velocity in a confined aquifer: Theory and preliminary laboratory verification* AGU.

Lehr, J. H., Hyman, M., & Gass, T. (2001). *Handbook of complex environmental remediation problems* Lightning Source Inc.

Leonard, B. P., & Drummond, J. E. (1995). Why you should not use 'Hybrid', 'Power-law' or related exponential schemes for convective modelling—there are much better alternatives. *International Journal for Numerical Methods in Fluids, 20*(6), 421-442.

Mackay, D. (2006). *Handbook of physical-chemical properties and environmental fate for organic chemicals: Introduction and hydrocarbons* CRC Press/Taylor \& Francis.

Mackay, D. M., Freyberg, D. L., Roberts, P. V., & Cherry, J. A. (1986). A natural gradient experiment on solute transport in a sand aquifer: 1. approach and overview of plume movement. *Water Resources Research, 22*(13), 2017-2029.

Malone, D. R., Kao, C., & Borden, R. C. (1993). Dissolution and biorestoration of nonaqueous phase hydrocarbons: Model development and laboratory evaluation. *Water Resources Research, 29*(7), 2203-2213.

Morshed, J., & Kaluarachchi, J. J. (1995). Critical assessment of the operator-splitting technique in solving the advection-dispersion-reaction equation: 2. monod kinetics and coupled transport.*Advances in Water Resources, 18*(2), 101-110.

Mumford, K. G. (2002). *Investigation of natural oxidant demand reactions in a sandy aquifer material.* Unpublished Master of Applied Science in Civil Engineering, University of Waterloo, Waterloo.

Mumford, K. G., Lamarche, C. S., & Thomson, N. R. (2004). Natural oxidant demand of aquifer materials using the push-pull technique. *Journal of Environmental Engineering, 130*(10), 1139-1146.

Nielsen, P. H., & Christensen, T. H. (1994). Variability of biological degradation of aromatic hydrocarbons in an aerobic aquifer determined by laboratory batch experiments. *Journal of Contaminant Hydrology,* (15), 305.

Pankow, J. F., & Johnson, R. L. (1996). Physical and chemical properties of dense nonaqueous phase liquid (DNAPL) compounds. In J. F. Pankow, & J. A. Cherry (Eds.), *Dense chlorinated solvents and other DNAPLs in groundwater* (). Portland, Oregon: Waterloo Press.

Pankow, J. F., & Cherry, J. A. (1996). *Dense chlorinated solvents and other DNAPLs in groundwater: History, behavior, and remediation* Waterloo Press.

Patankar, S. V.,. (1980). *Numerical heat transfer and fluid flow / suhas V. patankar* Hemisphere Pub. Corp. ; McGraw-Hill, Washington : New York.

Phanikumar, M. S., & McGuire, J. T. (2010). A multi-species reactive transport model to estimate biogeochemical rates based on single-well push–pull test data. *Computers & Geosciences, 36*(8), 997-1004.

Pitterle, M. T., Andersen, R. G., Novak, J. T., & Widdowson, M. A. (2005). Push-pull tests to quantify in situ degradation rates at a phytoremediation site. *Environmental Science & Technology, 39*(23), 9317-9323.

R., A., A., R., & M., S. (1994). *Spatial variability in biodegradation rates as evidenced by methane production from an aquifer*. Washington, DC, ETATS-UNIS: American Society for Microbiology.

Radhakrishna Pillai, A. C. (2001). Fourth-order exponential finite difference methods for boundary value problems of convective diffusion type. *International Journal for Numerical Methods in Fluids,37*(1), 87-106.

Runkel, R. L., & Chapra, S. C. (1993). An efficient numerical solution of the transient storage equations for solute transport in small streams. *Water Resources Research, 29*(1), 211-215.

Sahl, J. W., Munakata-Marr, J., Crimi, M. L., & Siegrist, R. L. (2007). Coupling permanganate oxidation with microbial dechlorination of tetrachloroethene. *Water Environment Research, 79*(1), 5-12.

Schnarr, M., Truax, C., Farquhar, G., Hood, E., Gonullu, T., & Stickney, B. (1998). Laboratory and controlled field experiments using potassium permanganate to remediate trichloroethylene and perchloroethylene DNAPLs in porous media. *Journal of Contaminant Hydrology, 29*(3), 205.

Schroth, M. H., Istok, J. D., & Haggerty, R. (2000). In situ evaluation of solute retardation using single-well push–pull tests. *Advances in Water Resources, 24*(1), 105-117.

Schroth, M. H., Kleikemper, J., Bolliger, C., Bernasconi, S. M., & Zeyer, J. (2001). In situ assessment of microbial sulfate reduction in a petroleum-contaminated aquifer using push–pull tests and stable sulfur isotope analyses. *Journal of Contaminant Hydrology, 51*(3-4), 179-195.

Schroth, M. H., & Istok, J. D. (2006). Models to determine first-order rate coefficients from single-well push-pull tests. *Ground Water, 44*(2), 275-283.

Schwarzenbach, R. P., & Westall, J. (1981). Transport of nonpolar organic compounds from surface water to groundwater. laboratory sorption studies. *Environmental Science & Technology, 15*(11), 1360-1367.

Seol, Y., Zhang, H., & Schwartz, F. W. (2003). A review of in situ chemical oxidation and heterogeneity. *Environmental Engineering Geoscience, 9*(1), 37-49.

Siegrist R. L., Urynowicz M. A., West O. R., Crimi M. L. and Lowe K. S. (Eds.), *Principles and practices of in situ chemical oxidation using permanganate*. Columbus, Ohio: Battelle Press.

Snodgrass, M. F., & Kitanidis, P. K. (1998). A method to infer in situ reaction rates from push-pull experiments. *Ground Water, 36*(4), 645-650.

Spiegel, M. R. (1958). *Applied differential equations* Prentice-Hall.

Sra, K. S., Thomson, N. R., & Barker, J. F. (2010). Persistence of persulfate in uncontaminated aquifer materials. *Environmental Science & Technology, 44*(8), 3098-3104.

Strang, G. (1968). On the construction and comparison of difference schemes. *SIAM Journal on Numerical Analysis, 5*(3), 506-517.

Struse, A. M., Siegrist, R. L., Dawson, H. E., & Urynowicz, M. A. (2002). Diffusive transport of permanganate during in situ oxidation.*128*(4), 327-334.

Sudicky, E. A., Cherry, J. A., & Frind, E. O. (1983). Migration of contaminants in groundwater at a landfill: A case study : 4. A natural-gradient dispersion test. *Journal of Hydrology, 63*(1-2), 81-108.

Tang, D. H., & Babu, D. K. (1979). Analytical solution of a velocity dependent dispersion problem. *Water Resources Research, 15*(6), 1471-1478.

Thomson, N. R., Hood, E. D., & Farquhar, G. J. (2007). Permanganate treatment of an emplaced DNAPL source. *Ground Water Monitoring & Remediation, 27*(4), 74-85.

Thomson, N. R. (2010, FMC Environmental Solutions: Peroxygen Talk Archive). Natural oxidant interaction (NOI): A paradigm shift. http://www.envsolutions.fmc.com/ResourceCenter/PeroxygenTalkArchive.aspx?itemId=1093

Tomich, J. F., Dalton Jr., R. L., Deans, H. A., Rice, U., & Shallenberger, L. K. (1973). Single-well tracer method to measure residual oil saturation. *Society of Petroleum Engineers, Volume 25*(Number 2), 211.

Urmann, K., Gonzalez-Gil, G., Schroth, M. H., Hofer, M., & Zeyer, J. (2005). New field method: gas Push−Pull test for the in-situ quantification of microbial activities in the vadose zone. *Environmental Science & Technology, 39*(1), 304-310.

Valocchi, A. J. *Effect of radial flow on deviations from local equilibrium during sorbing solute transport through homogeneous soils* - AGU.

Versteeg, H. K., & Malalasekera, W. (2007). *An introduction to computational fluid dynamics: The finite volume method* Pearson Education Ltd.

Waldemer, R. H., Tratnyek, P. G., Johnson, R. L., & Nurmi, J. T. (2007). Oxidation of chlorinated ethenes by heat-activated persulfate: Kinetics and products. *Environmental Science & Technology, 41*(3), 1010-1015.

Wang, H., & Anderson, M. P. (1995). *Introduction to groundwater modeling: Finite difference and finite element methods* Academic Press.

White, M. D., & Oostrom, M. (2000). *STOMP. subsurface transport over multiple phases, verison 2.0, theory guide*. Richland, Washington: Pacific Northwest National Laboratory.

Xu, X., & Thomson, N. R. (2008). Estimation of the maximum consumption of permanganate by aquifer solids using a modified chemical oxygen demand test. *Journal of Environmental Engineering,134*(5), 353-361.

Xu, X., & Thomson, N. R. (2008). Estimation of the maximum consumption of permanganate by aquifer solids using a modified chemical oxygen demand test.*134*(5), 353-361.

Xu, X., & Thomson, N. R. (2009). A long-term bench-scale investigation of permanganate consumption by aquifer materials. *Journal of Contaminant Hydrology, 110*(3-4), 73-86.

Xu, X., & Thomson, N. R. (2010). Hydrogen peroxide persistence in the presence of aquifer materials. *Soil and Sediment Contamination: An International Journal, 19*(5), 602-616.

Yan, Y. E., & Schwartz, F. W. (1999). Oxidative degradation and kinetics of chlorinated ethylenes by potassium permanganate. *Journal of Contaminant Hydrology, 37*(3-4), 343-365.

Yang, C., Park, M., & Zhu, C. (2007). A method for estimating *in situ* Reaction rates from push-pull experiments for arbitrary solute background concentrations. *Environmental & Engineering Geoscience, XIII*(4), 345-354.

Zheng, C., & Wang, P. (1999). *MT3DMS: A modular three-dimensional multispecies transport model for simulation of advection, dispersion, and chemical reactions of contaminants in groundwater systems, technical report*. Vicksburg, Miss.: U.S. Army Corpss of Eng.

Zlotnik, V. A., & Logan, J. D. (1996). Boundary conditions for convergent radial tracer tests and effect of well bore mixing volume. *Water Resources Research, 32*(7), 2323-2328.

Appendix A - Input Files

Input file: MGP residual oxidation by permanganate

0.01 1.1 20. 1.e+3 0.8625 1.0 0 (sn, density, c ox, lamda, tend,tox,iox dep						
21 (ncomp	(MW[g/mol], Cmax [mg/L], f_S/f_L,		k[L/g-min],	Cn [mg/kg],	Beta [g/g],	logKoc [L/kg])
Benzene	78.1	1780.	1.00	0.00	550.	0.00	1.78
Toluene	92.1	534.8	1.00	2.7e-4	2120.	15.4	2.16
Ethylbenzene	106.2	161.2	1.00	2.3e-3	1860.	15.5	2.32
Naphthalene	128.2	31.7	0.30	4.2e-3	70000.	14.7	3.09
2-Methltnap	142.0	25.4	0.86	7.3e-3	33400.	14.9	3.93
1-Methltnap	142.2	28.05	1.00	5.1e-3	23500.	14.9	3.36
Acenaphthylene	154.0	9.8	0.22	0.00	610.	0.0	3.30
Acenaphtene	154.2	3.93	0.2	8.0e-2	11900.	4.9	3.70
Fluorene	166.2	1.98	0.16	1.6e-1	11600.	9.5	3.95
Phenanthrene	178.2	1.18	0.28	1.6e-1	32600.	7.9	4.40
Anthracene	178.0	0.05	0.01	5.0e-2	8570.	8.0	4.39
Fluoranthene	202.3	0.26	0.21	3.3e-1	13400.	9.3	4.69
Pyrene	202.3	0.13	0.11	0.60	13200.	9.3	4.85
BaA	228.0	0.014	0.04	0.00	4900.	0.0	5.66
Chrysene	228.0	0.002	0.0097	4.7e-3	5100.	14.5	5.49
BbF	252.0	0.00323	0.039	0.00	2150.	0.0	6.08
BaP	252.0	0.0038	0.03	6.0e-1	3900.	13.1	6.07
Indeno	276.0	0.062	0.0451	0.00	2610.	0.0	6.54
DahA	278.0	0.0005	0.004	0.00	490.	0.0	6.31
BighiP	276.0	0.00026	0.003	0.00	3110.	0.0	6.20
Bulk	250.0	0.003	1.000	0.00	1.	0.0	0.00

Input file: Gasoline residual (Composition A) oxidation by permanganate

```
0.01  1.1  20.  1.e+3  0.8625 1.0  0 (sn, density, c_ox, lamda, tend,tox,iox_dep
10  (ncomp        (MW[g/mol], Cmax [mg/L], f_S/f_L,  k[L/g-min], Cn [mg/kg], Beta [g/g], logKoc [L/kg])
Benzene              78.1   1850.     1.00    0.0000      16400.      0.0      1.78
Toluene              92.1   515.0     1.00    2.7e-4      91100.     15.4      2.16
Ethylbenzene        106.2   161.2     1.00    2.3e-3      26100.     15.5      2.32
Naphthalene         128.2   31.7      0.30    4.2e-3        200.     14.7      3.09
o-xylene            106.2   173.      1.00    4.6e-4      28400.     15.6      3.12
m,p-xylene          106.2   174.      1.00    5.0e-4      68570.     15.6      2.52
123-TMB             120.2   69.       1.00    5.0e-4       7100.     15.7      2.80
124-TMB             120.2   56.       1.00    5.0e-4      29700.     15.7      3.28
135-TMB             120.2   48.9      1.000   5.0e-4       9900.     15.7      2.82
Bulk                250.0   0.003     1.000    0.00          1.      0.0      0.00
```

Input file: Gasoline residual (Composition B) oxidation by permanganate

```
0.01  1.1  20.  1.e+3  0.8625 1.0  0 (sn, density, c_ox, lamda, tend,tox,iox_dep
10  (ncomp        (MW[g/mol], Cmax [mg/L], f_S/f_L,  k[L/g-min], Cn [mg/kg], Beta [g/g], logKoc [L/kg])
Benzene              78.1   1850.     1.00    0.0000      34353.      0.0      1.78
Toluene              92.1   515.0     1.00    2.7e-4     109053.     15.4      2.16
Ethylbenzene        106.2   161.2     1.00    2.3e-3      44053.     15.5      2.32
Naphthalene         128.2   31.7      0.30    4.2e-3      18153.     14.7      3.09
o-xylene            106.2   173.      1.00    4.6e-4      46353.     15.6      3.12
m,p-xylene          106.2   174.      1.00    5.0e-4      86523.     15.6      2.52
123-TMB             120.2   69.       1.00    5.0e-4      25053.     15.7      2.80
124-TMB             120.2   56.       1.00    5.0e-4      47653.     15.7      3.28
135-TMB             120.2   48.9      1.000   5.0e-4      27853.     15.7      2.82
Bulk                250.0   0.003     1.000    0.00          1.      0.0      0.00
```

Input file: Gasoline residual (Composition A) oxidation by persulfate

```
0.01  1.1  50.  1.e+3  0.8625 1.0  0 (sn, density, c_ox, lamda, tend,tox,iox_dep
10  (ncomp        (MW[g/mol], Cmax [mg/L], f_S/f_L,  k[L/g-min], Cn [mg/kg], Beta [g/g], logKoc [L/kg])
Benzene              78.1   1850.     1.00    1.3e-6      16400.     36.9      1.78
Toluene              92.1   515.0     1.00    2.0e-6      91100.     37.5      2.16
Ethylbenzene        106.2   161.2     1.00    2.0e-6      26100.     38.0      2.32
Naphthalene         128.2   31.7      0.30    1.1e-6        200.     36.0      3.09
o-xylene            106.2   173.      1.00    9.8e-7      28400.     38.0      3.12
m,p-xylene          106.2   174.      1.00    8.6e-7      68570.     38.0      2.52
123-TMB             120.2   69.       1.00    5.4e-7       7100.     38.4      2.80
124-TMB             120.2   56.       1.00    9.2e-7      29700.     38.4      3.28
135-TMB             120.2   48.9      1.000   4.2e-7       9900.     38.4      2.82
Bulk                250.0   0.003     1.000    0.000          1.      0.0      0.00
```

Input file: Gasoline residual (Composition B) oxidation by persulfate

```
0.01  1.1  50.  1.e+5  0.8625 1.0  0 (sn, density, c ox, lamda, tend,tox,iox dep
10  (ncomp        (MW[g/mol], Cmax [mg/L], f_S/f_L,  k[L/g-min], Cn [mg/kg], Beta [g/g], logKoc [L/kg])
Benzene              78.1   1850.     1.00    1.3e-6      34353.     36.9      1.78
Toluene              92.1   515.0     1.00    2.0e-6     109053.     37.5      2.16
Ethylbenzene        106.2   161.2     1.00    2.0e-6      44053.     38.0      2.32
Naphthalene         128.2   31.7      0.30    1.1e-6      18153.     36.0      3.09
o-xylene            106.2   173.      1.00    9.8e-7      46353.     38.0      3.12
m,p-xylene          106.2   174.      1.00    8.6e-7      86523.     38.0      2.52
123-TMB             120.2   69.       1.00    5.4e-7      25053.     38.4      2.80
124-TMB             120.2   56.       1.00    9.2e-7      47653.     38.4      3.28
135-TMB             120.2   48.9      1.000   4.2e-7      27853.     38.4      2.82
Bulk                250.0   0.003     1.000    0.000          1.      0.0      0.00
```

Appendix B - Baseline Gasoline Analysis (Chevron Corporation)

API 94-02 whole baseline gasoline
CHEVRON RESEARCH GASOLINE ANALYSIS

Sample Name: 6018638 API BASE GASOLINE Customer: CARR
Acquisition Date: 5-Apr-1996 Acquisition Time: 19:55
Channel #: 13 Analysis: GAS0126 Sample #: 3 Injection #: 1

*** DETAILED COMPOSITION, PERCENT ***

1. BY VOLUME

C NO.	PARA	OLEF	NAPH	AROM	UNCL HC	TOTALS BY C #	NORMAL PARA	NON-ALKYL I-PARA	ALKYL I-PARA	CYCLO-PENT	CYCLO-HEX
3-	0.00	0.00	******	******	******	0.00	0.00	******	******	******	******
4	4.68	0.06	******	******	******	4.74	4.59	0.09	******	******	******
5	12.38	3.71	0.18	******	******	16.26	2.89	9.49	******	0.18	******
6	12.30	3.17	1.62	1.40	******	18.49	2.29	10.01	******	1.36	0.26
7	7.69	1.94	1.66	7.85	******	19.15	1.18	6.52	******	0.98	0.69
8	7.30	0.53	1.55	10.60	0.18	20.16	0.52	2.94	3.83	0.91	0.64
9	1.54	0.00	0.87	7.87	0.30	10.58	0.22	1.22	0.10	0.08	0.79
10	1.08	0.00	0.05	4.34	0.52	6.00	0.00	0.84	0.24	0.00	0.05
11	0.35	0.00	0.00	1.98	0.48	2.80	0.00	0.35	0.00	0.00	0.00
12+	0.14	0.00	0.00	0.21	1.46	1.82	0.11	0.04	0.00	0.00	0.00
TOT	47.47	9.40	5.95	34.25	2.93	100.00	11.79	31.51	4.17	3.51	2.44

2. BY WEIGHT

C NO.	PARA	OLEF	NAPH	AROM	UNCL HC	TOTALS BY C #	NORMAL PARA	NON-ALKYL I-PARA	ALKYL I-PARA	CYCLO-PENT	CYCLO-HEX
3-	0.00	0.00	******	******	******	0.00	0.00	******	******	******	******
4	3.64	0.05	******	******	******	3.69	3.57	0.07	******	******	******
5	10.31	3.28	0.18	******	******	13.77	2.42	7.89	******	0.18	******
6	10.84	2.94	1.64	1.64	******	17.07	2.02	8.82	******	1.37	0.27
7	7.06	1.86	1.69	9.11	******	19.72	1.08	5.98	******	0.98	0.71
8	6.84	0.51	1.61	12.30	0.18	21.45	0.49	2.76	3.59	0.94	0.67
9	1.48	0.00	0.92	9.20	0.30	11.91	0.21	1.18	0.10	0.08	0.84
10	1.06	0.00	0.06	5.19	0.52	6.84	0.00	0.83	0.24	0.00	0.06
11	0.34	0.00	0.00	2.52	0.50	3.35	0.00	0.34	0.00	0.00	0.00
12+	0.14	0.00	0.00	0.27	1.81	2.22	0.11	0.04	0.00	0.00	0.00
TOT	41.73	8.63	6.10	40.24	3.30	100.00	9.90	27.91	3.92	3.55	2.55

3. BY MOLAR

C NO.	PARA	OLEF	NAPH	AROM	UNCL HC	TOTALS BY C #	NORMAL PARA	NON-ALKYL I-PARA	ALKYL I-PARA	CYCLO-PENT	CYCLO-HEX
3-	0.00	0.00	******	******	******	0.00	0.00	******	******	******	******
4	6.00	0.08	******	******	******	6.08	5.89	0.12	******	******	******
5	13.71	4.49	0.24	******	******	18.44	3.22	10.48	******	0.24	******
6	12.07	3.36	1.87	2.02	******	19.31	2.25	9.81	******	1.56	0.31
7	6.75	1.82	1.65	9.48	******	19.71	1.03	5.72	******	0.96	0.69
8	5.75	0.43	1.38	11.11	0.15	18.82	0.41	2.32	3.01	0.80	0.57
9	1.11	0.00	0.70	7.34	0.23	9.38	0.16	0.88	0.07	0.06	0.64
10	0.72	0.00	0.04	3.73	0.36	4.85	0.00	0.56	0.16	0.00	0.04
11	0.21	0.00	0.00	1.65	0.31	2.17	0.00	0.21	0.00	0.00	0.00
12+	0.08	0.00	0.00	0.17	0.99	1.24	0.06	0.02	0.00	0.00	0.00
TOT	46.39	10.19	5.88	35.51	2.04	100.00	13.02	30.13	3.24	3.62	2.25

GRP. TYPE, VOL %: P = 48.91, O = 9.68, N = 6.13, A = 35.28, Saturates = 55.03
DIENE CONTENT = 438. vol ppm AVG MW = 95.9 API GR. = 56.8 SP. GR. =0.7516
OCTANE NUMBER: (from pure values) RON = 84.8 MON = 79.4
(from blending values) RON = 87.9 MON = 79.3
CARBON-HYDROGEN RATIO =6.577 STOICH. AIR-FUEL RATIO =14.49 lbs air/lbs fuel
BTU/lb = 11445. NET, 12334. GROSS; BTU/gal = 71783. NET, 77356. GROSS
REID VAPOR PRESSURE = 8.1 BROMINE NO. = 17.1

AROMATIC HCS

CODE	MOL.	VOL.	WT.	NAME	
600	2.02	1.40	1.64	BENZENE	
601	9.48	7.85	9.11	TOLUENE	
602	2.36	2.25	2.61	ETHYLBENZENE	
604	4.41	4.22	4.88	M-XYLENE	
605	1.78	1.71	1.97	P-XYLENE	
603	2.57	2.42	2.84	O-XYLENE	*
607	0.10	0.11	0.13	CUMENE	
644	0.53	0.57	0.66	N-PROPYL BENZENE	
609	1.55	1.68	1.95	1-ME-3-ET BENZENE	
610	0.69	0.75	0.86	1-ME-4-ET BENZENE	
613	0.79	0.85	0.99	135-TRIME BENZENE	
608	0.48	0.51	0.60	1-ME-2-ET BENZENE	*
612	2.37	2.54	2.97	124-TRIME BENZENE	*

1CHEVRON RESEARCH GASOLINE ANALYSIS Page 8
5-Apr-1996 19:55
6018638 API BASE GASOLINE 13GAS0126
Sample 3 Injection 1

Appendix C - Additional Model Development Details

Chapter 2: Model bench-marking efforts, Conservative Transport

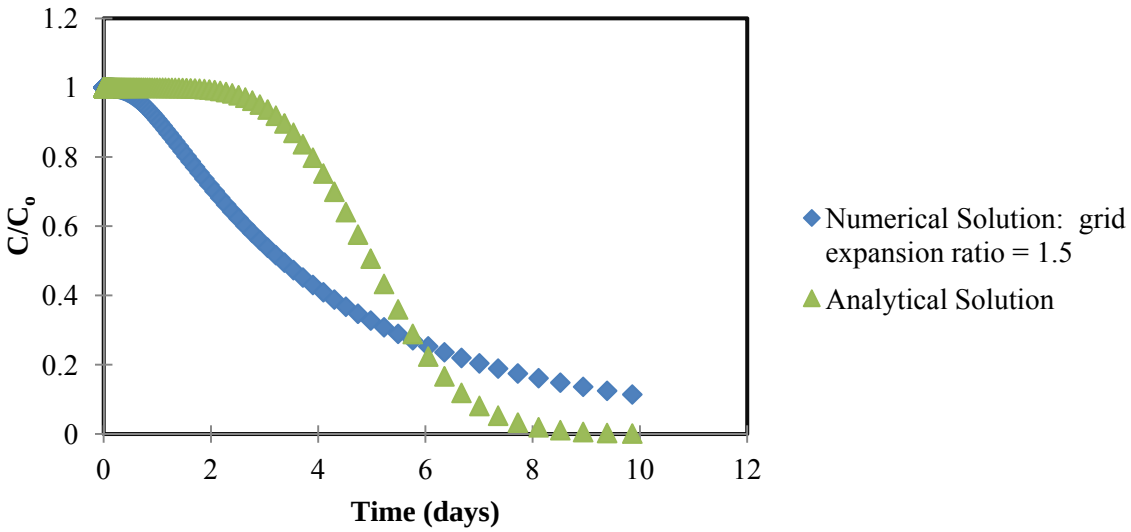

Figure C-1. Change in numerical solution due to increase in grid expansion ratio

Numerical Scheme and exponential weighting details

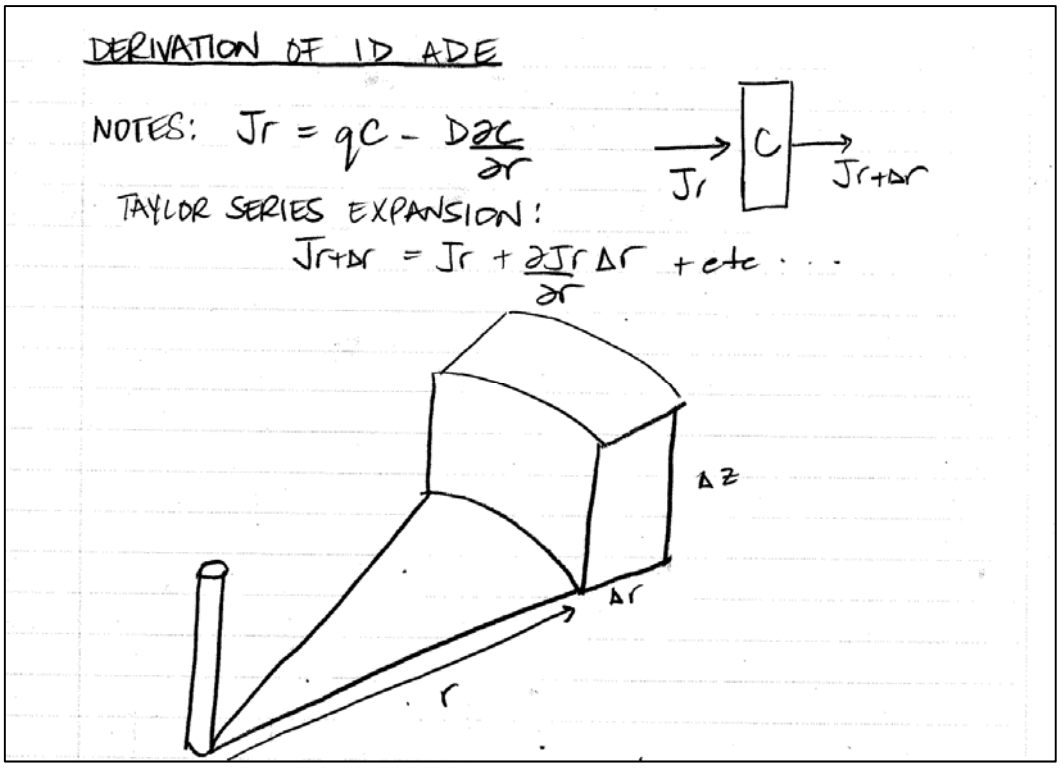

STORAGE IN OUT

① $\frac{\partial}{\partial t}\left[c\phi\Delta z\left(\pi(r+\Delta r)^2-\pi r^2\right)\right] = J_r 2\pi r\Delta z - J_{r+\Delta r}\left[2\pi(r+\Delta r)\Delta z\right]$

② $\frac{\partial}{\partial t}\left[c\phi\Delta z\pi(r^2+2r\Delta r+\Delta r^2-r^2)\right]$ ($\Delta r^2 \approx 0$)

$= J_r(2\pi r)\Delta z - J_{r+\Delta r}2\pi r\Delta z - J_{r+\Delta r}2\pi\Delta r\Delta z$

($J_{r+\Delta r}$: SUB IN TAYLOR)

③ $\frac{\partial}{\partial t}\left[c\phi\Delta z\pi 2\pi r\Delta r\right]$

$= J_r(2\pi r\Delta z) - \left[J_r + \frac{\partial J_r}{\partial r}\Delta r\right](2\pi r\Delta z) - \left[J_r + \frac{\partial J_r}{\partial r}\Delta r\right](2\pi\Delta r\Delta z)$

$= J_r 2\pi r\Delta z - J_r 2\pi r\Delta z - \frac{\partial J_r}{\partial r}\Delta r 2\pi r\Delta z - J_r 2\pi\Delta r\Delta z - \frac{\partial J_r}{\partial r}\Delta r^2 2\pi\Delta z$ ($\Delta r^2 \to 0$)

$= -\frac{\partial J_r}{\partial r}\Delta r 2\pi r\Delta z - J_r 2\pi\Delta r\Delta z$

$\frac{\partial}{\partial t}\left[c\phi\Delta z\pi 2r\Delta r\right] = -J_r 2\pi\Delta r\Delta z - \frac{\partial J_r}{\partial r}\Delta r 2\pi r\Delta z$

$r\frac{\partial}{\partial t}[c\phi] = -J_r - r\frac{\partial J_r}{\partial r}$

$\frac{\partial}{\partial t}[c\phi] = \frac{1}{r}\left[-J_r - r\frac{\partial J_r}{\partial r}\right]$ → CHAIN RULE

$\frac{\partial[c\phi]}{\partial t} = -\frac{1}{r}\frac{\partial}{\partial r}(rJ_r)$

NUMERICAL SCHEME

- EXPONENTIAL WEIGHTING
- FINITE VOLUME
- INJECTION PHASE

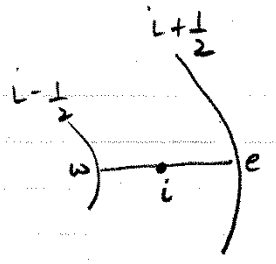

$$\frac{\partial(C\Phi)}{\partial t} = -\frac{1}{r}\frac{\partial}{\partial r}\left(rqC\right) + \frac{1}{r}\left(r\Phi D\frac{\partial c}{\partial r}\right)$$

$$\frac{\Phi V}{\Delta t}\left(C - C^{\circ}\right) = \left(-\frac{q}{\Phi}AC\right)_e - \left(-\frac{q}{\Phi}AC\right)_w + \left(\Phi D\frac{\partial c}{\partial r}A\right)_e - \left(\Phi D\frac{\partial c}{\partial r}A\right)_w$$

(C°: OLD TIMESTEP)

SUB: $T = \frac{V}{\Delta t}$, $P = \frac{F}{H}$, $F = V$, $H = \frac{\alpha_r V + Dm}{\Delta r}$, $A = 2\pi r$, $q = \frac{Q}{2\pi b r}$, $V = \frac{q}{\Phi}$

EXPONENTIAL WEIGHTING SCHEME

$$-TC + TC^{\circ} = -FeAeCe + FwAwCw$$

$$T(C - C^{\circ}) = -FeAe\left[C + \frac{C - C_{i+1}}{\exp(Pe) - 1}\right] + FwAw\left[C_{i-1} + \frac{C_{i-1} - C_i}{\exp(Pw) - 1}\right]$$

$$-TC_i + TC^{\circ} = -\left[\frac{FeAe}{\exp(Pe) - 1}\right]C_{i+1} \quad (tii)$$

$$+\left[FeAe + \frac{FeAe}{\exp(Pe) - 1} + \frac{FwAw}{\exp(Pw) - 1}\right]C_i \quad (ti)$$

$$-\left[\frac{FwAw\exp(Pw)}{\exp(Pw) - 1}\right]C_{i-1} \quad (iti)$$

$$-TC_i + TC^{\circ} = ti\,\theta C_i - iti\,\theta C_{i-1} - tii\,\theta C_{i+1} + ti(1-\theta)C^{\circ} - iti(1-\theta)C^{\circ}_{-1} - tii(1-\theta)C^{\circ}_{+1}$$

$$\left[T - ti(1-\theta)\right]C^{\circ} + tii(1-\theta)C^{\circ}_{+1} + iti(1-\theta)C^{\circ}_{-1} = -iti\,\theta C_{i-1} + (T + ti\,\theta)C_i - tii\,\theta C_{i+1}$$

$\theta = 0.5$ for Crank-Nicolson time-marching scheme

Appendix D - Chapter 3 Supplemental Figures

Permanganate Sensitivity Analysis (Section 3.1.2)

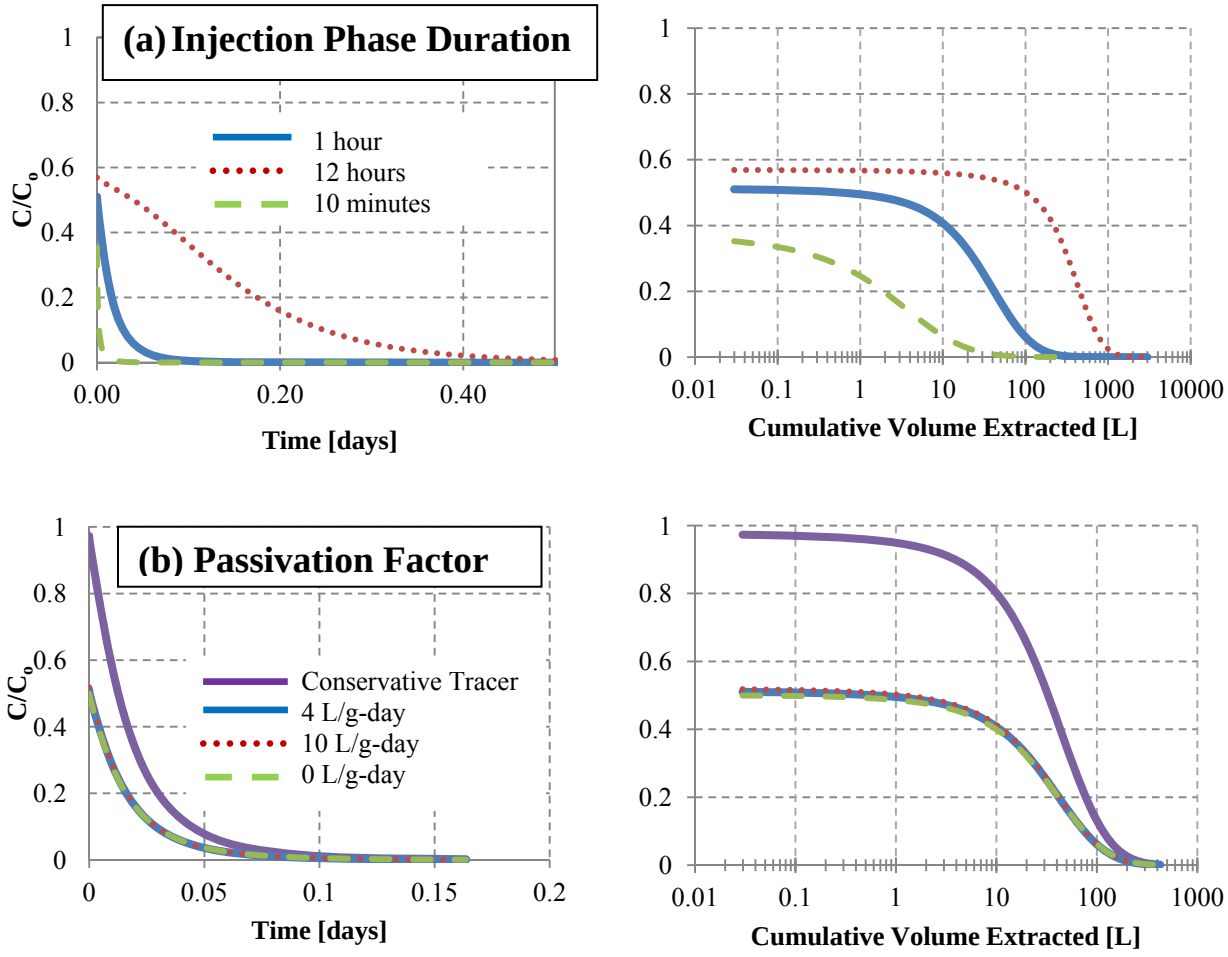

Figure D-1. Permanganate PPT BTCs in response to variations in field operational or NOI parameters

Persulfate Sensitivity Analysis (Section 3.1.2)

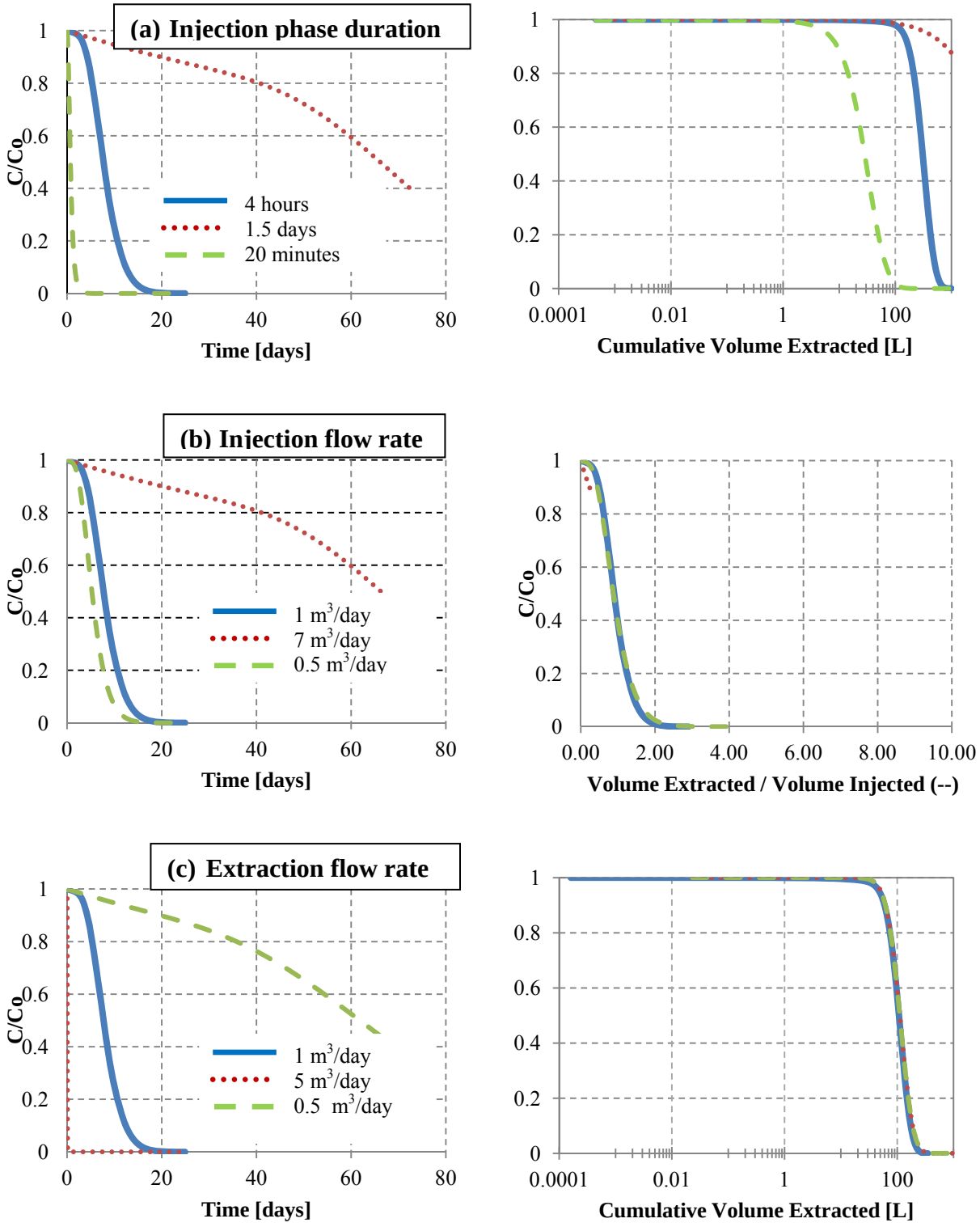

Figure D-2. Persulfate PPT BTCs in response to variations in field operational or NOI parameters

Appendix E - Chapter 4 Supplemental Figures and Tables

Treatability PPTs: Sensitivity Analysis (Section 4.2)

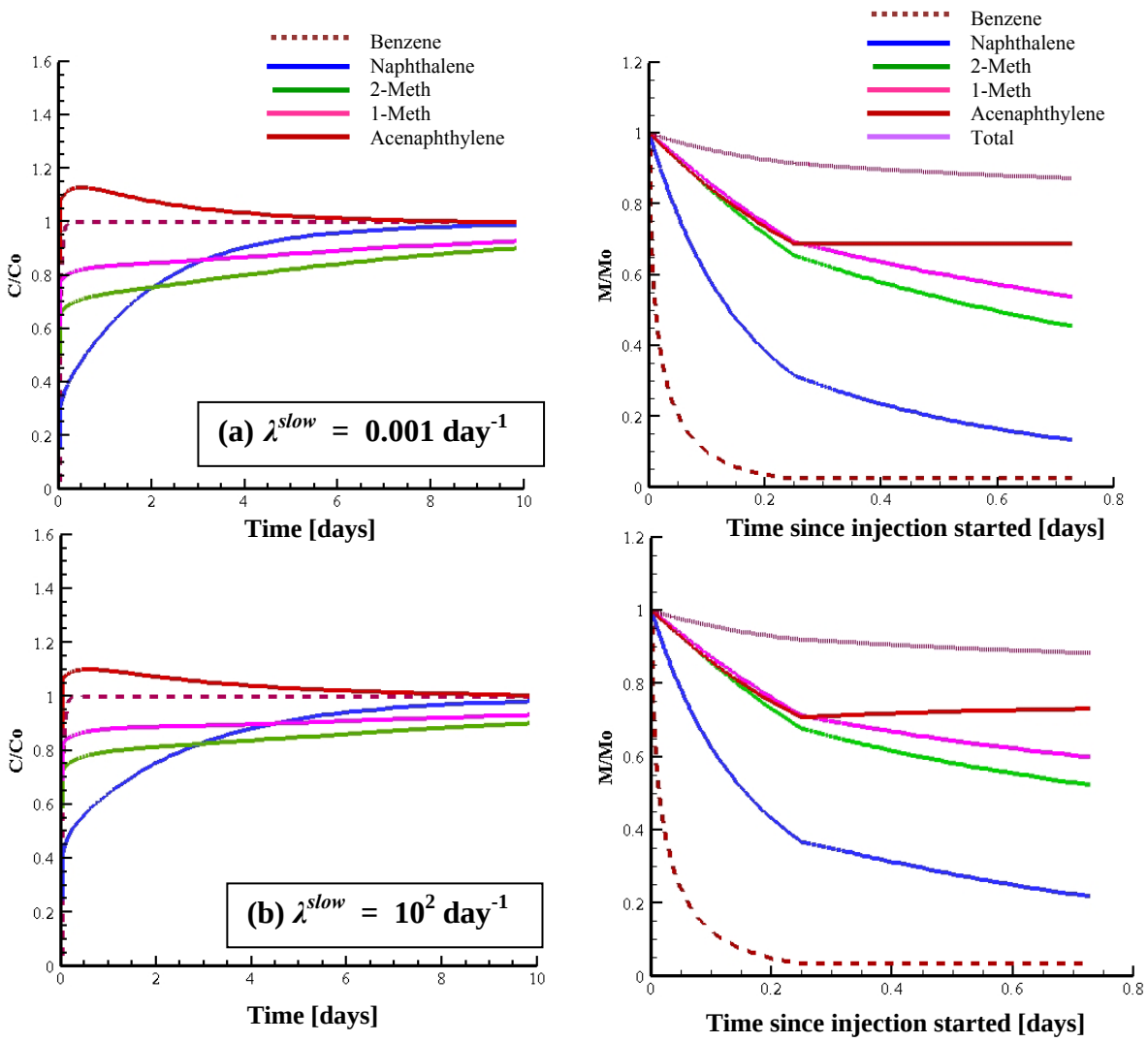

Figure E-1. NAPL PPT results for variations in λ^{slow}: left-hand plots represents PPT BTCs, right-hand plots represents the fast region NAPL mass profile located 0.04 m from the well

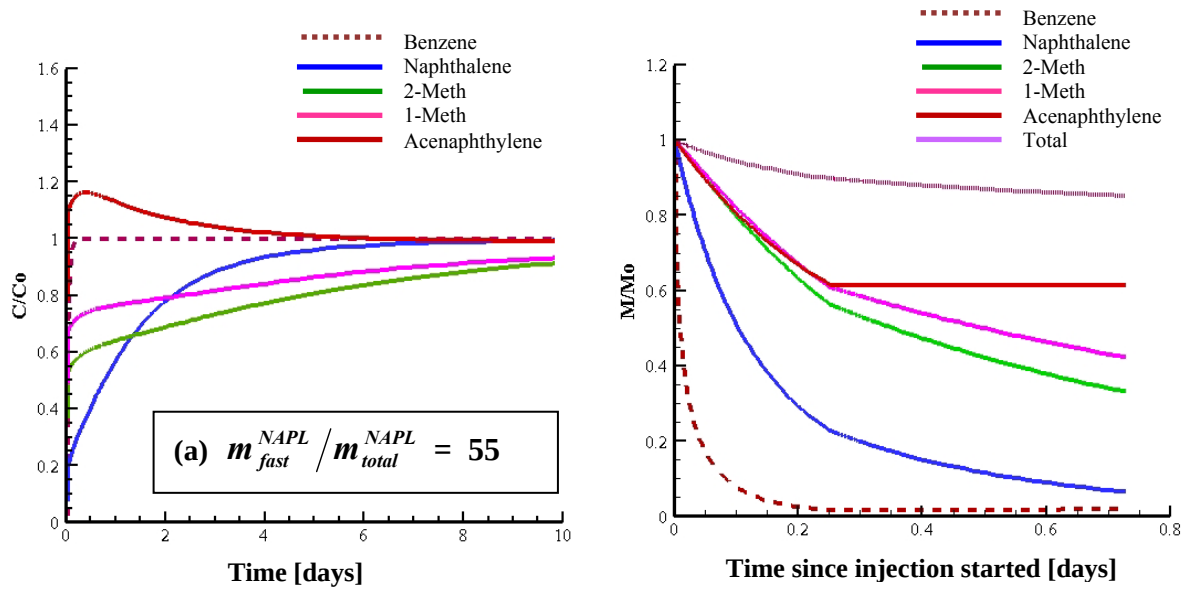

Figure E-2. NAPL PPT results for $m_{fast}^{NAPL} / m_{total}^{NAPL}$ = 55%: left-hand plot represents PPT BTCs, right-hand plot represents the fast region NAPL mass profile located 0.04 m from the well

Oxidant Dosage and Treatability (Section 4.3)

Table E-1. MGP Treatability Assessment

MGP Component	Mass oxidized (mg)
Toluene	572
Ethylbenzene	1620
Naphthalene	62438
2-Meth	14832
1-Meth	6923
Acenaphtene	18586
Fluorene	17034
Phenanthrene	18525
Anthracene	2882
Fluoranthene	2717
Pyrene	3191
Chrysene	<100
BaP	<100
Total (mg)	149320
Total (mg-NAPL/g-permanganate consumed)	**52.4**

Oxidant Dosage and Treatability (Section 4.3)

Table E-2. NOI neglected: MGP Treatability Assessment

MGP Component	Mass oxidized (mg)
Toluene	507
Ethylbenzene	1694
Naphthalene	66701
2-Meth	16512
1-Meth	7380
Acenaphtene	24548
Fluorene	25827
Phenanthrene	38264
Anthracene	4453
Fluoranthene	9472
Pyrene	13953
Chrysene	<10
BaP	<10
Total	209310
Total (mg-NAPL/g-permanganate consumed)	86
g permanganate consumed/g NAPL oxidized	12

Oxidant Behaviour (Section 4.4)

Table E-3. Permanganate PPT: Gasoline Treatability Assessment

Gasoline Component	Composition A mass oxidized (mg)	Composition B mass oxidized (mg)
Toluene	35283	28291
Ethylbenzene	25097	33789
Naphthalene	192	14055
o-xylene	6621	7474
m,p-xylene	17522	15511
123-TMB	661	1259
124-TMB	2086	1523
135-TMB	568	612
total NAPL mg	88030.4	102514
g-gasoline oxidized/g oxidant consumed	35	36

Persulfate PPT Results: Oxidant Behaviour (Section 4.4)

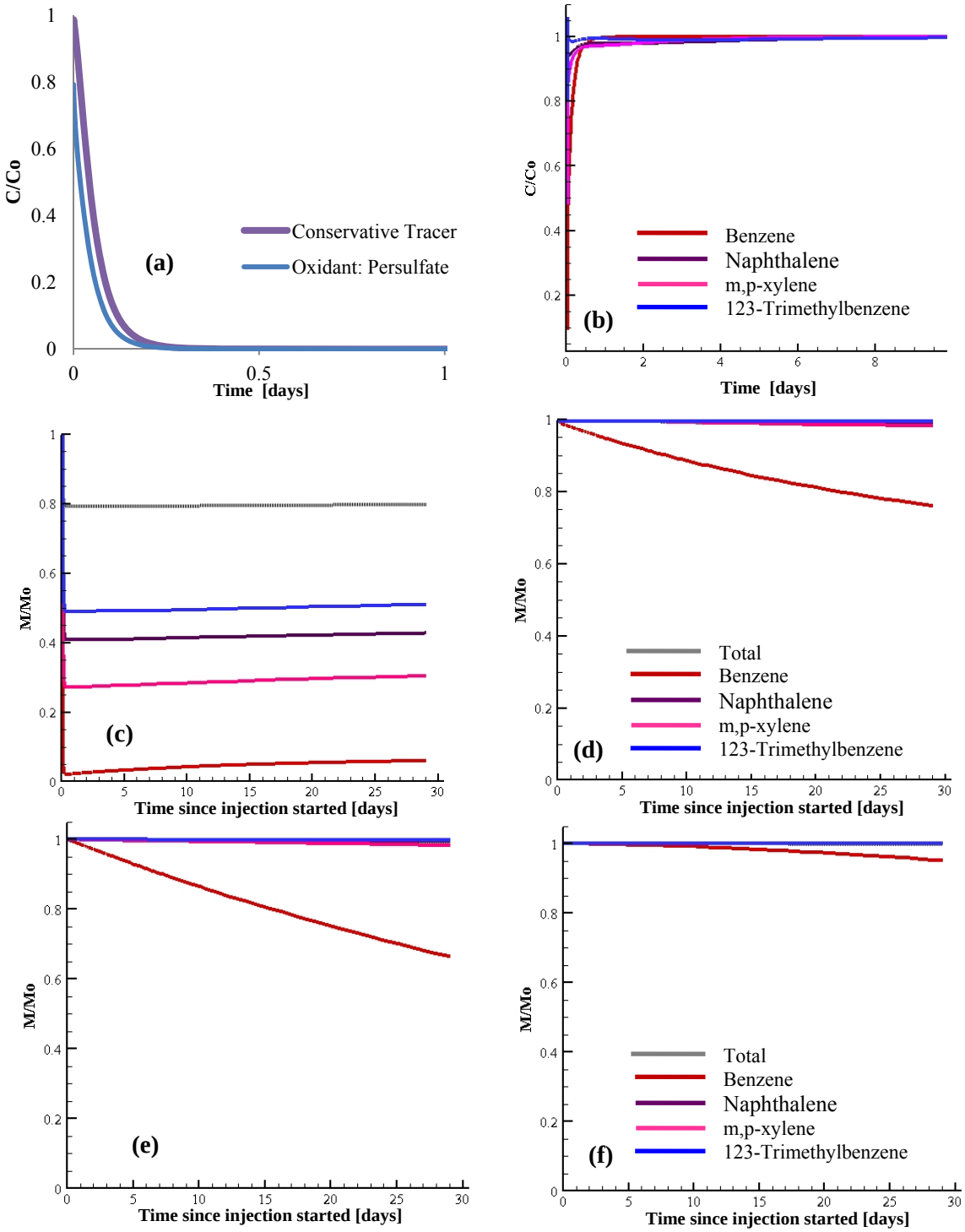

Figure E-3. Results for persulfate PPT into gasoline contaminated aquifer (gasoline composition A): (a) persulfate and tracer BTCs, (b) gasoline component BTCs, fast region NAPL mass profiles at (c) 0.04m and (e) 0.4 m from the well, and slow region NAPL mass profiles at (d) 0.04 m and (f) 0.4 m from the well